Workshop of
Experimental Nuclear and Particle Physics
2016

16.–23. 01. 2016, Bílý Potok

Faculty of Nuclear Sciences and Physical Engineering
Czech Technical University in Prague

Workshop of Experimental Nuclear and Particle Physics 2016
Editors: Z. Gajdošová, D. Horák, V. Pacík, R. Novotný
Issued by: Czech Technical University in Prague
Faculty of Nuclear Sciences and Physical Engineering
Address: KF FJFI ČVUT, Břehová 7, 115 19 Praha 1
novotr14@fjfi.cvut.cz, +420731891801
Available at `http://wejcf2016.ejcf.cz/wejcf2016_proceedings.pdf`
First edition. 157 pages.
ISBN 978-80-01-06005-6

Contents

Foreword

This year, for the 10th time, students, graduates, and teachers from the field of Experimental Nuclear and Particle Physics at FNSPE CTU met at the annual winter workshop. The meeting was held during the week of 16.–23. 01. 2016 at *Penzion Krakonoš* in the Jizera Mountains in the Czech Republic. The main goal of the workshop is to follow the progress of students, discuss problems and experiences and also to get to know each other better. Each participant gave a talk about their work or progress during the previous year. Extended abstracts of these talks are published in the proceedings you are holding now.

Editors

Energy evolution of exclusive J/ψ photoproduction off protons

Jaroslav Adam*(jaroslav.adam@cern.ch)*

Abstract

Heavy ions, accelerated to ultra-relativistic energies, create strong electromagnetic fields which allow one to study photon-photon, photon-proton and photon-nucleus reactions in ultra-peripheral collisions. The reactions offer the possibility to study saturation phenomena and nuclear gluon shadowing.

1 Introduction

The ultra-peripheral collision (UPC) is a collision mediated only by electromagnetic interaction without the contribution of strong forces. Such reaction is achieved when the collision occurs at impact parameter greater than the sum of nuclear radii; the strong interaction is then suppressed by it's short range nature. The electromagnetic field mediating the UPC collision is described as a flux of virtual photons. Review of the UPC physics is given in [1], review of the LHC results is presented in [2].

2 Photoproduction of J/ψ in photon-proton interactions

By means of perturbative Quantum Chromo-Dynamics (pQCD), the photoproduction reaction is modeled at a leading order (LO) as fluctuation of the virtual photon into a pair of $c\bar{c}$ quarks which then interacts on the proton via the two-gluon exchange. As a result of the interaction, free J/ψ particle as a bound state of $c\bar{c}$ is produced. Such photoproduction is exclusive since no other particles are produced.

Cross section of exclusive J/ψ photoproduction off proton, $\sigma(\gamma+\mathrm{p} \rightarrow J/\psi+\mathrm{p})$ is proportional, according to LO pQCD, to the square of the proton gluon distribution. Data on the cross section at different values of the photon-proton center-of-mass energy $W_{\gamma\mathrm{p}}$ allows to probe the gluon distribution at different momentum fractions given by the Bjorken variable $x = (M_{J/\psi}/W_{\gamma\mathrm{p}})^2$ where $M_{J/\psi}$ is the mass of the J/ψ.

ALICE experiment has measured exclusive photoproduction off protons in ultra-peripheral p-Pb collisions [3]. The asymmetrical system provides constraints to the kinematics of the reaction, because the lead ion is most likely (at ∼95%) the source of the virtual photons. The photon-proton center-of-mass energy $W_{\gamma\mathrm{p}}$ is given by the energy of the proton beam E_p and rapidity y of the J/ψ as $W_{\gamma\mathrm{p}}^2 = 2E_pM_{J/\psi}\exp(-y)$.

The rapidity y is measured in the laboratory system according to the direction of the proton beam. Outside mid-rapidity, y takes positive sign for the J/ψ produced in the direction of the proton beam and negative sign otherwise. At fixed beam energy, the photon-proton energy $W_{\gamma\mathrm{p}}$ is larger at negative rapidities. ALICE data cover wide range of energies, namely 20 GeV $\lesssim W_{\gamma\mathrm{p}} \lesssim$ 1 TeV.

Previous measurements of exclusive J/ψ photoproduction in the photon-proton interactions are reported from HERA experiments H1 [4] and ZEUS [5]. Energy range covered by these two experiments is $20 < W_{\gamma\mathrm{p}} < 305$ TeV. The LHCb experiment has extracted the photon-proton cross section using the proton-proton symmetrical collisions [6].

Empirical power-law parametrization to the cross section as a function of the energy was found by the HERA experiments. The data on the photon-proton cross section was parametrized as $\sigma(\gamma\text{+p} \to J/\psi\text{+p}) = N(W_{\gamma\mathrm{p}}/W_0)^{\delta}$. Corresponding empirical parametrization to the proton gluon distribution was set as $x \cdot g(x, \mu^2) = N \cdot x^{-\lambda}$ with $\delta \approx 4 \cdot \lambda$.

The parametrization of the gluon distribution indicate increasing number of gluons carrying lower fractions x of the proton total momentum. To meet the unitarity constraints the increase is supposed to stop starting at some value of x and hence at some $W_{\gamma\mathrm{p}}$. The gluon density will saturate in such a scenario.

Finding the onset of the gluon saturation, e.g. the energy at which the behavior of the cross section will change from the power-law prescribed by the HERA results is the main experimental task.

3 The ALICE experiment at the LHC

The ALICE measurement of the exclusive J/ψ photoproduction off protons reported here used the forward muon spectrometer covering the pseudorapidity interval $-4.0 < \eta < -2.5$. The spectrometer consists of a composite absorber, five MWPC tracking stations, a trigger system of RPC and dipole magnet of integrated field of 3 T·m.

The forward scintillator arrays, VZERO-A and VZERO-C were used for triggering and for exclusivity selection. Pseudorapidity coverage is $2.8 < \eta < 5.1$ for VZERO-A and $-3.7 < \eta < -1.7$ for VZERO-C. The Zero Degree Calorimeters (ZDC) detect very forward neutrons at pseudorapidity $|\eta| > 8.8$.

Additional measurement was also performed using the central tracking detectors with overall acceptance $|\eta| < 0.9$. The central detectors, listed in increasing radial distance from the nominal interaction point are the Inner Tracking System (ITS), the Time Projection Chamber (TPC) and the time-of-flight detector (TOF). Triggering in the central detectors is provided by the Silicon Pixel Detectors (SPD) which are the two innermost layers of the ITS (out of six) and by TOF.

4 ALICE measurement of exclusive J/ψ photoproduction off protons

The J/ψs have been reconstructed via it's dimuon decays $J/\psi \to \mu^+\mu^-$. The event selection was based on finding just two tracks in an otherwise empty detector.

The two unlike-sign tracks were required in the forward muon spectrometer. The activity in VZERO-C, which is located at the same side as the forward muon spectrometer, was required to be compatible with the two muons within the expected time interval for beam-beam interaction. No activity was required in VZERO-A on the opposite side. Remaining forward activity was rejected by the ZDCs, central activity was removed by requirements for the SPD.

As the rapidity of the J/ψ covered by the foward muon spectrometer is $2.5 < |y| < 4.0$, according to the relation $W^2_{\gamma\mathrm{p}} = 2E_p M_{J/\psi} \exp(-y)$ the energy is $W_{\gamma\mathrm{p}} \in [21, 45]$ GeV for the case when the proton beam is oriented towards the muon spectrometer (denoted as p-Pb) and [577, 952] GeV for the proton beam moving in the opposite direction (Pb-p).

4.1 Signal extraction

Distribution of invariant mass of selected dimuon candidates is shown in Figure 1 on the left for p-Pb (up) and for Pb-p (down). Mass peak of the J/ψ is clearly visible above the expected background form two-photon production of dimuon pairs $\gamma\gamma \to \mu^+\mu^-$.

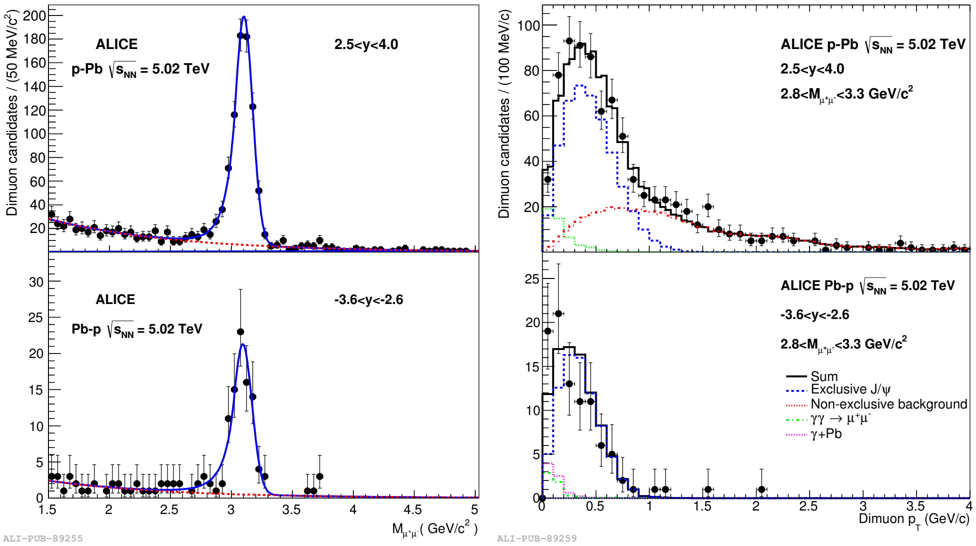

Figure 1: Invariant mass and transverse momentum distributions for forward (up) and backward (down) dimuon samples [3].

The number of the J/ψ coming from photon-proton interactions $\gamma\mathrm{p} \to J/\psi\mathrm{p}$ was extracted using the fit to the transversal momentum p_T distribution of the J/ψ candidates.

The procedure is shown in the right part of Figure 1. The p_T distribution of events within the peak of the J/ψ is fitted using the MC templates for signal $\gamma\mathrm{p} \to J/\psi\mathrm{p}$ and for $\gamma\gamma \to \mu^+\mu^-$ and the template for non-exclusive production both of the J/ψ and the dimuons.

In the case of Pb-p (Figure 1 right down), the contribution of coherent J/ψ photoproduction on the Pb nucleus is also added to the fit, denoted as γ+Pb in the legend.

4.2 Experimental cross section of exclusive J/ψ photoproduction in p-Pb

The differential cross section is given by the yield of exclusive candidates $N^{\text{exc}}_{J/\psi}$ corrected for the total acceptance and efficiency $\varepsilon_{J/\psi}$ as

$$\frac{\mathrm{d}\sigma}{\mathrm{d}y} = \frac{N^{\text{exc}}_{J/\psi}}{\varepsilon_{J/\psi} \cdot \mathcal{B} \cdot \mathcal{L}} \cdot \frac{1}{\Delta y}, \tag{1}$$

where $\mathcal{B}$ is the branching ratio of the J/ψ dimuon decay $J/\psi \to \mu^+\mu^-$ and $\mathcal{L}$ is the luminosity of the data sample. The Δy is the with of rapidity interval where the differential cross section is measured.

The yield of exclusive candidates $N^{\text{exc}}_{J/\psi}$ is obtained from the number of candidates extracted from the p_T fits $N_{J/\psi}$ by applying the correction for the feed-down f_D from ψ'. The corrected yield is $N^{\text{exc}}_{J/\psi} = N_{J/\psi}/(1 + f_D)$.

The efficiency $\varepsilon_{J/\psi}$ is calculated using the MC of $\gamma\mathrm{p} \to J/\psi\mathrm{p}$. The events were generated using the STARLIGHT event generator [7] and folded by the full detector simulation. The output of the simulation was analysed using the same selection criteria as for the data, providing the number of reconstructed events in the simulation. The number of generated events was obtained by reading the generator input. The efficiency is the ratio of reconstructed events to the generated, both in the rapidity interval used for the reconstruction.

In Pb-p, the trigger required minimal energy deposition in VZERO-C. The data-driven estimate of the efficiency was used for this part of the trigger selection.

The photon-proton cross section $\sigma(\gamma\mathrm{p} \to J/\psi\mathrm{p})$ is obtained from the differential cross section using the flux of virtual photons $\mathrm{d}N_\gamma/\mathrm{d}k$, which is the distribution of photons carrying a momentum k. The relation is

$$\frac{\mathrm{d}\sigma}{\mathrm{d}y}(\mathrm{p{+}Pb} \to \mathrm{p{+}Pb} + J/\psi) = k\frac{\mathrm{d}N_\gamma}{\mathrm{d}k}\sigma(\gamma\mathrm{p} \to J/\psi\mathrm{p}). \tag{2}$$

The photon flux has been calculated using STARLIGHT. The direct proportionality between the cross sections presented in equation 2 is possible thanks to the constraints on the photon source (most likely the lead ion).

5 Energy evolution of the photoproduction cross section

The photon-proton cross section is shown in the left part of Figure 2 together with HERA data [4, 5] and theoretical models. The model by JMRT group [8] is based on pQCD treatment of the interaction while the b-Sat model [9, 10] uses the color dipole approach. The STARLIGHT parametrization is fixed according to the HERA and fixed-target data.

A power law fit by $\sigma(\gamma{+}\mathrm{p} \to J/\psi{+}\mathrm{p}) = N(W_{\gamma\mathrm{p}}/W_0)^\delta$ has been made to the cross section as a function of energy $W_{\gamma\mathrm{p}}$. Value of the slope parameter δ corresponding to ALICE results is 0.68 ± 0.06, while similar fits to HERA data provided 0.69 ± 0.04 and 0.67 ± 0.03 for ZEUS and H1 respectively. The result of the fit is compatible with the previous HERA results, indicating that no change in gluon behavior has been observed coming to the LHC energies.

Right part of Figure 2 shows comparison of the fit to the ALICE data with LHCb solutions to the photon-proton cross section [6]. The LHCb experiment has

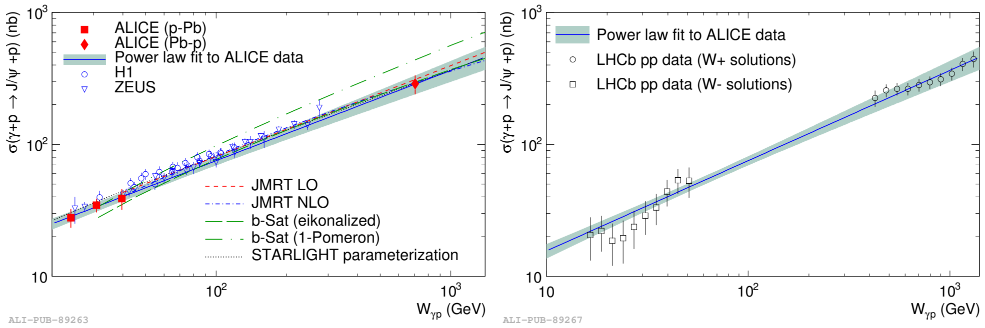

Figure 2: Exclusive J/ψ photoproduction cross section off protons [3].

measured the differential cross section of exclusive J/ψ photoproduction in symmetrical proton-proton collisions. Ambiguity on the photon source occurs, because each proton can serve as a photon source and a target, leaving the kinematics of the photon-proton interaction unconstrained. For each rapidity interval where the differential cross section has been measured, two solutions to the $\sigma(\gamma\text{p} \to J/\psi\text{p})$ have been extracted assuming higher and lower energy of the photon. The solutions are consistent with the fit to the ALICE data.

6 Conclusions

The ALICE experiment has made the first LHC measurement of exclusive J/ψ photoproduction off protons, increasing the energy range of photon-proton center-of-mass energy almost three times compared to the previous measurements at HERA. At the lower energies, the ALICE results are compatible with results by HERA experiments. Partonic models based on pQCD and models using the color dipole approach are consistent with the experimental results. At the current energy covered by ALICE and at the current experimental precision no change in gluon behavior has been observed going from HERA to LHC energies.

An update to ALICE measurements on the photon-proton cross section presented in [3] is now well advanced, values of the cross section are being calculated within the energy range of the current measurement, giving more complete picture of the energy evolution.

References

[1] A. J. Baltz et al., Phys. Rept. 458, 1 (2008)

[2] J. G. Contreras and J. D. Tapia Takaki, Int. J. Mod. Phys. A 30, 1542012 (2015)

[3] B. Abelev *et al.* [ALICE Collaboration], Phys. Rev. Lett. 113, 232504 (2014)

[4] A. Aktas et al. [H1 Collaboration], Eur. Phys. J. C 46, 585 (2006)

[5] S. Chekanov et al. [ZEUS Collaboration], Eur. Phys. J. C 24, 345 (2002)

[6] R Aaij et al, [LHCb Collaboration], J.Phys. G 41 055002 (2014)

[7] S. Klein and J. Nystrand, Phys. Rev. C 60, 014903 (1999), http://starlight.hepforge.org/

[8] S. P. Jones, A. D. Martin, M. G. Ryskin and T. Teubner, JHEP 1311, 085 (2013)

[9] H. Kowalski, L. Motyka and G. Watt, Phys. Rev. D 74, 074016 (2006)

[10] J. L. Abelleira Fernandez *et al.*, arXiv:1211.4831 [hep-ex]

Properties of cosmic ray showers of ultra-high energies

Alena Bakalová *(bakalale@fjfi.cvut.cz)*

Introduction

Cosmic ray showers are initiated by primary particles coming from outer space which afterwards penetrate into the atmosphere and create secondary particles. In order to describe the showers, we can use simulations, such as CONEX [1, 2], which combines the Monte Carlo method with detailed hadronic interaction models. Also the semi-empirical models has been proposed. Such models are based on simplified description of the main characteristics of the showers. Showers initiated by a primary photon can be interpreted by the Heitler model of extensive air showers [3], while hadronic showers can be described by the Heitler-Matthews model [3]. The problem of main parameters of cosmic ray showers has been investigated from many different points of view (see e.g. [3, 4, 5]).

The Heitler model of EM cascades describes a photon initiated shower and contains only three types of particles - photons, electrons and positrons. After traversing one splitting length d in the atmosphere, a photon splits into an electron-positron pair, each carrying half of the primary energy. After travelling the same distance d, both electron and positron each radiate a bremsstrahlung photon. Again, the energy of the particle is equally divided between an electron and a photon. The splitting process described above continues until particles reach a critical energy, which for electrons in the air is $\xi_c^e = 85\,\mathrm{MeV}$. Two important parameters can be derived from this model. The first one is the shower maximum X_{max}, which is a penetration depth where the shower reaches the maximum amount of particles. The second parameter is the elongation rate Λ, the rate of increase of X_{max} with primary energy defined by the formula

$$\Lambda = \frac{\mathrm{d}X_{max}}{\mathrm{d}\log_{10} E_0} \tag{1}$$

where E_0 is the energy of the primary particle.

Hadronic showers are modeled by the Heitler-Matthews model. These showers have both hadronic and electromagnetic component. A primary particle, e.g. proton, penetrates into the atmosphere and decays into N_{ch} charged pions and $\frac{1}{2}N_{ch}$ neutral pions. Neutral pions create secondary EM showers, described by the Heitler model, while charged pions travel one layer d of the atmosphere and interact. This layer is given as

$$d = \lambda_I \ln 2 \tag{2}$$

where λ_I is the interaction length. λ_I is considered as a constant value. When these charged pions reach the energy where the decay length of a charged pion is smaller than the distance to the point of the next interaction, they all decay into muons and muon neutrinos. The total number of muons is given by the relation

$$N_\mu = (\frac{E_0}{\xi_c^\pi})^\beta \tag{3}$$

where the parameter β is 0.85, according to the Heitler-Matthews model, when we take N_{ch} as a constant with value $N_{ch} = 10$. The value of the elongation rate for proton initiated showers is $\Lambda = 58\,\mathrm{g \cdot cm^{-2}}$, but the same number corresponds to other elements' nuclei, such as helium or iron.

Methods and Results

Our simulations of high-energy cosmic ray showers were created in the simulation code CONEX, which combines the Monte Carlo simulation and the numerical description of hadronic interactions. Using two different models EPOS-LHC [6, 7] and QGSJet II-04 [8], we created showers of primary energy from 10^{14} eV to 10^{20} eV for four primaries - proton, helium, nitrogen and iron. For EM showers, we used EPOS-LHC simulations for energies scaled from 10^{14} eV to 10^{19} eV. The data obtained were compared to aforementioned semi-empirical models. The main focus was so far given to the elongation rate Λ and the parameter β.

Regarding the elongation rate, we plotted a dependence of X_{max} on energy of the primary particle. By fitting this dependence of EPOS-LHC simulations, we obtained a value for proton initiated showers $\Lambda = 58.0 \pm 1.0\,\mathrm{g \cdot cm^{-2}}$, which corresponds satisfactorily with the predicted value by Heitler-Matthews. For other elements, the value has a rising tendency. Such a behavior is not predicted by the Heitler-Matthews model. The values are $60.9 \pm 0.8, 64.0 \pm 0.6$ and $65.7 \pm 0.4\,\mathrm{g \cdot cm^{-2}}$ for helium, nitrogen and iron respectively. For EM showers, the elongation rate is $\Lambda = 90 \pm 2\,\mathrm{g \cdot cm^{-2}}$, while the Heitler model predicts the rate $\Lambda = 85\,\mathrm{g \cdot cm^{-2}}$.

By plotting the dependence of number of muons in X_{max} on energy, we were able to obtain the value of parameter β. Our simulations show the value of the parameter as $\beta = 0.906 \pm 0.003$ for EPOS-LHC and $\beta = 0.900 \pm 0.002$ for QGSJet II-04. This value is a bit higher than the one predicted by the model, but it corresponds with other simulations, as mentioned in [3].

Conclusion

These results show that the value of the elongation rate is well described by these models for EM showers and proton initiated showers. For other nuclei, the atomic number needs to be taken into account. In the future, we would like to compare our simulation results with other models, such as the extended Heitler-Matthews model [5] , which predicts an increasing value of elongation rate with a higher atomic number. Regarding the parameter β, our value is higher than the predicted one. Such finding is mainly caused by consideration of N_{ch} as a constant value.

References

[1] T. Bergmann et al., Astropart. Phys. 26, 420-432 (2007)

[2] T. Pierog et al., Nucl. Phys. B. - Proc. Suppl. 151, 159 (2006)

[3] J. Matthews, Astropart. Phys. 22, 387 (2005)

[4] J. Vicha, P. Travnicek & D. Nosek, arXiv:1509.06320 (2015)

[5] Pierre Auger Collaboration, Journal of Cosmology and Astroparticle Physics 2, 026 (2013)

[6] K. Werner, F. M. Liu & T. Pierog, Phys. Rev. C 74, 044902 (2006)

[7] T. Pierog & K. Werner, Nucl. Phys. B - Proc. Suppl. 196, 102 (2009)

[8] S. S. Ostapchenko, Phys. Rev. D 83, 014018 (2011)

Diffractive processes at the LHC

Dagmar Bendová *(bendodag@fjfi.cvut.cz)*

---

1 Introduction

The total hadron-hadron cross-section of the interaction can be divided into two parts - first one corresponds to the elactic processes where both protons remain intact and are only rescatterend and the second one includes all of the inelastic processes, difractive and non-difractive in which one or both of the two protons are broken and new particles are produced during the interaction. In most cases, diffraction is considered to be the background of studied interaction. But it can be useful as the signal itself and lately it has become very important for studying the behaviour of QCD in the high-density regime, the low-x structure of the proton or even observe the Higgs boson. There will be given a brief theoretical description of the diffraction, it's experimental features and some of the results obtained from HERA, Tevatron and the LHC.

2 Theoretical view

Diffraction can be considered as a quasi-elastic process. Their experimental sign is detection of intact proton in the forward region and large rapidity gap in the central detector. We distinguish several types of diffraction processes according to the number of rapidity gaps and detected forward protons (see section 3 - Experimental signs of diffraction).

These experimental signs and therefore the diffractive process itself can be explained as exchange of the object with quantum numbers of vacuum, therefore we talk about a colorless exchange. This object is called Pomeron. According to the transverse momentum p_T we can distinguish between soft diffraction for low p_T, which can be descibed by Regge theory, and hard diffraction which is descibed by the means of perturbative QCD.

2.1 Regge theory and soft diffraction

Regge theory was developed in 1960s and is based on the analytical properties of scattering amplitudes as the function of angular momentum which is not discrete but can take any complex value. It describes interactions between hadrons (i.e. strong interaction) as the exchange of objects with quantum number of vacuum in t-channel. These objects are called "Regge trajectories" (or Reggeon) and so Pomeron can be seen as a specific Regge trajectory.

Although Regge theory was later succeeded by quantum chromodynamics, it is still very good approach for cases where one can not obtain predictions from pQCD, e.g. elastic scattering or diffraction.

2.2 Hard diffraction

For the hard diffraction, for which predictions of pQCD are used, one can also describe the interaction as the exchange of Pomeron. But it's important to realize that this Pomeron has different attributes than Pomeron described in Regge theory. In QCD object of quantum numbers of vacuum is considered to be the $q\bar{q}$ pair with opposite color charges. Color exchange is happening only between the quark and antiquark and so the result color charge of the object is zero.

2.2.1 Diffractive scattering in ep collisions at HERA

Although protons are not broken in diffractive process, there were several cases of production high p_T objects such as jets in $p\bar{p}$ interactions. These observations pointed out the possibility of describing diffraction in terms of partons and respective distribution functions. Great amount of work in this field was done at HERA where collisions of electron and proton were studied. But how can be possible that diffraction, a typical hadronic process, occured during the ep collision which is an electro-weak interaction? In this case, the electron radiates a very fast moving virtual photon with lifetime longer than a strong interaction time. This photon can fluctuate into a $q\bar{q}$ pair (color dipole, described above) and it's a pair which interacts with the proton by the strong interaction. After the interaction, proton carries large fraction of the incoming proton momentum and thus is detected in the forward region. As the result of the collision, hadronic state X with the virtual photon quantum numbers is created and large rapidity gap between X and forward proton is observed after the interaction. For illustration see Figure 1.

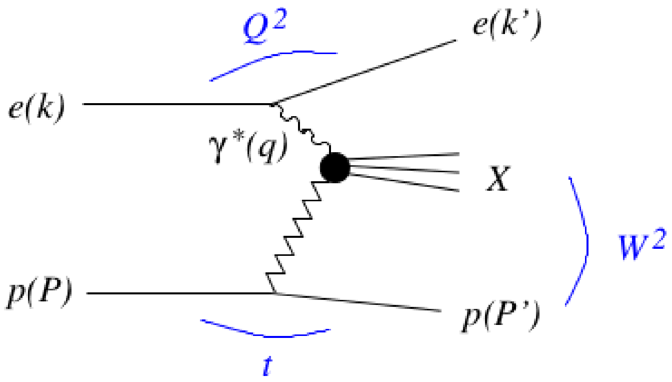

Figure 1: Diagram of inclusive diffractive process in ep collision at HERA [1].

Therefore $\gamma^* p \to Xp$ interaction can be described by the invariants $Q^2 = -q^2$, $t = (P - P')^2$, by fractional momentum loss of the incident proton

$$\xi = \frac{(P - P') \cdot q}{P \cdot q}, \tag{1}$$

and by the variable

$$\beta = \frac{Q^2}{2q(P - P')}, \tag{2}$$

which corresponds to the Bjorken variable x_B as $\xi \cdot \beta = x_B$. Therefore a diffractive distribution functions can be derived and for fixed β, ξ and t and in the limit of large Q^2 one can write a diffraction distribution function as

$$F_2^{D(4)}(\beta, \xi, t, Q^2) = \sum_i \int_\beta^1 \frac{\mathrm{d}z}{z} C_i \left(\frac{\beta}{z}\right) f_i^D(z, \xi, t, Q^2), \tag{3}$$

where the sum is over all partons of the type i, f_i^D is the corresponding parton distribution function and functions C_i describe scattering of the virtual photon on the parton.
Precise determinations of PDFs and their uncertainities were computed at HERA in order to give a prediction for cross-sections of diffractive processes at the LHC. But now comes the question whether it is appropriate to use PDFs obtained from ep collisions at HERA to describe hard diffractive processes in $p\bar{p}$ collisions at the Tevatron or in pp collisions at the LHC. The answer to this problem can be illustated on the results from diffractive dijet production, made by CDF collaboration, compared to the diffractive PDFs from HERA. As we can see on Figure 2, the fraction of diffractive dijet events is much smaller then our expactations based on HERA predictions. This type of disagreement was being observed in all $p\bar{p}$ interactions at the Tevatron. The difference between the prediction and real data is due to the interactions between the partons of the colliding hadrons which are mostly soft and therefore phenomenological models must be used to determine their effects. These soft interactions (also called reinteractions) lower the yield of diffractive event because they can produce another final state particles which can fill the rapidity gap and so we define the "gap survival probability" term (see sec. 3.1).

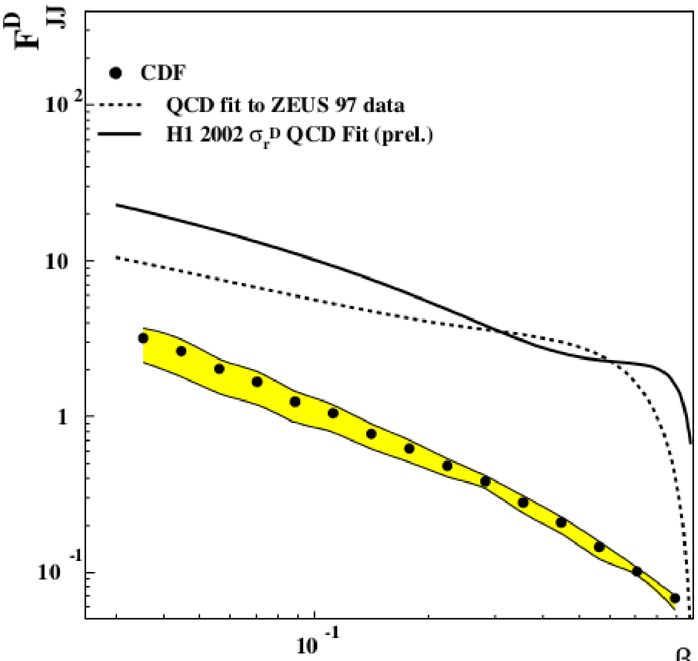

Figure 2: Cross section of diffractive dijet production in $p\bar{p}$ collision at the Tevatron compared with predictions from HERA. See also original CDF publication [5].

3 Experimental signs of diffraction

As mentioned above we can distinguish several types of diffractive processes. For illustration see Figure 3.
The most frequent and easiest to detect one is the single diffraction process in which one of the interacting protons dissociates into a final state hadronic system, which carries quantum number of the original proton, and the second proton remains intact. Large rapidity gap is produced separating the forward proton and the dissociated system. When both protons are broken and produce two dissociated systems separated bz rapidity gap, we talk about the double diffraction event. Double pomeron exchange (or central diffraction) occurs when both protons remain intact after interaction and a hadronic system with quantum number of vacuum is created in central region. Each proton is separated from the system by a rapidity gap. Also a multiple pomeron exchange can occur but this process is not so frequent and is also difficult to detect.

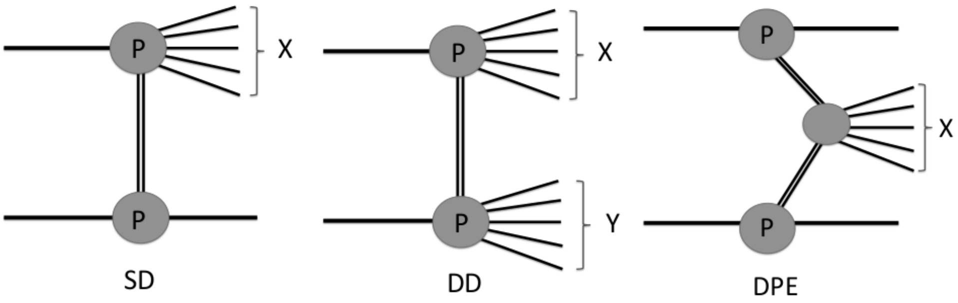

Figure 3: Single (left), double (center) diffraction and double pomeron exchange (left) [4].

3.1 Large Rapidity Gap

Rapidity gaps are regions in the central detector devoid of any hadronic activity. They are created as a result of colorless exchange during the diffractive event and they separate intact proton and system created from the other proton (see Figure 4). A non-pileup envoronment is optimal for observations of diffratcive processes because multiple soft hadron-hadron interactions could fill the gap. Also gaps can be observed in non-diffractive events due to the fluctuations in hadronization processes.
We can discribe rapidity gap $\Delta\eta_F$ using the invariant mass M_X of the dissociated system and momentum fraction of the proton lost in scattering ξ (see (1)). But for establishing the variable from data we rather use so called experimental observability

$$\bar{\xi} = \frac{\sum p_T e^{\pm\eta}}{\sqrt{s}} \tag{4}$$

where sum is over all clusters.
The size of the gap $\Delta\eta$ is then proportional to the experimental observability $\bar{\xi_X}$ (or to the mass M_X) and one can perform measurements of the cross-section as function of a gap size and momentum fraction. We evaluate mostly single diffraction events because their gap is easiest to detect and there is largest possibility of creation of dijets or other interesting objects on the forward edge of the gap. For example maximum rapidity at

the LHC $y_{max} = 11.5$, after some detector correstion we obtain a gap size $\Delta\eta \leq 9.6$ and because of the possibility of jets filling the gap, we determine maximum size of the rapidity gap $\Delta\eta \leq 7.2$ for the single diffraction process at the ATLAS experiment.
Because of the reinteractions which can fill the gap (as described in section 2.2.1) a gap survival probability $\langle S^2 \rangle$ variable which is defined as the fraction of events in which additional interactions do not spoil the gap and is currently the largest uncertainity for the description of diffractive processes at the LHC.
Gap survival probability was introduced during the diffractive experiments at the Tevatron and was discovered that $\langle S^2 \rangle$ is a model dependent vartiable. Predictions from Tevatron estimated gap survival probability $\langle S^2 \rangle \approx 0.10$ for single diffraction process at the LHC which corresponds with the most current result for CMS $\langle S^2 \rangle = 0.12 \pm 0.04$ very well.

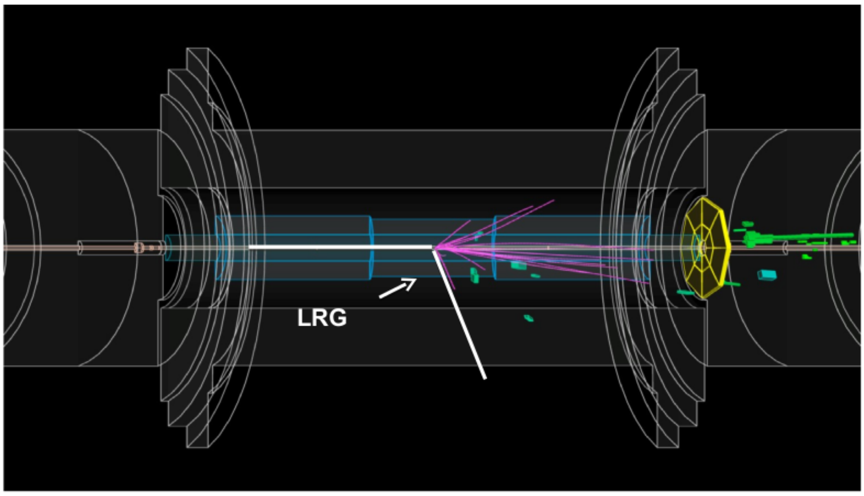

Figure 4: Large rapidity gap in ATLAS detector.

3.2 Forward protons

In forward processes particles (scattered protons) are produced at small polar angles with large rapidities and carry most of the energy of the interaction. These particles can not be detected by the central detector beacuse they propagate close to the beam through magnetic field in the pipe. Therefore special instruments are needed for manipulation with forward detectors, e.g. Roman Pots. On Figure 5 we can see different forward detectors of the CMS and ATLAS experiments placed up to 240 m from the central detector. There are also depicted currently realised projects to place the forward detectors to the distance of 420 m from central detectors.

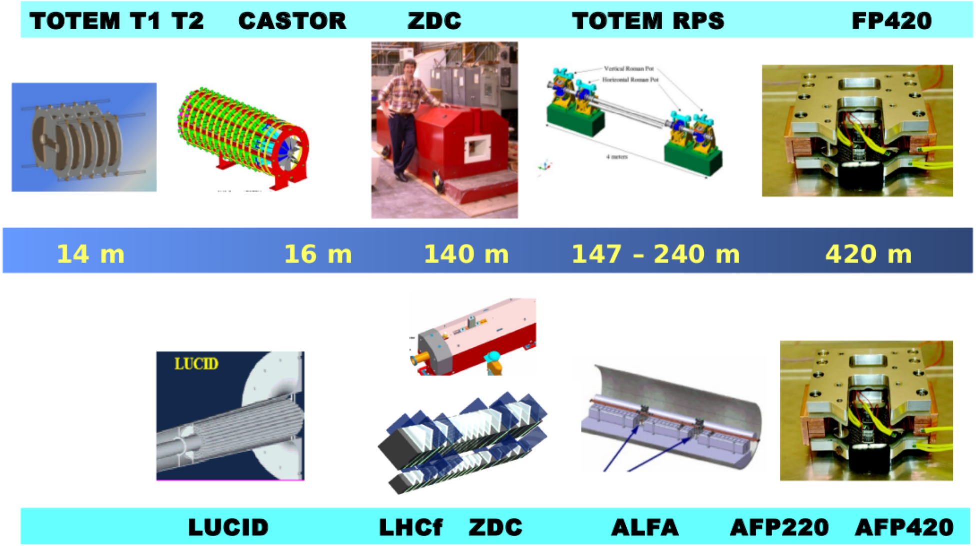

Figure 5: Forward detectors situated around the CMS (up) and ATLAS (down) detectors.

4 Conclusion

In this short paper we have been introduced to the theoretical description of the diffraction. We also mentioned the main contribution of results produced at HERA to the succesful derivation of diffraction PDFs. Experimental view was also presented with emphasis on the importance of rapidity gaps. Possible production of high p_T objects was mentioned. Amongst these the production of the jets in diffractive processes is in the spotlight and simulations of this case will be the crusious part of my bachelor thesis. Furthermore diffraction is also very insteresting phenomenom for providing a clear environment to observe the Higgs boson and as mentioned above, it is very important and unique tool for investigation of low-x structure of the proton. Also in high gluon density regime, diffraction is the key feature to investigate the saturation process and the state called ”color glass condensate”.

References

[1] M. Arneodo, M. Diehl, Diffraction for non-believers (2004-2005), arXiv:hep-ph/0511047v1.

[2] O. Kepka, QCD and Diffraction in the ATLAS Experiment at the LHC, Doctoral thesis (2009).

[3] R. Staszewski, Study of Diffraction with the ATLAS Detector at the LHC, Doctoral thesis (2013), HAL Id: tel-00772329.

[4] P. Růžička, Diffraction in the ATLAS experiment, Doctoral thesis (2012).

[5] T. Affolder et al. [CDF Collaboration], Phys. Rev. Lett. 84 (2000) 5043.

Vector meson photoproduction using color dipole approach

Jan Cepila*(jan.cepila@fjfi.cvut.cz)*

---

1 Introduction

One of still not understood part of QCD is how the transverse gluon profile of the proton looks like at very high energies. Large amount of inclusive data mainly from the deep inelastic scattering at HERA at small Bjorken x allows to test the high-energy limit of QCD. However, DIS is not sensitive to the particular transverse distribution of gluons. Therefore, it is advantageous to study complementary processes like vector meson production, which is more sensitive due to different form of the incident and conjugate wave function.

Consider a photon emitted from the proton with energy $w_{\pm} = \frac{M_V}{2}\exp(\pm|y|)$, where M_V is the mass of the vector meson, y is the rapidity of the vector meson in the lab frame and ± is there since there are two energies depending on which of the two incoming protons emitted the photon. According to the color dipole approach, this photon interacts strongly via one one of it's Fock states with the target proton in the frame, where the target proton is in rest. In the case of exclusive vector meson production this Fock state corresponds to the $q\bar{q}$ dipole. After the interaction, the coherent $q\bar{q}$ state forms a vector meson. The Bjorken-x and energy of the meson in the cms of the photon-proton system is

$$W_{\pm}^2 = 2w_{\pm}\sqrt{s} \qquad x_{Bj} = \frac{M_V^2}{W_{\pm}^2} = \frac{M_V}{\sqrt{s}}\exp(\mp|y|), \tag{1}$$

where $\sqrt{s}$ is the invariant cms energy of the collision and the momentum Δ lost by the outgoing proton is described via Mandelstam variable $t = (p' - p)^2$ as $\Delta = \sqrt{-t}$.

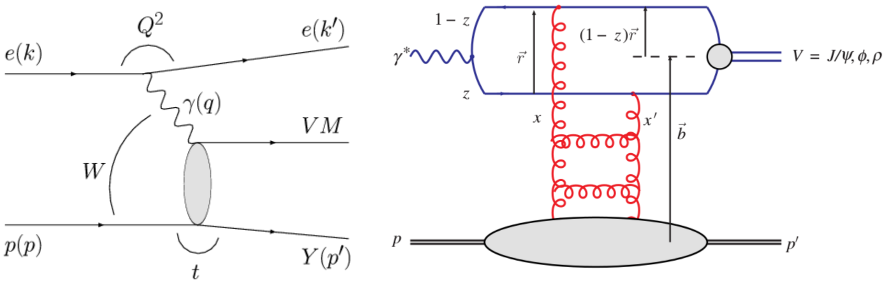

Figure 1: Interaction scheme of the vector meson production seen in the color dipole picture taken from [1].

2 Color dipole approach to vector mesons

The amplitude for production of a vector meson M_V is given by [1, 2]

$$\mathcal{A}_{T,L}^{\gamma^* p \to Mp}(x, Q, \Delta) = i \int \mathrm{d}^2 r \int_0^1 \frac{\mathrm{d}z}{4\pi} \int \mathrm{d}^2 b \, \Psi_M^* \Psi_{\gamma^*}\Big|_{T,L} e^{-i(\vec{b}-(1-z)\vec{r})\Delta} \frac{\mathrm{d}\sigma_{q\bar{q}}}{\mathrm{d}^2 b}, \tag{2}$$

where $\Psi_M^* \Psi_{\gamma^*}|_{T,L}$ is an overlap of a virtual photon and vector meson wave function, $\vec{r}$ is the transverse dipole size, $\vec{b}$ is the impact parameter of the dipole (transverse distance from the center of the proton to the center of mass of the dipole) and z is a part of photon momenta carried by one of the quarks from the dipole. The diffractive differential cross-section can be written as

$$\frac{\mathrm{d}\sigma_{T,L}^{\gamma^* p \to Mp}}{\mathrm{d}|t|} = \frac{1}{16\pi} \left| \mathcal{A}_{T,L}^{\gamma^* p \to Mp} \right|^2 \tag{3}$$

and the total cross-sections for $\gamma^* p$ scattering is obtained by the integration of the differential cross-sections over $|t| \in (0, 1)$.

Derivation of above formulas relies on the assumption that the S-matrix is purely real and so the amplitude $\mathcal{A}$ is purely imaginary. The real part of the amplitude can be accounted for by multiplying the differential cross-section by a factor $1 + \beta^2$ as in [3, 4], where

$$\beta = \tan(\pi\lambda/2) \qquad \lambda = \left| \frac{\partial \ln \mathcal{A}_{T,L}^{\gamma^* p \to Mp}}{\partial \ln \frac{1}{x}} \right|. \tag{4}$$

Note that in principle, the factor λ is different for transverse and longitudinal polarization. Nevertheless, the difference is of the order of 1%.

Finally, one has to incorporate the fact, that gluons attached to quarks in the $q\bar{q}$ dipole carry different light-front momenta fractions x and x' of the proton - the skewness effect. It is done by multiplying the cross-sections formula with factor $R_g(\lambda)$ [1]

$$R_g(\lambda) = \frac{2^{2\lambda+3}}{\sqrt{\pi}} \frac{\Gamma(\lambda + 5/2)}{\Gamma(\lambda + 4)} \tag{5}$$

This factor is obtained at NLO level in the limit $x' \ll x \ll 1$ and at small t assuming that the diagonal gluon density of the target has a power-law form. Note, that other definition of the skewedness factor use the actual gluon density $xg(x)$ instead of the dipole amplitude $\mathcal{A}$. Nevertheless, both definitions are consistent within common uncertainties[1].

The vector meson wave function is modelled with the presumption that vector meson is predominantly a quark-antiquark state and the spin and polarization structure is the same as in the photon case. The overlap of a virtual photon and vector meson wave function is

$$\begin{aligned} \Psi_M^* \Psi_{\gamma^*}\Big|_T &= e_f \delta_{f\bar{f}} e \frac{N_c}{\pi z(1-z)} \left(m_f^2 K_0(\epsilon r) \Phi_T(r,z) - (z^2 + (1-z)^2) \epsilon K_1(\epsilon r) \partial_r \Phi_T(r,z) \right) \\ \Psi_M^* \Psi_{\gamma^*}\Big|_L &= e_f \delta_{f\bar{f}} e \frac{N_c}{\pi} 2Qz(1-z) K_0(\epsilon r) \left(M_V \Phi_L(r,z) + \delta \frac{m_f^2 - \nabla_r^2}{M_V z(1-z)} \Phi_L(r,z) \right), \end{aligned} \tag{6}$$

where $e = \sqrt{4\pi\alpha_{em}}$, $\epsilon^2 = z(1-z)Q^2 + m_f^2$, $N_c = 3$ is the number of colors, m_f and $e_f \delta_{f\bar{f}}$ are the fractional charge and effective mass of the quark respectively and δ is a switch

enables to include the non-local part of the wave function introduced in [3, 5]. The scalar part $\Phi_{T,L}$ of the vector meson wave function is model dependent.
The Gauss-LC model [6] assumes that the longitudinal momentum fraction z fluctuates independently of the quark transverse momentum $\vec{k}$. This model assumes $\delta = 0$.

$$\begin{aligned}\Phi_T(r,z) &= N_T(z(1-z))^2 e^{-\frac{r^2}{2R_T^2}} \\ \Phi_L(r,z) &= N_L z(1-z) e^{-\frac{r^2}{2R_L^2}}\end{aligned} \tag{7}$$

Meson	$\hat{e}_f\delta_{f\bar{f}}$	$M_V[GeV]$	$m_f[GeV]$	N_T	$R_T^2[GeV^{-2}]$	N_L	$R_L^2[GeV^{-2}]$
J/Ψ	2/3	3.097	1.4	1.23	6.5	0.83	3.0
$\Upsilon(1S)$	1/3	9.46	4.2	0.78	1.91	0.78	1.91

Table 1: Vector meson wave function parameters for the Gauss-LC static part from [2, 7]. Note that only values for transversely polarized overlap wave function exist for Υ and the same values are taken also for longitudinal part to simplify the calculation.

The boosted Gaussian model [3, 4, 5, 8] assumes that the fluctuation of the quark three-momentum $\vec{p}$ in the rest frame of the meson can be written in a boost-invariant form $p^2 = (k^2 + m_f^2)/(4z(1-z)) - m_f^2$ and so

$$\Phi_{T,L}(r,z) = N_{T,L} z(1-z) e^{-\frac{m_f^2 R^2}{8z(1-z)} - \frac{2z(1-z)r^2}{R^2} + \frac{m_f^2 R^2}{2}} \tag{8}$$

This model has proper short distance limit and assumes $\delta = 1$.

Meson	$\hat{e}_f\delta_{f\bar{f}}$	$M_V[GeV]$	$m_f[GeV]$	N_T	N_L	$R^2[GeV^{-2}]$
J/Ψ	2/3	3.097	1.4	0.578	0.575	2.3
$\Upsilon(1S)$	1/3	9.46	4.2	0.481	0.480	0.57

Table 2: Table of vector meson wave function parameters for the boosted Gaussian static part from [2, 9]

Since most of parametrizations of the dipole cross-sections are independent of impact parameter b, one has to modify the formula for the scattering amplitude. Let's assume the transverse distribution of the gluonic density in the proton is T_g, then it is possible to separate[10]

$$\frac{\mathrm{d}\sigma_{q\bar{q}}}{\mathrm{d}^2 b} = 2N(x,r,b) = 2N(x,r)T_g(b) \qquad \sigma_{q\bar{q}}(x,r) = 2\int \mathrm{d}^2 b N(x,r) T_g(b) = \sigma_0 N(x,r) \tag{9}$$

The simplest form of the gluon profile function is a step function

$$T_g(b) = \Theta(b_s - b) \Rightarrow \sigma_0 = 2\pi b_s^2, \tag{10}$$

where $b_s = 4$ GeV^{-1}[2] is a parameter fixed by the average square transverse radius of the proton $\langle b^2 \rangle = \frac{b_s^2}{2}$. One can use also a Gauss distribution as a profile function

$$T_g(b) = \exp^{-\frac{b^2}{2B}} \Rightarrow \sigma_0 = 4\pi B \tag{11}$$

where the parameter $B = 5.59 GeV^{-2}$ is taken from [10]. The dependence of the cross-section on particular choice of the profile function is very strong and the correct profile function has to be modelled to data.
The dipole cross-section $\sigma_{q\bar{q}}(x, r)$ cannot be calculated from the first principles and has to be extracted from data. One can identify two limiting cases. The dipole cross-section behave like $\sim \rho^2$ at small separations $\rho \to 0$. However, at large separations the dipole cross-section is presumed to be saturated in order to suppress contributions from very large dipoles(black disc limit). Several parametrizations exist[2, 11, 12, 13, 14], but most of them do not take into account the QCD evolution of the gluon density. It can be, however, incorporated via the saturation phenomena.

3 Dipole cross-section from the CGC

It is known that gluon distribution inside the proton shows large increase of the number of gluons at fixed values of the virtuality, Q^2. The growth of the gluon density was understood to be due to gluon-branching processes described by the BFKL evolution equation. However, data suggest less gluons in a hadron than there should be according to the solution of BFKL equation. The unitarity of the cross section implies that the gluon density should stop growing at some point and a recombination of gluons occurs. This is known as saturation. The presence of recombination generates a scale, the so called saturation scale, $Q_s(x)$, which separates regions with linear rise of the gluon density from non-linear saturated regime.
A usual framework to study saturation phenomena is the Color Glass Condansate (CGC); an effective theory, which describes the high energy limit of QCD [15, 16]. The CGC generates a set of equations known as the JIMWLK equations. These equations are equivalent to a hierarchy of equations found by Balitsky[17]. In the limit of a large number of colours, the hierarchy reduces to one equation, which was independently derived by Kovchegov [18] within the colour dipole model. This equation, called the Balitsky-Kovchegov (BK) equation, describes the evolution in rapidity Y of the dipole scattering amplitude $N(r, Y)$ for the scattering of a colour dipole of transverse size r with a target

$$\frac{\partial N(r,Y)}{\partial \ln Y} = \int d\vec{r}_1 K(\vec{r},\vec{r}_1,\vec{r}_2)\Bigg(N(r_1,Y)+N(r_2,Y)-N(r,Y)-N(r_1,Y)N(r_2,Y)\Bigg),$$

where $\vec{r}_2 = \vec{r} - \vec{r}_1$. The kernel incorporating the running of the coupling is given by

$$K(\vec{r},\vec{r}_1,\vec{r}_2) = \frac{\alpha_s(r^2)N_C}{2\pi}\left(\frac{r^2}{r_1^2 r_2^2} + \frac{1}{r_1^2}\left(\frac{\alpha_s(r_1^2)}{\alpha_s(r_2^2)} - 1\right) + \frac{1}{r_2^2}\left(\frac{\alpha_s(r_2^2)}{\alpha_s(r_1^2)} - 1\right)\right),$$

with

$$\alpha_s(r^2) = \frac{12\pi}{(11 - \frac{2}{3}N_C)\ln\left(\frac{4C^2}{r^2\Lambda_{QCD}^2}\right)},$$

where N_C is the number of colours and C is a parameter to be fixed by comparing to data. The final ingredient to the rcBK equation is the initial condition. For the initial form of the dipole scattering amplitude we use the McLerran-Venugopalan model [19]:

$$N(r, Y=0) = 1 - \exp\left(-\frac{(r^2 Q_{s0}^2)^\gamma}{4}\ln\left(\frac{1}{r\Lambda_{QCD}} + e\right)\right) \tag{12}$$

with the values of the parameters Q_{s0}^2, C and γ taken from fit (e) in Table 1 of [20]. Note that in the fit the initial rapidity, $Y = 0$, is at $x_0 = 0.01$, where the relation between Y and x is $Y = \ln(x_0/x)$. The fit was performed under the assumption that $\alpha_s(r^2)$ freezes for values of r larger than r_0 defined by $\alpha_s(r_0^2) = 0.7$. We set Λ_{QCD} to 241 MeV.

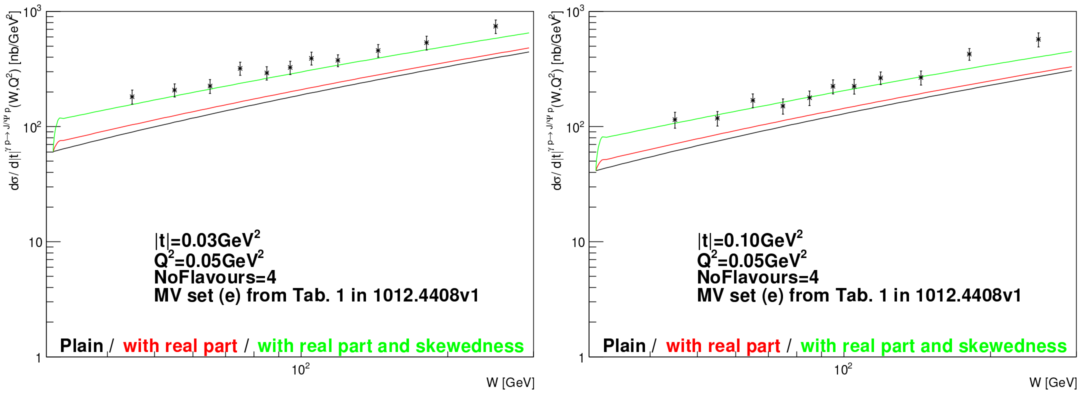

Figure 2: Results for J/Ψ photoproduction at fixed t compared to HERA data.

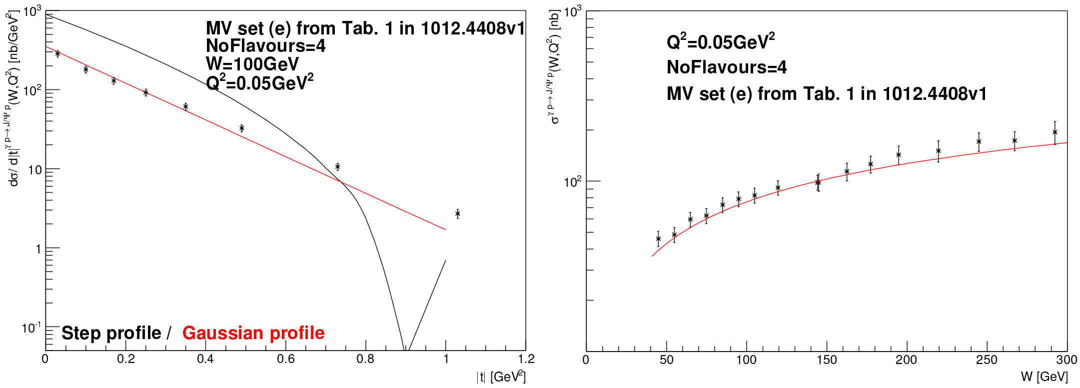

Figure 3: Left: Differential cross-section for J/Ψ photoproduction at fixed t for two different gluon profiles. Right: Total cross-section for the J/Ψ photoproduction compared to HERA data.

4 Conclusions

A model of vector meson photoproduction based on the color dipole approach was described with all it's essential parts. It is very successful in the description of data from HERA with only four free parameters. Saturation included dipole cross-sections based on Balitsky-Kovchegov equation was successfully implemented. The importance of the dependence of the dipole cross-section on the impact parameter is shown. The separation of the dipole scattering amplitude to two parts induces a need to know the transverse gluon profile of the proton and introduces one additional parameter. This parameter not only influence the overall normalization but also a shape of the predicted results. Let's denote that other possible separations of the dipole scattering amplitude exist, e.g. [10], but they are not compatible with the b-independent BK equation. The whole model is universal - predictions can be done for any energy and for most vector mesons. The importance of the skewedness correction is clearly visible with up to 50% contribution. On the other hand, the correction for the real part of the amplitude contributes up to 10%.

References

[1] N. Armesto and A. H. Rezaeian, Phys.Rev. **D90**, 054003 (2014), arXiv:1402.4831.

[2] H. Kowalski, L. Motyka, and G. Watt, Phys.Rev. **D74**, 074016 (2006), arXiv:hep-ph/0606272.

[3] J. Nemchik, N. N. Nikolaev, E. Predazzi, and B. Zakharov, Z.Phys. **C75**, 71 (1997), arXiv:hep-ph/9605231.

[4] J. R. Forshaw, R. Sandapen, and G. Shaw, Phys.Rev. **D69**, 094013 (2004), arXiv:hep-ph/0312172.

[5] J. Nemchik, N. N. Nikolaev, and B. Zakharov, Phys.Lett. **B341**, 228 (1994), arXiv:hep-ph/9405355.

[6] H. G. Dosch, T. Gousset, G. Kulzinger, and H. Pirner, Phys.Rev. **D55**, 2602 (1997), arXiv:hep-ph/9608203.

[7] G. S. dos Santos and M. V. T. Machado, (2014), arXiv:1411.7918.

[8] S. J. Brodsky, T. Huang, and G. P. Lepage, (1980).

[9] L. Motyka and G. Watt, Phys. Rev. **D78**, 014023 (2008), arXiv:0805.2113.

[10] T. Lappi and H. Mantysaari, Phys. Rev. **C83**, 065202 (2011), arXiv:1011.1988.

[11] K. J. Golec-Biernat and M. Wusthoff, Phys.Rev. **D59**, 014017 (1998), arXiv:hep-ph/9807513.

[12] K. J. Golec-Biernat and M. Wusthoff, Phys.Rev. **D60**, 114023 (1999), arXiv:hep-ph/9903358.

[13] E. Iancu, K. Itakura, and S. Munier, Phys. Lett. **B590**, 199 (2004), arXiv:hep-ph/0310338.

[14] H. Kowalski and D. Teaney, Phys. Rev. **D68**, 114005 (2003), arXiv:hep-ph/0304189.

[15] L. D. McLerran and R. Venugopalan, Phys.Rev. **D49**, 2233 (1994), arXiv:hep-ph/9309289.

[16] L. D. McLerran and R. Venugopalan, Phys.Rev. **D49**, 3352 (1994), arXiv:hep-ph/9311205.

[17] I. Balitsky, Nucl.Phys. **B463**, 99 (1996), arXiv:hep-ph/9509348.

[18] Y. V. Kovchegov, Phys.Rev. **D60**, 034008 (1999), arXiv:hep-ph/9901281.

[19] L. D. McLerran and R. Venugopalan, Phys.Lett. **B424**, 15 (1998), arXiv:nucl-th/9705055.

[20] J. L. Albacete, N. Armesto, J. G. Milhano, P. Quiroga-Arias, and C. A. Salgado, Eur.Phys.J. **C71**, 1705 (2011), arXiv:1012.4408.

J/ψ production in heavy-ion collisions at STAR

Jana Fodorová (*fodorjan@fjfi.cvut.cz*)

1 Introduction

In the collisions of heavy nuclei, at high energies such as those achievable at the Relativistic Heavy Ion Collider (RHIC) at Brookhaven National Laboratory, the nuclear matter may undergo a phase transition from hadrons to a state of deconfined quarks and gluons, the quark-gluon plasma (QGP).

Due to the color screening of the quark-antiquark potential in the QGP the production of heavy quarkonia[1] (e.g. J/ψ, Υ) is expected to be suppressed [1]. However, there are also other effects that may influence the observed quarkonium yields (secondary production in the QGP, feed-down effects, cold-nuclear-matter effects). Not all of these effects are related to the presence of the QGP and thus complicate the suppression picture. Moreover, the quarkonium production mechanism in elementary collisions is still not completely understood. For these reasons we need to study different quarkonium states in various colliding systems, at different collision energies and centralities.

At the STAR experiment at RHIC, hot-medium effects on J/ψ production have been studied in Au+Au collisions at $\sqrt{s_{\mathrm{NN}}}$ = 39, 62.4, 200 GeV [2, 3, 4] and in U+U collisions at $\sqrt{s_{\mathrm{NN}}}$ =193 GeV. Since U nuclei are larger than Au nuclei, the energy density of the created medium is expected to be higher in U+U collisions than in Au+Au collisions, particularly in the most central collisions [5]. Thus they allow for further studying of the hot-medium effects.

In this work current status of J/ψ analysis in central U+U collisions and recent results on J/ψ production in heavy-ion collisions at STAR are presented.

2 Experimental setup

The Solenoidal Tracker at RHIC (STAR) [6] specializes in tracking and identification of charged particles at mid-rapidity and with 2π coverage in azimuth. In the work presented here J/ψ has been studied via the electron-positron decay channel, $J/\psi \rightarrow e^+e^-$ with a branching ratio $B_{\mathrm{ee}} = 5.9$ %. The STAR Time Projection Chamber (TPC) [7], Time of Flight (TOF) [8] detector and Barrel Electromagnetic Calorimeter (BEMC) [9] were used for electron identification.

TPC provides tracking and particle identification via the specific energy loss $\mathrm{d}E/\mathrm{d}x$ of particles, TOF measures $1/\beta$ and together with TPC enables separation of electrons

---

[1] bound states of heavy quarks and their anti-quarks

from hadrons up to ~ 1.4 GeV/c. BEMC measures energies of electromagnetic showers and thus enables electron-hadron separation via energy-to-momentum E/pc ratio. For electrons $E/pc \sim 1$ while for hadrons $E/pc < 1$. It is also used to trigger on high-p_{T} electrons, the so called High Tower (HT) trigger.

The 0-5% most central data are selected using the information about energy of spectator neutrons measured by Zero Degree Calorimeters and track multiplicity information from TOF.

3 Data analysis

115 M of 0-5% most central U+U collisions collected in 2012 at $\sqrt{s_{\mathrm{NN}}} = 193$ GeV were used in the analysis presented here. Candidates on electrons and positrons from J/ψ decay were selected from good-quality tracks with transverse momenta $p_{\mathrm{T}} > 1.0$ GeV/c which satisfied selection criteria on TPC, TOF and BEMC signals:

- the difference from the expected ln $(\mathrm{d}E/\mathrm{d}x)$ for electrons expressed in terms of standard deviation units, $n\sigma_{\mathrm{e}}^{\mathrm{TPC}}$, was required to be in the range (-1.5, 2.0);
- $1/\beta^{\mathrm{TOF}}$ of particles with momenta $p < 1.4$ GeV/c was required to be in the range (0.970, 1.025), for particles with $p > 1.4$ GeV/c the TOF cut was used if particles had a signal in TOF;
- the energy E deposited in the BEMC tower had to be larger than 0.15 GeV and the ratio pc/E^{BEMC} had to be in the range (0.7, 2.0).

4 Results

J/ψ signal was reconstructed from the invariant mass distributions of the e^{+} e^{-} pairs. Combinatorial background of the J/ψ signal was estimated by the mixed-event background method, i.e. by combining the electrons with positrons from different events. After the combinatorial background subtraction the invariant mass distribution of the e^{+} e^{-} pairs was fitted with a crystal ball function to describe the signal and a linear function was used to describe the residual background.

Figure 1 shows J/ψ signal after combinatorial background subtraction and fit for the signal and the background for p_{T} integrated in 0-5% most central U+U collisions. The J/ψ raw yield calculated by the bin counting method in the invariant mass region (2.9, 3.2) GeV/c^{2} was 4960 ± 580 with a significance of $\sim 8.6\,\sigma$ in 0-5% most central U+U collisions.

Modification of J/ψ production in heavy-ion collisions is quantified by the so called nuclear modification factor R_{AA} defined as the ratio of J/ψ yield produced in nucleus+nucleus collisions compared with the yield in proton+proton collisions scaled by the number of binary collisions. Data analysis leading to the extraction of J/ψ nuclear modification factor in 0-5% most central U+U collisions is being performed currently, namely reconstruction efficiency studies.

Here we mention recent results of similar analyses on J/ψ nuclear modification factor in Au+Au and U+U collisions at STAR [2, 3, 4]. Figure 2 (left panel) shows R_{AA} as a function of p_{T} in minimum bias and HT triggered Au+Au and U+U collisions [2].

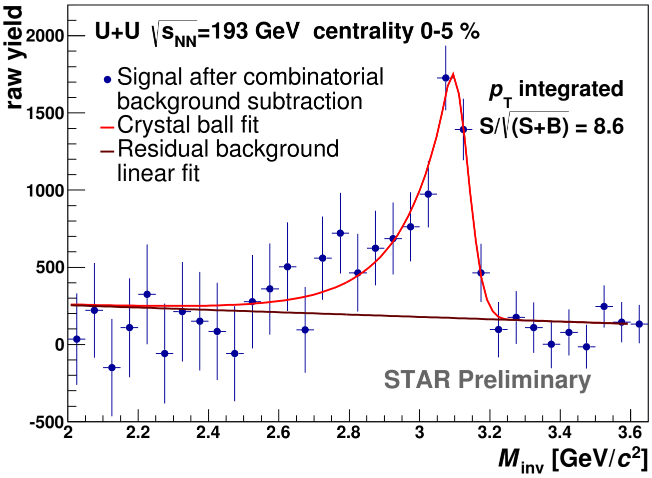

Figure 1: J/ψ signal after combinatorial background subtraction fitted with a crystal ball function (signal shape) together with a linear function (residual background) in 0-5% most central U+U collisions.

In the right panel of Figure 2 the nuclear modification factor of J/ψ is presented as a function of the number of nucleons participating in collision N_{part}. Results are shown for different colliding energies $\sqrt{s_{\text{NN}}} = 200$, 62.4 and 39 GeV in Au+Au collisions [2] and for $\sqrt{s_{\text{NN}}} = 193$ GeV in minimum bias U+U collisions. U+U results are consistent with Au+Au results with similar N_{part}, within errors.

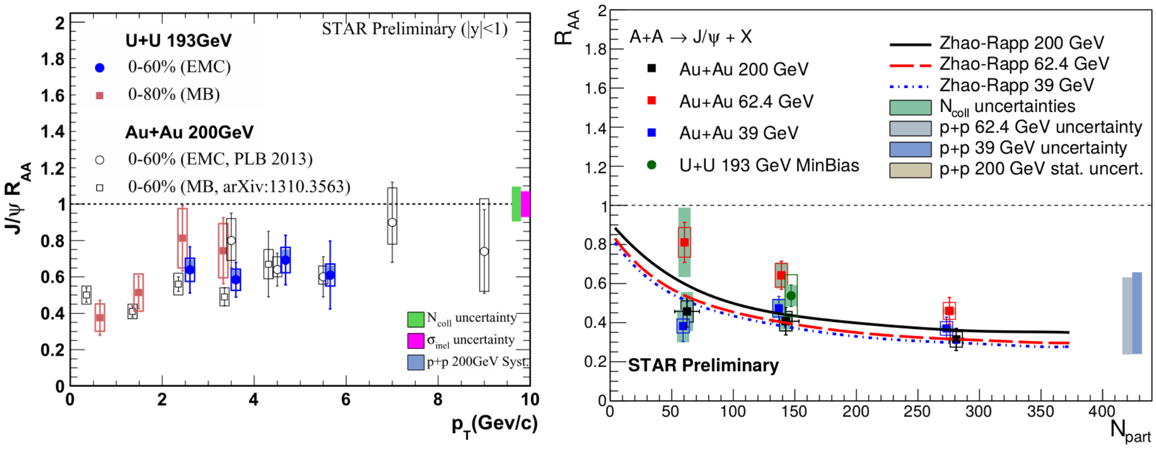

Figure 2: Left: J/ψ R_{AA} as a function of p_{T} in minimum bias and HT triggered U+U and Au+Au collisions [2]. Right: J/ψ R_{AA} as a function of N_{part} in Au+Au collisions at $\sqrt{s_{\text{NN}}} = 200$ (black), 62.4 (red) and 39 (blue points) GeV [2] and compared with model predictions [10] and in minimum bias U+U collisions at $\sqrt{s_{\text{NN}}} = 193$ GeV (green points).

5 Summary

The status of J/ψ production analysis in 0-5% most central U+U collisions has been presented. A strong signal of J/ψ has been observed. J/ψ reconstruction efficiency is currently being studied leading to the extraction of J/ψ nuclear modification factor in 0-5% most central U+U collisions.

We have also presented results on modification of J/ψ production in minimum-bias U+U collisions and Au+Au collisions at the STAR experiment. Suppression of J/ψ production is similar in both colliding systems.

References

[1] T. Matsui and H. Satz, *J/ψ Suppression by Quark-Gluon Plasma Formation, Phys.Lett.* **B178** (1986) 416.

[2] **STAR** Collaboration, W.M. Zha, *Recent measurements of quarkonium production in p+p and A+A collisions from the STAR experiment*, *Nuclear Physics* **A931** (2014) 596-600.

[3] **STAR** Collaboration, L. Adamczyk et al., *J/ψ production at low p_T in Au+Au and Cu+Cu collisions at $\sqrt{s_{NN}} = 200$ GeV at STAR, Phys.Rev.* **C90** (2014) 024906, [arXiv:1310.3563].

[4] **STAR** Collaboration, L. Adamczyk et al., *J/ψ production at high transverse momenta in p+p and Au+Au collisions at $\sqrt{s_{NN}} = 200$ GeV, Phys.Lett.* **B722** (2013) 55-62, [arXiv:1208.2736].

[5] D. Kikola, G. Odyniec, and R. Vogt, *Prospects for quarkonia production studies in U+U collisions, Phys.Rev.* **C84** (2011) 054907, [arXiv:1111.4693].

[6] **STAR** Collaboration, K. Ackermann et al., *STAR detector overview, Nucl.Instrum.Meth.* **A499** (2003) 624-632.

[7] M. Anderson, J. Berkovitz, W. Betts, R. Bossingham, F. Bieser, et al., *The Star time projection chamber: A Unique tool for studying high multiplicity events at RHIC, Nucl.Instrum.Meth.* **A499** (2003) 659-678, [nucl-ex/0301015].

[8] **STAR** Collaboration, W. Llope, *Multigap RPCs in the STAR experiment at RHIC, Nucl.Instrum.Meth.* **A661** (2012) 110-113.

[9] **STAR** Collaboration, M. Beddo et al., *The STAR barrel electromagnetic calorimeter, Nucl.Instrum.Meth.* **A499** (2003) 725-739.

[10] X. Zhao and R. Rapp, *Charmonium in Medium: From Correlators to Experiment, Phys.Rev.* **C82** (2010) 064905, [arXiv:1008.5328].

J/Ψ and $\Psi(2s)$ production in ultra-peripheral collisions

Zuzana Gajdošová*(gajdosova.zuzana23@gmail.com)*

This proceeding will present a brief introduction to ultra-peripheral collisions (UPC). The results of J/ψ and $\psi(2S)$ photoproduction by the Phenix, CMS and ALICE collaborations. A preview of the tasks of my Bachelor's thesis will also be presented.

The large hadron collider (LHC) is able to accelerate charged particles to a speed near to the speed of light. A fast particles like these carries a boosted electromagnetic field, which Enrico Fermi called the flux of virtual photons in 1924, [1].

When these charged particles collide in a way such that the impact parameter is larger than the sum of their radii, they interact via photons. These are the events called UPC. For the case where the charged particles are nuclei, the interaction can proceed in two general ways. The first one is when a radiated photon from the heavy-ion from one beam interacts directly with another heavy-ion from another beam, see Figure 1 (b). The second manner is when each heavy-ion in opposite beams radiate photons and these photons interact with each other, see Figure 1 (a). The cross section of such events is large, because the photon flux grows with the square of the charge Z^2.

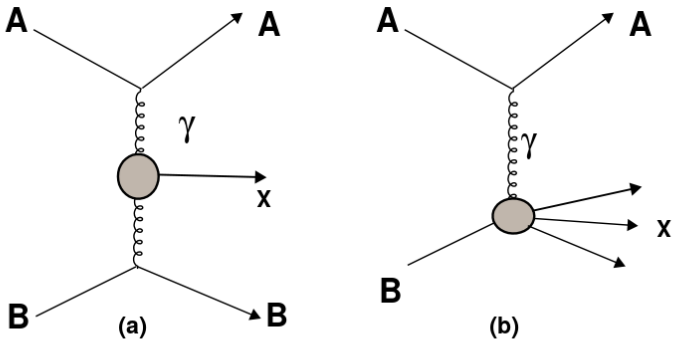

Figure 1: Electromagnetic interaction of two ions mediated by radiated photons.

New particles are created in UPC. What we are focusing on is exclusive photoproduction of vector mesons, i.e J/ψ, $\psi(2S)$, ϕ, etc., and generaly this process is the most commonly studied process in UPC at ALICE. The vector mesons from exclusive processes have a small associated background and thus a clear signal. These processes allow to study the distribution of gluons in the target, i.e. heavy-ion, at small Bjorken-x and therefore lead to a better understanding of Quantum Chromodynamics (QCD).

The first exclusive photoproduction of J/ψ decaying into e^+e^- ever measured in nucleus-nucleus UPC, particularly in Au-Au collisions, was obtained by the PHENIX experiment at BNL, [2]. The results were published in 2009. Although the statistical errors are quite large and do not permit to extract strong conclusions from the measurement, it is a clear sign showing that this kind of physics can be made in heavy-ion colliders.

Another experiment which provides a study of UPC in nucleus-nucleus collision $Pb + Pb \to Pb+Pb+J/\psi$ is CMS at CERN [3]. Since CMS detector has much material, it is not able to measure J/ψ at central rapidity and reports only results at semi-forward rapidity. ALICE is capable of detecting particles both in central rapidities and in forward rapidities. There are some theories which attempt to describe the data. These theories can be divided into some groups according to its character. The one which counts for Strong Shadowing like AB-EPS08, GDGM-strong shadowing and GZ - LTA theories. Then there exits theories which include Moderate Gluon Shadowing like GDGM -Moderate shadowing, AB-EPS08, theories with no gluon shadowing as following: LM and STARLIGHT and finally the group of theories which counts for Impulse approximation, i.e. no nuclear effects at all. To the final group pertain STARLIGHT-No Nuclear Eff. and AN MSTW08 theories. The CMS and ALICE results show that the theories which include moderate gluon shadowing describe the data, while strong shadowing underestimates the data and the Impulse Approximation overestimates these data. The data were taken at the energy of $\sqrt{s_{NN}} = 2.76$ TeV.

The theory which counts for moderate shadowing, AB-EPS09 fits well the data for the measured cross section of the J/ψ at mid rapidity; $\mathrm{d}\sigma^{coh}_{J/\Psi}/\mathrm{d}y = 2.38^{+0,34}_{-0,24}$ (sta+sys) mb.

It is expected that with data from Run2 the theoretical model will be even more constrained.

ALICE also measured the cross section of $\psi(2S)$ and showed that models with moderate shadowing are able to reproduce the measurement, [5].

The ratio of UPC cross section of J/ψ to $\psi(2S)$ shows a surprising result, see Figure 2. The point measured by ALICE in Pb-Pb collisions is 2σ larger than the other points. The question is what would cause this shift, if there are nuclear effects and gluon shadowing which modify J/ψ and $\psi(2S)$ in different way. Run2 would help to decide if it is a real result or a statistical fluctuation, which is also one of the tasks of my Bachelor's thesis.

The name of my Bahelor's thesis is the following: *Exclusive photoproduction of vector meson $\psi(2S)$ in Pb-Pb collisions in ALICE with Run2 data.* This means that I will have a first look at $\psi(2S)$ with Run2 data. Since Run2 has higher luminosity $\approx 138\ \mu b^{-1}$ in comparison wih Run1 $\approx 22\ \mu b^{-1}$, we expect better statistics which will serve to decrease the uncertainty of the data, see Figure 3, and thus put more constraints on the theories. The energy at which Pb-Pb collide in Run2 is 5.02 TeV which is twice the energy of Run1. This implies that we would be able to study gluon distribution in hadrons at even smaller Bjorken-x, lower by a factor of 2 and thus understand more QCD.

Another task of my bachelor thesis is to reproduce the results obtained in Run1.

References

[1] Fermi E Z. Physik 29:315 (1924)

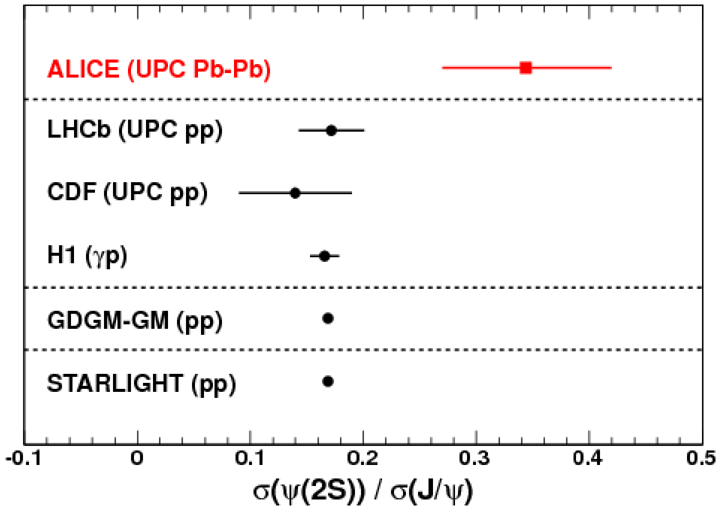

Figure 2: The ratio of UPC cross section of J/ψ to $\psi(2S)$, taken from [5].

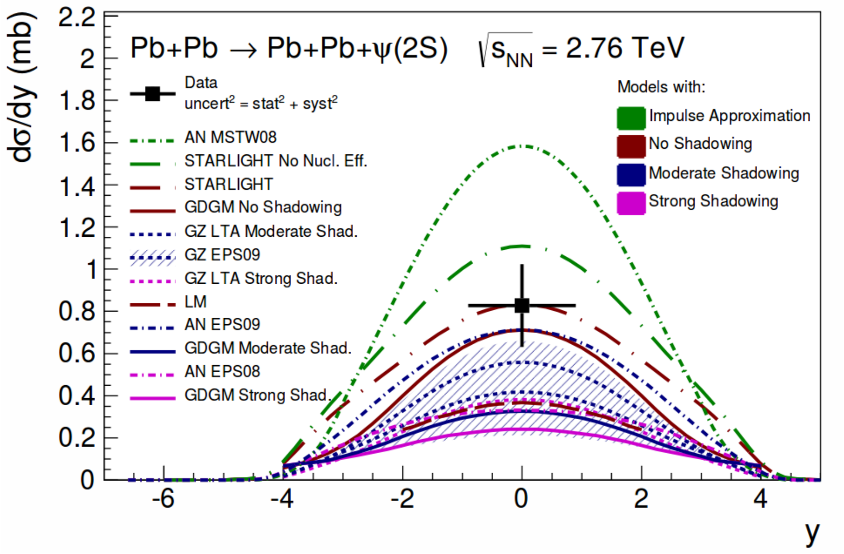

Figure 3: The $\psi(2S)$ in Pb-Pb collisions in ALICE, taken from [5].

[2] PHENIX Coll., A. Afanasiev, et al, Phys.Lett.B679:321-329 (2009)

[3] CMS Coll., CMS-PAS-HIN-12-009

[4] ALICE: Phys.Lett. B718 (2013) 1273 Eur. Phys. J. C (2013) 73:2617

[5] ALICE Coll., arXiv:1508.05076v1

Eliptic flow of J/ψ meson in $U+U$ collisions at STAR experiment

Alena Harlenderová *(harleale@fjfi.cvut.cz)*

1 Introduction

The analysis of the azimutal anisotropy in non-central collisions is one of the most important instrument for studying properties of matter created in heavy ion collisions. The azimutal distribution (anistrophic flow) of particle momentum is expected to be sensitive to early stages of the collision. The azimuthal part of momentum distribution can be decomposed by using the Furier transform. The second Fourier coefficient v_2 is called elliptic flow. Studying J/ψ eliptic flow can shed more light on the production of J/ψ and interaction of J/ψ with the hot deconfined medium.

2 Non-central collisions and anisotrophic particle flow

The azimutal distribution (anistrophic flow) of produced particles is expected to be sensitive to early stages of the collision [2]. There is considerable azimutal anisotrophy in spatial distribution of matter in non-central collisions. The medium is in the shape of ”almond” due to the initial geometry of the collision and is thermalized briefly after the collision. Initial azimuthal anisotrophy results in a preassure gradient which has different magnitude at different places of the transverse plane, as is depicted in the Figure 1. The thermalized medium expands and the expansion is faster in a direction of the largest gradient. In the other words, particles are in average more accelerated in this direction and have significant values of transverse momentum p_T. Overall, the initial azimuthal anisotrophy in distribution of matter results in the anisotrophy in the azimuthal distribution of momentum of emitted particles.

3 Decomposition of azimuthal part of momentum distribution

The azimuthal part of momentum distribution can be decomposed by using the Furier transform with respect to the reaction plane (plane defined by the centres of nuclei and the beam direction).

$$E\frac{d^3N}{d^3p} = \frac{1}{2\pi}\frac{d^2N}{p_T dp_T dy}\left(1 + \sum_{i=1}^{\infty} 2v_n \cos(n(\phi - \Phi^{RP}))\right),$$

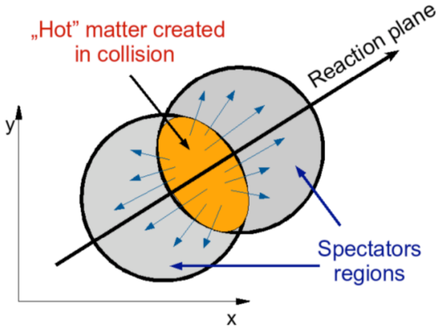

Figure 1: Transverse plane of the relativistic heavy ion collision [5].

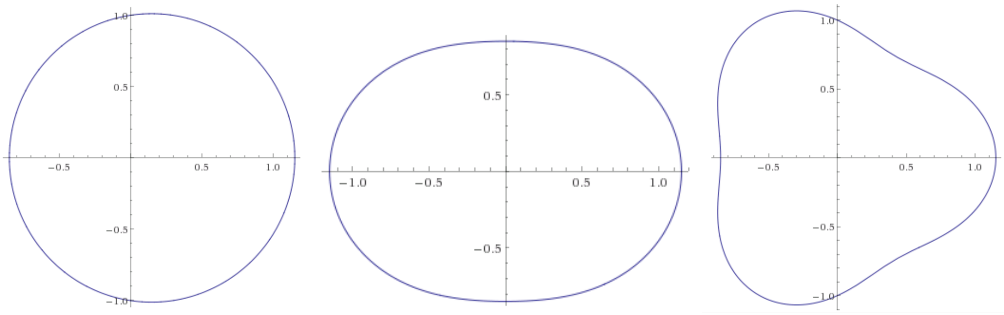

Figure 2: The distribution corresponding to direct flow with $v_1 = 0,15$ (the picture on the left),$v_2 = 0,15$ (the picture in the middle) and $v_3 = 0,15$ (on the right). The figure is taken from [4].

where N is number of particles, E energy, y rapidity, v_n n-th Fourier coefficient, ϕ azimuthal angle and Φ^{RP} the azimuthal angle of reaction plane.

Coefficients v_n correspond to the various modifications of the momentum distribution. The flow corresponding to the first Fourier coefficient v_1 is called direct flow, the second Fourier coefficient v_2 is called elliptic flow, third v_3 triangular flow. The distributions corresponding to $1 + 0,15 \cdot \cos\phi$, $1 + 0,15 \cdot \cos 2\phi$ and $1 + 0,15 \cdot \cos 3\phi$ can be seen in the Figure 2. Here we are going to discuss elliptic flow.

4 Eliptic flow of particles containing of light and strange quarks

It was shown that the particles composed of light and strange quarks have the positive value of v_2 for higher p_T. It can be seen for exapmle in the Figure 3. It shows v_2 as a function of p_T at mid-rapidity for $\pi^{\pm}, K^{\pm}, p, \bar{p}, \Lambda, \bar{\Lambda}, \phi, K^0_s, \Xi^-$ and $\bar{\Xi}^+$ in Au+Au collisions at $\sqrt{s_{NN}} = 7.7, 11.5, 19.6, 27, 39$ and 62.4GeV [2]. A similar pattern of v_2 was observed for all mentioned particles. v_2 increases with p_T from v_2 close to zero value to the maximum between 0.6 and 2.2. The maximum v_2 is higher for higher beam energies and is smaller for mesons than for hadrons [2].

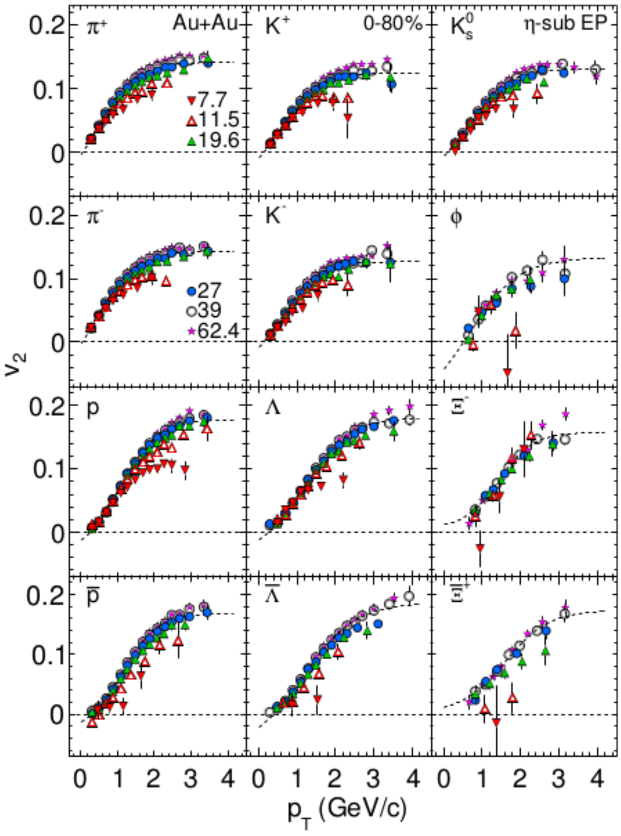

Figure 3: v_2 as a function of p_T at mid-rapidity for $pi^{\pm}, K^{\pm}, p, \bar{p}, \Lambda, \bar{\Lambda}, \phi, K_s^0, \Xi^-$ and $\bar{\Xi}^+$ in Au+Au collisions at $\sqrt{s_{NN}} = 7.7, 11.5, 19.6, 27, 39$ and 62.4GeV. The figure is taken from [2].

5 Eliptic flow of J/ψ

Particles from Figure 3 are all composed of light and strange quarks that are deconfined and thermalized in Quark-Gluon plasma and interact strongly with their surronudings. However, particles such as quarkonia are expected be formed in the early stage of collision before thermalization. They are tightly bound, thus they may survive the whole evolution in the form of colourless mesons. Thus, they should not be thermalized like asymptically free quarks. However, situation is not so simple. Quarkonia can be formed for example also during hadronisation. The quarks of these quarkonia are present in QGP like single quarks and consequently can be easily thermalized. Thus, studying J/ψ eliptic flow can shed more light on the production of J/ψ and interaction of J/ψ with the hot deconfined medium.

Here we are going to discuss one method that can be used for v_n calculation, the standard event plane method [1].

6 Event plane method

Since the reaction plane is not known, we can only estimate it. The estimation is called the event plane.

At first, we need to calculate the 2-D event flow vector $\vec{Q}_n$ in the transverse plane, which lies in the event plane.

$$Q_{x,n} = \sum_i w_i \cos(n\phi_i) = Q_n \cos(n\Phi_n)$$

$$Q_{y,n} = \sum_i w_i \sin(n\phi_i) = Q_n \sin(n\Phi_n)$$

i goes ower all particles of event. w_i is the weight for i-th particle. It is common to use transverse momentum p_T as the weight. ϕ_i is the laboratory angle of the particle flight.

Afterwards, the event plane angle can be calculated as

$$\Phi_n = \frac{\arctan 2(Q_{n,y}, Q_{n,x})}{n}.$$

The observed coeficient can be obtained by formula

$$v_n^{obs}(p_T, y) = \langle \cos[n(\phi_i - \Phi_n)] \rangle,$$

where $\langle\rangle$ donates the an average over all particles in all events.

We do not have the infinite number of particles, therefore v_n have to be corrected by the event plane resolution

$$\mathcal{R}_n = \langle \cos[n(\Phi_n - \Phi_{RP})] \rangle.$$

v_n can be obtained by

$$v_n = \frac{v_n^{obs}}{\mathcal{R}_n}.$$

However, we do not know the reaction plane angle used in the formula for $\mathcal{R}_n$ calculation. Thus, the $\mathcal{R}_n$ can be obtained by following iterative method. We randomly devide the events to two subevents with the same multiplicity and obtain the event plane resolution for these subevents:

$$\mathcal{R}_{n,sub} = \sqrt{\langle \cos[n(\Phi_n^A - \Phi_n^B)] \rangle}.$$

The event plane resolution can be estimated by

$$\mathcal{R}_{n,full}(\chi) = \mathcal{R}(\sqrt{2}\chi_{sub}),$$

where $\chi_{sub} = v_{n,sub}\sqrt{M} = \frac{v_{n,sub}^{obs}}{\mathcal{R}_n^{obs}}\sqrt{M}$. M is a number of particles in a subevent. The first approximation is given by $\mathcal{R}_{full} \approx \sqrt{2}\mathcal{R}_{sub}$. We can further iterate by substituting $\mathcal{R}_{full}$ in $\chi = v_n\sqrt{M}$ and calculation of

$$\mathcal{R}_k(\chi) = \frac{\sqrt{\pi}}{2}\chi \exp\left(\frac{-\chi^2}{2}\right)\left(I_{(k-1)/2}\left(\frac{\chi^2}{2}\right) + I_{(k+1)/2}\left(\frac{\chi^2}{2}\right)\right),$$

where I donates modified Bessel function. This method is taken from [1].

7 J/ψ v_2 in AuAu collisions at $\sqrt{s_{NN}} = 200$GeV

J/ψ v_2 was analysed in AuAu collisions at $\sqrt{s_{NN}} = 200$GeV performed at STAR experiment [2]. In the upper panel of the Figure 4 the obtained J/ψ v_2 can be seen together with charged hadron and ϕ v_2 from the same collisions. We can observe that charged hadron and ϕ v_2 are considerably higher than J/ψ v_2. Moreover, J/ψ v_2 is consistent with non-flow estimation (green area). There is J/ψ v_2 compared to the various model estimations in the lower pannel of the Figure 4. We can see that J/ψ is probably not mostly produced by the coalescence according to the data.

References

[1] S. A. Voloshin, A. M. Poskanzer, R. Snellings, Collective phenomena in non-central nuclear collisions, arXiv:0809.2949

[2] L. Adamczyk at. all, Elliptic flow of identified hadrons in Au+Au collisions at $\sqrt{s_{NN}}$= 7.7–62.4 GeV, arXiv:1301.2348

[3] Hao Qiu, STAR High Level Trigger and J/ψ Elliptic Flow, Ph.D. Thesis

[4] https://www.wolframalpha.com , WolframAlpha, (1.2.2016)

[5] D. Kikola, Hidden charm production in the relativistic heavy ion collisions registered in the STAR experiment, Ph.D. Thesis

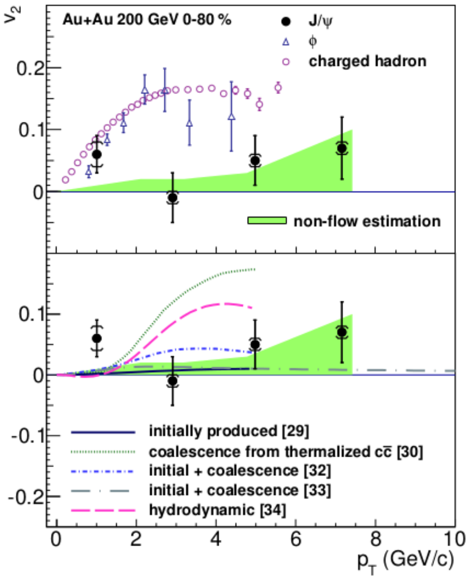

Figure 4: J/ψ v_2 for AuAu collisions at $\sqrt{s_{NN}} = 200$GeV performed at STAR experiment. The upper panel: J/ψ v_2 together with charged hadron and ϕ v_2 from the same collisions. The lower pannel: J/ψ v_2 compared to the various model estimations. The figure is taken from [3]

Photoproduction of ρ^0 in Ultra-peripheral collisions at ALICE

David Horák*(david.horak@cern.ch)*

The LHC is not only the most powerful collider for proton-proton and heavy-ion collisions, but it is also the most powerful source of photon collisions. The accelerated protons and ions carry an electromagnetic field, which can be viewed as a beam of photons. The photon-photon and photon-proton (or ion) processes can be studied in ultra-peripheral collisions (UPC). These processes, in particular photoproduction of vector mesons, offer an unique opportunity to study fundamental interactions in QED and QCD.

A collision of two particles is characterized by an impact parameter b, which is defined as the perpendicular distance between the path of the two particles. When two highly accelerated particles collide with an impact parameter larger than the sum of nuclear radii, the strong interaction is suppressed due to its short range and only electromagnetic interactions may occur. This we call an ultra-peripheral collision. The electromagnetic field of relativistic nuclei is contracted and its intensity (and the number of virtual photons surrounding the nucleus) is proportional to Z^2 [1].

In ultra-peripheral collisions the ρ^0 meson is produced by a process called photoproduction. In proton-lead collisions, the lead is the source of photon and the proton is the target. The photoproduction of ρ^0 can be elastic or dissociative. In the former, the proton remains in its ground state, in the latter case it breaks up. The ρ^0 meson decays dominantly into a $\pi^+\pi^-$ pair.

The ALICE experiment at the LHC provides a great oportunity to study ultra-peripheral collisions thanks to its good resolution at low p_T. A typical UPC event is characterized by a small number of tracks. Because of low number of tracks, there is lot of beam-gas background events. It can be cutted by the V0 detectors, which should by empty when the ρ^0 is produced. Then pions are identified by means of ionization losses in a time projection chamber (TPC). Also these events should have opposite charge. If not, it means that there are lost tracks and those ones can be used to determine the number of lost good tracks. An important role play zero degree calorimeters, which show signal if the proton breaks up. Therefore they can be used to determine the number of non-exclusive candidates. The invariant mass of $\pi^+\pi^-$ pair has not a Breit-Wigner shape due to two pion non-resonant production. This shape can be described by the Söding formula or by the Ross-Stodolski formula [2].

For Run 2 new detectors at ALICE were installed. One of them was ALICE Diffractive (AD) Detector, which is formed by two scintillation arrays on both sides (ADA and ADC). The ADA covers a pseudorapidity interval: $4.8 < \eta < 6.3$ while the ADC covers: $-7.0 < \eta < -4.9$ [3].

Each AD detector consist of 8 cells of scintillation plastic of about $22 \times 22 \times 2.5$ cm in two layers working in coincidence. The light produced by scintillators is collected by Wave Length Shifting bars attached on sides of each cell, which transfer the collected light trough optical fibres to the photomultipliers. These provides two signals: one, amplified by a factor of 10, which is used for L0 trigger timing measurement, the other, direct signal, is used for charge integration. The main task of AD detector is to extend V0 veto in higher rapidities and provide trigger for UPC and for diffractive physics.

The exclusive production of ρ^0 meson was never measured in p-Pb ultra-peripheral collision, so it is very attractive topic. Also the results can be compared with Pb-Pb collisions in ALICE and with photoproduction of ρ^0 at HERA accelerator. The new data from Run 2 will provide much higher statistics and open the possibility of study photoproduction of particles that was never studied in ultra-peripheral collisions.

References

[1] Bertulani Carlos A., et. al, Physics of Ultra-Peripheral Nuclear Collisions, arXiv:nucl-ex/0502005v2, 2005.

[2] Mayer C., Coherent Photo-Production of ρ^0 Vector-Mesons and of e^+e^- pairs in Ultra-peripheral Pb-Pb Collisions at $\sqrt{s_{NN}} = 2.76$ TeV, ALICE Internal Notes, 2014.

[3] Herrera Corral G., Diffractive Physics with ALICE at the LHC: the control of quantum collisions. Conference Series 624 (2015) 012008. 2015.

Rydberg atoms and their use in experiment AEgIS

Hana Hrubešová*(hrubehan@fjfi.cvut.cz)*

The primary goal of the Antihydrogen Experiment: Gravity, Interferometry, Spectroscopy (AEGIS) is the direct measurement of the Earth's gravitational acceleration g, on antihydrogen. The second physical goal is spectroscopic measurements of antihydrogen atoms in fly. The basic setup of the experiment should reach an accuracy of 1 % and higher precision through the radial cooling of the beam. The experiment them it self is located on the Antiproton Decelerator. It is 6th experiment in this area and it is using antiprotons made there.[1]

There are basic steps for production of a pulse of cold beam of $(\bar{H})$:

- Production of positonium (e^+) trough ^{22}Na source and accumulate them
- Capture and acumulation of antiprotons ($\bar{p}$) from the AD in a cylindrical Penning trap
- Cooling of the $\bar{p}$ to sub-K temperature
- Production of positronium (Ps) by bombarding cryogenic nanoprous material with pulse of e^+
- Excitation of the Ps to a Rydberg states which should have a principal quantum number $n = 25 - 35$
- Formation of $\bar{H}$ by resonant change exchange between Rydberg Ps and could $\bar{p}$
- Pulsed formation of an $\bar{H}$ beam by Stark acceleration with inhomogeneous electric field
- Determination of g in a two gratin Moire deflectometer coupled with a position-sensitive detector

For the manipulation with antihydrogen is very important one of his characteristic and that is Rydberg state. Rydberg atoms are atoms in which is at least one electron excited to a high quantum states. The principal quantum number n is typically about $n = 1 - 7$ for Rydberg atoms it may be as big as e.g. 300. Classical speaking of the large principal quantum number mean that the radius of the orbit of that electron around atoms is very huge and the time spend near core is short. The binding energy of the high excited states is very low. Their life time is very long and the dipole moments make them extremly sensitive to electrical filed. Their sensitivity to magnetic filed make it easy to control their behaviour through the application of external filed. The Rydberg atoms are named after Swedish physicist Johannes Robert Rydberg. He worked on a classification of atomic spectra line.Rydberg atoms are used for study of atom interaction.

There are three methods leading to production of Rydberg atoms. The first two methods are Electron impact excitation and Charge exchange excitation. The methods are based on the use of collimated beams of fast electrons incident on ground-state atoms or beam of ions and a population of neutral atoms of another species. The third method which is used in AEgIS experiment is Optical excitation. This method use tunable dye laser. The first laser is Uv, perfomer the transition from 1^3S to 3^3P the wavelength inrange $204 - 206nm$. The second laser which actually excitate to Rydberg states is IR laser. With the wavelength between $1680 - 1715nm$ excited the electrons up to Rydberg state.

The interested property of Rydberg atom is formation of Rydberg matter. Rydberg matter is matter consist of Rydberg atoms. It was predicted by E. A. Manykin, M. I. Ozhovan and P. P. Poluéktov around 1980. Rydberg matter consist of hexagonal planar clusters. The planar clusters are not very big because of retardation effect caused by the finite velocity of the speed of light. Planar clusters consist of specified number of atoms or, the numbers are so called magical numbers $N = 7, 10, 14, 19, 37, \ldots$. They can been imagine as dusty plasma with small clusters in a gas. Rydberg matter has a few interesting properties. One of them is metastability with long life time up to several hours for lower n. Another interesting properties is 'darkness' i.e. weak interaction with light. The stability of Rydberg matter is caused by delocalisation on the high energy electrons form an overall lower energy states. [4]

In these days in on AEgIS make preparation for launch the experiment in autumn. Then is expected the first manipulation with antihydrogen and may be a data collection. For the future plans it is possible.

References

[1] CERN-SPSC-2016-007(https://cds.cern.ch/record/2121329/files/SPSC-SR-178.pdf)

[2] CERN-SPSC-2007-017 (http://cdsweb.cern.ch/search?of=hdp=reportnumber:CERN-SPSC-2007-017)

[3] Holmlid L.,1998b, Chem. Phys 237, 11

[4] Badiei S., Holmlid J., 2002, Mon. Not. R. Astrom. Soc. 333, 360

CP Violation in the $B_s \to J/\psi\phi$ decay on ATLAS

Tomáš Jakoubek *(tomas.jakoubek@cern.ch)*

The $B_s^0 \to J/\psi\phi$ decay channel is expected to be sensitive to new physics contributions in CP violation field of study. In this channel, CP violation occurs due to interference between direct decays and decays occurring through $B_s^0 - \overline{B_s^0}$ mixing. The frequency of this mixing is characterized by the mass difference ΔM_s between light (B_L) and heavy (B_H) mass eigenstates. Difference between decay widths can be described using a CP-violating phase ϕ_s

$$\Delta\Gamma_s = \Gamma_L^s - \Gamma_H^s = 2\ |\Gamma_{12}^s|\ \cos\phi_s, \tag{1}$$

where Γ_L^s and Γ_H^s are decay widths of B_L and B_H states respectively. ϕ_s is small in the concept of the Standard Model and can be related to CKM quark mixing matrix via the relation

$$\phi_s \simeq -2\ \arg\left(-\frac{V_{ts}V_{tb}^*}{V_{cs}V_{cb}^*}\right). \tag{2}$$

Predicted value is $\phi_s = -0.0368 \pm 0.0018$ rad. Many new physics models predict large ϕ_s values whilst satisfying all existing constraints, including the precisely measured value of ΔM_s.

Our analysis is based on 4.9 fb^{-1} of $\sqrt{s} = 7$ TeV data from proton-proton collisions collected with the ATLAS detector in the year 2011 (separate study [1], published in 2014), combined with 14.3 fb^{-1} of $\sqrt{s} = 8$ TeV data from the year 2012 into the complete RUN-1 results presented here [2].

To be selected, events must contain at least one reconstructed primary vertex, formed from at least four Inner Detector (ID) tracks, and at least one pair of oppositely charged muons reconstructed using information from the Muon Spectrometer (MS) and the ID. Pairs of oppositely charged muon tracks are refitted to a common vertex and the pair is accepted if $\chi^2/\mathrm{ndf} < 10$. In order to account for varying mass resolution in different parts of the detector, the $|\eta(\mu)|$ dependent J/ψ mass cuts are applied. Decays $\phi \to K^+K^-$ are reconstructed from all pairs of oppositely charged particles with $p_\mathrm{T} > 1$ GeV and $|\eta| < 2.5$ that are not identified as muons. Candidates for B_s are selected by fitting the four tracks to a common vertex with J/ψ mass constrain [3]. Candidate is accepted if the vertex fit has $\chi^2/\mathrm{ndf} < 3$ and $|m(K^+K^-) - m_\mathrm{PDG}(\phi)| < 11$ MeV. If there is more than one accepted B_s candidate in the event, the one with the lowest χ^2/ndf is selected.

For each B_s candidate the proper decay time t is calculated:

$$t = \frac{L_{xy}\ m(B_s)}{p_\mathrm{T}(B_s)},$$

where $p_{\mathrm{T}}(B_s)$ is the transverse momentum of the B_s meson and $m(B_s)$ is the mass of the B_s meson, taken from [3]. The transverse decay length L_{xy} is the displacement in the transverse plane of the B_s meson decay vertex with respect to the primary vertex, projected onto the direction of the B_s transverse momentum.

Flavour tagging is used to improve this CP violation measurement. Initial flavour of (neutral) B_s can be inferred using the other B-meson, typically produced in the event (so called "Opposite-Side Tagging" method). To study and calibrate these methods, events containing the decays of "self-calibrated" channel $B^{\pm} \to J/\psi K^{\pm}$ can be used (flavour of the B-meson at production is provided by the kaon charge).

Detector effect have been studied using Monte Carlo (MC) samples. So-called "acceptance maps" (relying on three angles and p_T) have been created and applied to the data. Also an observed time dependence of the muon trigger have been corrected by weighting function (derived using real data and MC).

Time-angular unbinned maximum likelihood fit have been then performed on B_s^0 candidates within a mass range of 5.15 GeV $< m(B_s^0) <$ 5.65 GeV to extract the parameters characterising the decay. The full fit contains 25 free parameters. Below the important physical parameters are summarized: mean B_s^0 lifetime, the decay width difference $\Delta\Gamma_s$, and the CP-violating week phase ϕ_s. All results (2011, 2012, and the full RUN-1 statistical combination) are consistent with the world average values. Mass and lifetime fit projections are shown in Figure 1. Comparison with other experiments is shown in Figure 2.

	8 TeV data			7 TeV data			Run1 combined		
Par	Value	Stat	Syst	Value	Stat	Syst	Value	Stat	Syst
ϕ_s [rad]	-0.123	0.089	0.041	0.12	0.25	0.05	-0.098	0.084	0.040
$\Delta\Gamma_s$ [ps^{-1}]	0.096	0.013	0.007	0.053	0.021	0.010	0.083	0.011	0.007
Γ_s [ps^{-1}]	0.678	0.004	0.004	0.677	0.007	0.004	0.677	0.003	0.003

Table 1: Current results using data from 8 TeV pp collisions, the previous measurement using 7 TeV data, and the values for the parameters of the two measurements, statistically combined.

References

[1] G. Aad *et al.* [ATLAS Collaboration], "Flavor tagged time-dependent angular analysis of the $B_s \to J/\psi\phi$ decay and extraction of $\Delta\Gamma$s and the weak phase ϕ_s in ATLAS," Phys. Rev. D **90** (2014) 5, 052007.

[2] G. Aad *et al.* [ATLAS Collaboration], "Measurement of the CP-violating phase ϕ_s and the B_s^0 meson decay width difference with $B_s^0 \to J/\psi\phi$ decays in ATLAS," arXiv:1601.03297 [hep-ex].

[3] K. A. Olive *et al.* [Particle Data Group Collaboration], "Review of Particle Physics," Chin. Phys. C **38** (2014) 090001.

[4] Y. Amhis *et al.* [Heavy Flavour Averaging Group], "Averages of b-hadron, c-hadron, and τ-lepton properties as of summer 2014,", arXiv:1412.7515 [hep-ex] and online update at `http://www.slac.stanford.edu/xorg/hfag/osc/summer_2015`

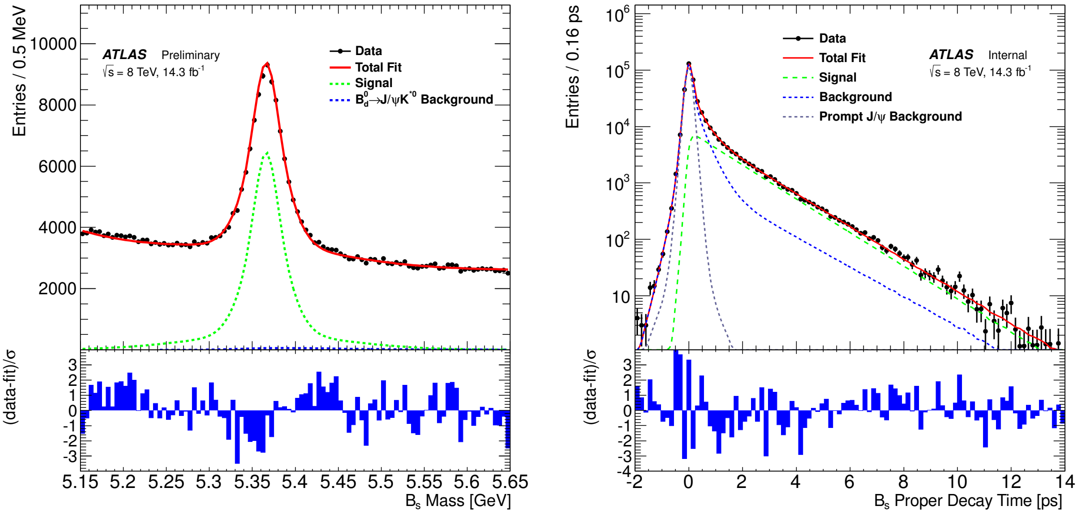

Figure 1: (Left) Mass fit projection for the 2012 data. The red line shows the total fit, the dashed green line shows the signal component while the long-dashed blue line shows the contribution from $B_d^0 \to J/\psi K^{0*}$ events. (Right) Proper decay time fit projection for 2012 data. The red line shows the total fit while the green dashed line shows the total signal. The total background is shown as a blue dashed line with a long-dashed grey line showing the prompt J/ψ background.

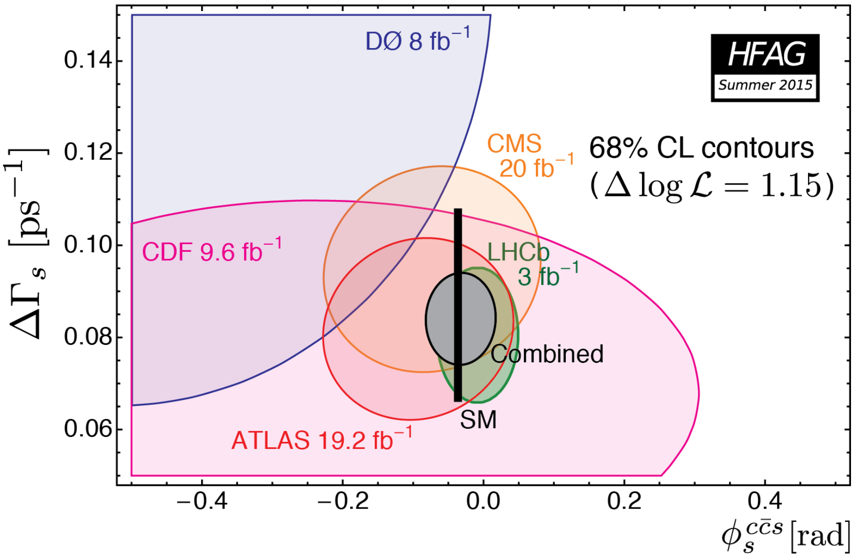

Figure 2: Plot of the 68% confidence-level contours in the $\phi_s - \Delta\Gamma_s$ plane with the individual contours of ATLAS, CMS, CDF, D∅, and LHCb experiments, their combined contour (solid line and shaded area), as well as the Standard Model predictions (thin black rectangle). [4]

Measuring the light yield of scintillators

Michal Kocan*(kocanmi3@fjfi.cvut.cz)*

In my bachelor paper I have studied the design of the future forward electromagnetic calorimeter FoCal. On our faculty is developing as a scintillation version. I was also doing simulations in GEANT 4. From simulations I can get a dependence of the deposit energy on the thickness of the active layer. Also I can get Molière radius, which is important in a reconstruction of particles. From the deposit energy in active layers I was able to determine the energy resolution of the detector. In next step of developing the scintillation calorimeter we will study light yield of scintillators.

The light yield of scintillators is one of the most important characteristics. Light yield depends not only on the material, but also on the temperature and on the value of the deposit energy in the scintillators. The absolute light yield of scintillators is defined as the ratio of total energy of scintillation photons to energy deposited by ionizing radiation in the scintillator and is characterized by the number of photons in scintillation per 1 MeV energy radiation absorbed by scintillator. [1]

For measurements are using four different methods. It is the pulse method, the method based on the measuring of the intrinsic resolution of the PMT, the single-electron method and the method of comparison. The pulse method is based on the measuring of the signal amplitude at the output of the spectrometer's output. The light yield of scintillator is associated with the signal amplitude. In second method the light yield is determined by measuring the number of photoelectrons on the first dynode of the PMT. In the single electron method is compared the signal amplitude from the detector with the value of the amplitude of the single electron distribution. In the method of comparison is compared the signal amplitude of the sample, with the well known scintillation light yield, and the signal amplitude of the new sample. In our measurements we are going to use the single electron method or the method of comparison.

For the right absolute scintillation yield determination with PMT, we need to know: 1) the light collection efficiency of scintillation photons on the PMT, 2) the effective quantum efficiency of that PMT, 3) the absolute number of photoelectrons emitted by the photocathode in a scintillation event of known gamma ray energy, and 4) the photoelectron collection efficiency on the first dynode. [3] To collect all scintillation photons the scintillator is covered with reflector. As reflector could be used Teflon which has almost 100% reflectivity. For better collecting photons on the photocathode we can use optical coupling. This fortunately undefinably change the quantum efficiency because the quantum efficiency is measured by manufacture with direct photons. [2, 3] Thus the optical coupling is not good for precise measuring. Every photon can incident with photocathode, reflect or transmit. So if we cover scintillator with good reflector the reflected photon on photocathode can again try to incident, and so on. This is going to change the quantum efficiency measured by manufacture to new effective quantum efficiency. The total number of photoelectrons emitted by photocathode in a scintillation event is determined by the single electron method. The photoelectron collection efficiency on the first dynode is for photomultipliers with box-and-grid type dynode structure almost 100% efficiency. [3]

In our measurements we are going to try measure well know scintillators as a test of our measuring device. Next we are going to measure new type of scintillators which are developing on our faculty. We will also try to measure the dependence of the absolute light yield on the energy of the gamma radiation.

References

[1] E. Sysoeva, V. Tarasov, O. Zelenskaya, "Comparison of methods for determination of scintillation light yield," Nucl. Instrum. Methods, vol. A486, pp. 67-73, 2002

[2] J. T. M. de Haas, P. Dorenbos, and C. W. E. van Eijk, "Measuring the absolute light yield of scintillators," Nucl. Instrum. Methods, vol. A537, pp. 97-100, 2005

[3] J. T. M. de Haas and P. Dorenbos, "Advances in Yield Calibration of Scintillators," IEEE Transactions on Nuclear Science, vol. 55, no. 3, pp. 1086-1092, 2008

Study of jet production in Au+Au collisions in the STAR experiment

Martin Kocmánek*(kocmama2@fjfi.cvut.cz)*

1 Introduction

Several particle physics experiments are focused on the research of nuclear matter under extreme conditions. The STAR experiment is dedicated to study nuclear matter at extremely high temperature and pressure. It is located at RHIC at Brookhaven National Laboratory, where heavy ions are accelerated to ultra-relativistic velocities and collided in order to create a state of hot and dense nuclear matter, consisting of deconfined partons (quarks and gluons), referred to as a quark-gluon plasma (QGP). QGP is theoretically predicted by Quantum Chromodynamics. During early hard scattering, partons of incoming nuclei undergo fragmentation and hadronization which results in jets, collimated sprays of hadrons. Jets are one of the most important probes of the QGP. Due to interaction of hard partons with surrounding QGP, the energy of partons is reduced in comparison to elementary proton-proton collisions which is referred to as a jet quenching. Measurement of modifications of jets transversing the nuclear matter provides important information of properties of hot and dense nuclear matter.

2 Jet reconstruction

Jets are reconstructed from particles which energy and momentum are measured in detectors. Jet-finding algorithms are used for jet reconstruction and their main goal is to cluster a set of charged tracks and neutral towers into jets. The algorithm selects a set of particles, which are typically emitted close to each other in angle, and combines their momenta to form the total momentum of a jet. The selection process is called the jet algorithm and the momentum addition rule is called the recombination scheme. Jet resembles kinematic properties of the original parton, therefore allows to access early stages of the collision. Jet reconstruction is successful in p+p collisions and serves as a fundamental test of QCD and as a reference to A+A collisions. A heavy-ion collision is a high-multiplicity environment with a large and inhomogeneous background, therefore the full jet reconstruction is challenging in such collisions.

An ideal jet algorithm has to fulfil several attributes[1]. It should be fully specified: the jet selection process and the jet kinematic variables are clearly defined. Further requirements are detector and order independence which means algorithm behaves equally at the parton, particle and detector level. The ideal algorithm is also collinear and infrared safe - adding of an infrared or collinear particle into an event will not influence existence or shape of measured jets. Finally, due to the enormous number of analysed data, jet algorithm should be stable and provide jet identification with a minimum of computer time.

Jet algorithms can be divided into two groups: cone and recombination. According to the selection of a starting particle, cone jet algorithms can be divided into seedless and seeded algorithms that start from the most energetic particle. A cone algorithm draws a virtual cone around the highest p_T particle and everything inside the cone is defined as a jet. The most important cone algorithms are the Cone, which is a seeded algorithm and infrared unsafe, and SISCone, which is in contrast to Cone seedless, infrared and collinear safe. The next category of algorithms are recombination algorithms. They are based on selecting a starting particle and then sequentially add other particles that are close enough to the arising jet. The most commonly used clustering algorithms are the k_T and the anti-k_T (Figure 1). All are infrared safe and differ from each other in calculation of the distance between particles. The k_T algorithm recombines first particles with low p_T close to each other in space. The anti-k_T algorithm clusters first particles with the highest p_T. Therefore the anti-k_T algorithm is resilient to the soft background. For the jet reconstruction the FastJet[2] software package is commonly used, which contains jet algorithms and tools for jet analysis.

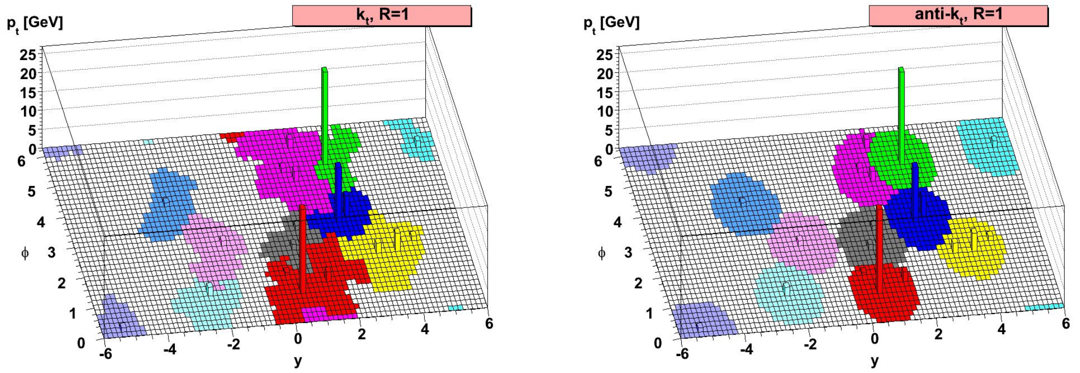

Figure 1: Comparison of the same event reconstructed by the k_T (left) and the anti-k_T (right) algorithm[3]. The parameter R determines the radius of a jet.

3 Results of jet analysis at STAR

One of the first attempts to perform full jet reconstruction in the environment of heavy-ion collisions was in the analysis of Au+Au collisions at $\sqrt{s_{NN}}$= 200 GeV from the Run 7 at RHIC. Figure 2 shows the jet R_{AA} which is the ratio of the jet production in Au+Au and jet production in p+p collisions scaled by binary collisions. Measured jet R_{AA} for $R = 0.2$ jets is more suppressed than R_{AA} for $R = 0.4$ which is compatible with the unity, within large systematic uncertainties. This fact indicates jet broadening in heavy-ion collisions. There is a difference between algorithms due to their different response to the heavy-ion background. This result is inconclusive and for its improvement higher statistics is necessary to suppress the uncertainties.

The STAR Run 11 provides higher statistics, therefore results are more promising. Figure 3 presents the first quantitative comparison of jet quenching at RHIC and the LHC.

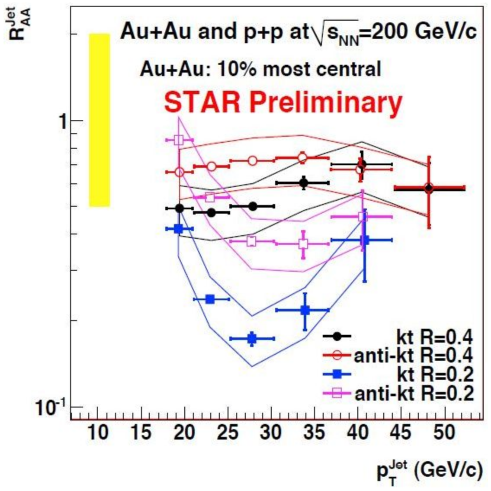

Figure 2: Jet R_{AA} in Au+Au collisions at $\sqrt{s_{NN}}$= 200 GeV[4].

It shows charged recoil jet spectrum for central and peripheral collisions and compares the jet nuclear modification factor for central and peripheral Au+Au collisions at $\sqrt{s_{NN}} = 200$ GeV for $R = 0.3$ with the result from ALICE in Pb+Pb collisions at $\sqrt{s_{NN}} = 2.76$ TeV for $R = 0.4$. The lower panel on the left side shows I_{CP} which is the ratio of central to peripheral distributions. At low p_T the I_{CP} is close to 1. For $p_{T,jet} > 10$ GeV/c, significant jet yield suppression $I_{CP} = 0.2$ can be observed in central collisions.

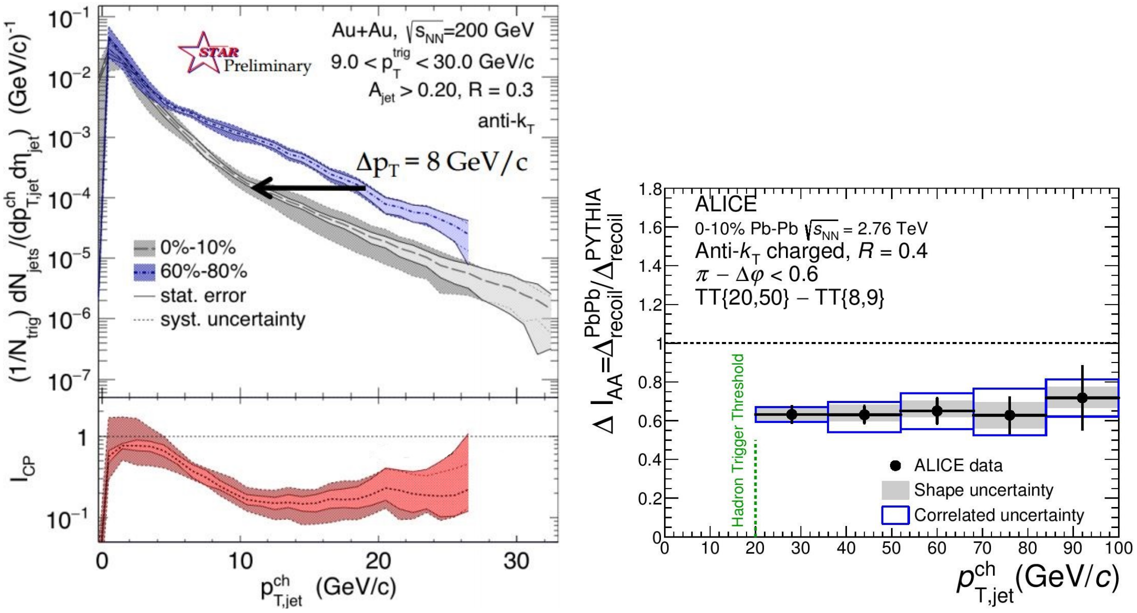

Figure 3: Left: Charged recoil jet spectrum for central and peripheral collisions $R = 0.3$ together with the nuclear modification I_{CP} [5]. Right: ΔI_{AA}, the ratio of Δ_{recoil} in Pb+Pb and PYTHIA p+p collisions at $\sqrt{s} = 2.76$ TeV for $R = 0.4$ [6].

4 Research project

The main aim of my research project is to study properties of fully reconstructed jets produced in Au+Au collisions at $\sqrt{s_{NN}}$= 200 GeV from Run 11. Charged tracks were measured by the Time Projection Chamber (TPC) and neutral towers by the Barrel ElectroMagnetic Calorimeter (BEMC) of the STAR experiment. Firstly, the study of data quality assurance, response of the BEMC and its time stability will be performed. In this part it is necessary to exclude runs with non-functional BEMC sectors and hot towers which are towers with excessive energy deposit or hit rate higher than the mean value of all towers. The main part of the research project is the application of the sequential recombination algorithm anti-k_T in Au+Au collisions as a function of the centrality and the resolution parameter R to create uncorrected jet spectra. Then the subtraction of background and the study of its influence on jet spectra will follow. To estimate background, the k_T algorithm will be applied on data. The background density ρ for each event is a median of p_T of all reconstructed k_T jets in the event. Uncorrected jet energy for each jet candidate will be subtracted by the estimated background energy in the jet area: $p_{T,jet}^{corr} = p_{T,jet}^{uncorr} - \rho \cdot A_{jet}$, where A_{jet} is the jet area. In the last part, the influence of detector effects on jet spectra will be studied.

References

[1] G. C. Blazey et al., Run II jet physics, hep-ex/0005012

[2] M. Cacciari, G. P. Salam and G. Soyez, FastJet user manual, Eur. Phys. J. C **72** (2012) 1896 [arXiv:1111.6097 [hep-ph]].

[3] M. Cacciari, G. P. Salam and G. Soyez, The Anti-k(t) jet clustering algorithm, JHEP **0804** (2008) 063 [arXiv:0802.1189 [hep-ph]].

[4] M. Ploskon [STAR Collaboration], Inclusive cross section and correlations of fully reconstructed jets in $\sqrt{s_{NN}}$ = 200 GeV Au+Au and p+p collisions, Nucl. Phys. A **830** (2009) 255C [arXiv:0908.1799 [nucl-ex]].

[5] P. M. Jacobs *et al.* [STAR Collaboration], Measurements of jet quenching with semi-inclusive charged jet distributions in $Au + Au$ collisions at $\sqrt{s_{NN}}$=200 GeV, arXiv:1512.08784 [nucl-ex].

[6] J. Adam *et al.* [ALICE Collaboration], Measurement of jet quenching with semi-inclusive hadron-jet distributions in central Pb-Pb collisions at $\sqrt{\mathbf{s_{NN}}}$ = 2.76 TeV, arXiv:1506.03984 [nucl-ex].

Event shape analysis in ultrarelativistic nuclear collisions

Renata Kopečná *(kopecren@fjfi.cvut.cz)*

---

1 Introduction

We present a novel method of analyzing events of multiparticle production. Heavy ion collisions are collisions of two complicated systems. The initial conditions fluctuate from event to event. There are different impact parameters, fluctuating parton distributions and energy depositions even within one centrality class. The analysis of event shapes can help us identify events undergoing similar evolution. We present a novel study of event shape using the algorithm proposed in [1]. This algorithm studies the *shape* of the distribution rather than one variable. This algorithm compares, sorts and selects events according to *similarity* with each other. The method studies the angular distribution via the algorithm using the Bayesian concept of probability. Moreover, it allows us to determine a good measure of the event shape.

2 The Method

The method is thoroughly described in [5]. Here, it will be described only briefly with the help of an example. First, we generated 5000 events using a toy model. This model generates azimuthal angles of pions from the distribution

$$P_5(\phi) = \frac{1}{2\pi}\left(1 + \sum_{n=1}^{5} 2v_n \cos(n(\phi - \psi_n))\right) . \tag{1}$$

The parameters v_n are multiplicity dependent as

$$v_n = a_n M^2 + b_n M + c_n \, , \tag{2}$$

where a_n, b_n, and c_n are parameters taken from experimental data [3, 4], $M \in (300, 3000)$. Those parameters for each n can be found in Table 1.

For each event, we made an azimuthal angle histogram with 20 bins. Every event is then described by its record $\{n_i\}$. Since we are studying the angle distribution, the choice of rotating single events is free. We will address this issue in the next section. The algorithm operates as follows:

1. (Somehow rotate the events.)
2. Order events according to a chosen variable.

Table 1: Parameters used for generating multiplicity dependent v_n.

n	$a/10^{-8}$	$b/10^{-5}$	c
1	0	0.01667	–0.000680
2	–7.098	20.06	0.07874
3	–2.083	6.658	0.0424
4	–96.38	2.621	0.04897
5	–71.76	2.236	0.01673

3. Divide sorted events into quantiles (deciles). The event bins are denoted using Greek letters (μ).
4. For every event calculate the probability that event with record $\{n_i\}$ belongs to event bin μ: $P(\mu|\{n_i\})$.
5. For every event calculate mean bin number $\bar{\mu}$ (values 1 - 10):
   $\bar{\mu} = \sum \mu P(\mu|\{n_i\})$.
6. Sort events according to $\bar{\mu}$.
7. If the new sorting changed the assignment of any events into event bins, return to (3). Otherwise the algorithm converged.

Events with a similar shape are organized by the algorithm in a way that they end up close together. There is no specific observable according to which the sorting proceeds. Moreover, the final arrangement of events is independent of the initial sorting as well as multiplicity. The final arrangement is expressed by the mean bin number $\bar{\mu}$.

3 Results

3.1 Elliptic flow

First, we tested the algorithm using events including only v_1 and v_2, higher harmonics were taken as zero (see eq. 1). One of the methods used in event shape studies is *Event shape engineering* [2], which sorts the events according to $q_2 = 1/M|\sum_{j=1}^{M} e^{2i\phi_j}|$. We were interested in verifying whether q_2 is truly a good variable for sorting events. As can be seen in fig. 1, the correlation of $\bar{\mu}$ with v_2 is clearly better than correlation of $\bar{\mu}$ with q_2. This means v_2 is better observable for sorting events than q_2 in this simple case. As mentioned before, the rotation of each event can be arbitrary. Since in this simple case v_2 is clearly dominant, we decided to rotate events in a way that $\Psi_2 = 0$. The final event sorting is in fig. 2. It is obvious that the elliptic flow decreases with the event bin number.

3.2 Anisotropic flow

The initial event rotation in the case of including harmonics up to pentagonal flow is not as simple as in the previous case. Interplay of harmonics comes into play. Since v_2 and v_3 are clearly dominant, we rotated events according to the angle bisector between

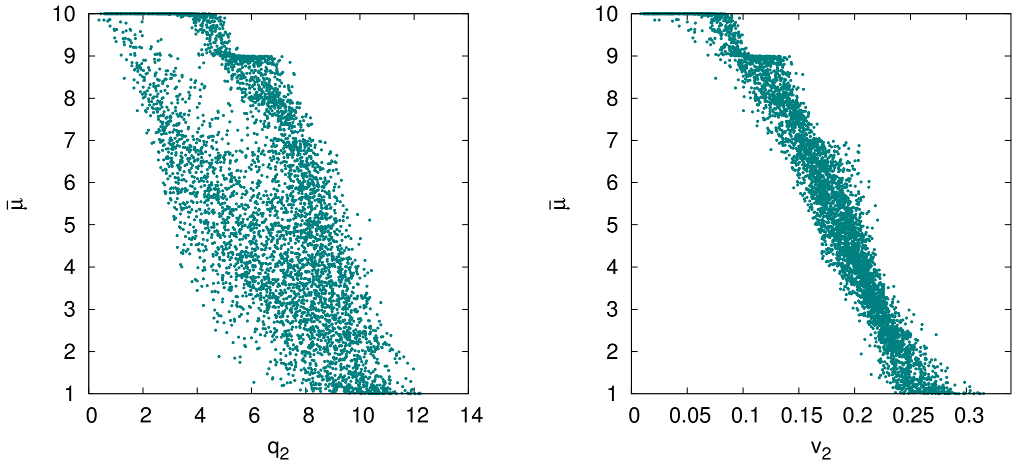

Figure 1: Left: correlation of $\bar{\mu}$ with q_2 determined for each event. Right: correlation of $\bar{\mu}$ with v_2 determined for each event via the event plane method.

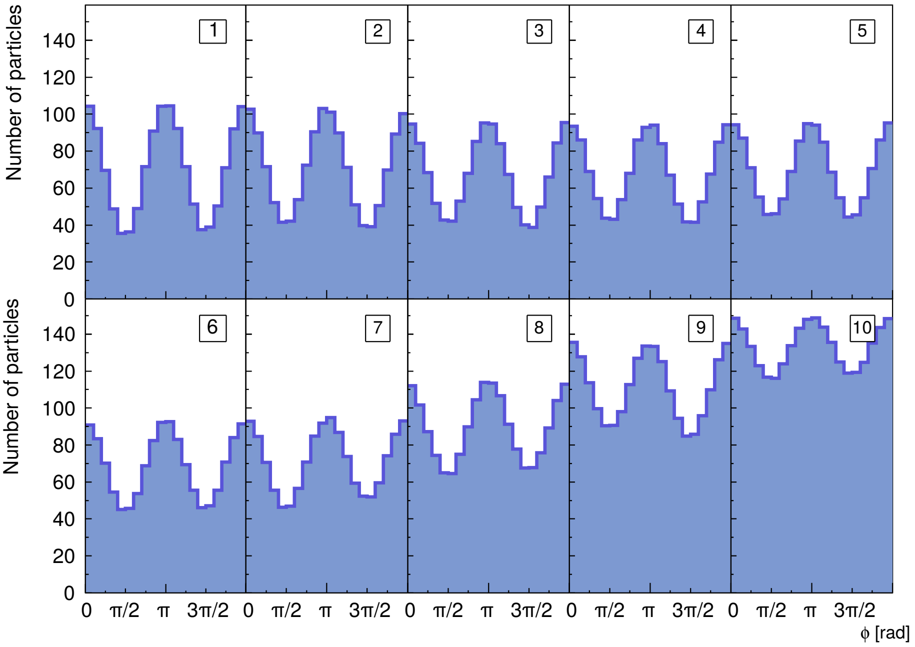

Figure 2: Average histograms of the azimuthal angles for event bins 1–10, with event bins indicated in the panels. Events with only v_2 and v_1.

ψ_2 and ψ_3, which we denote as ψ_{2-3}. In order to take care of the parity symmetry, the events were oriented so that ψ_2 is less than $\pi/2$ away from ψ_3 *counterclockwise*. As can be seen in fig. 3, v_2 is as bad for sorting events as q_2 and the sorting is not even dominated by v_3. Higher harmonics do not play any role at all. This suggests that event shape is determined by an interplay of several observables.

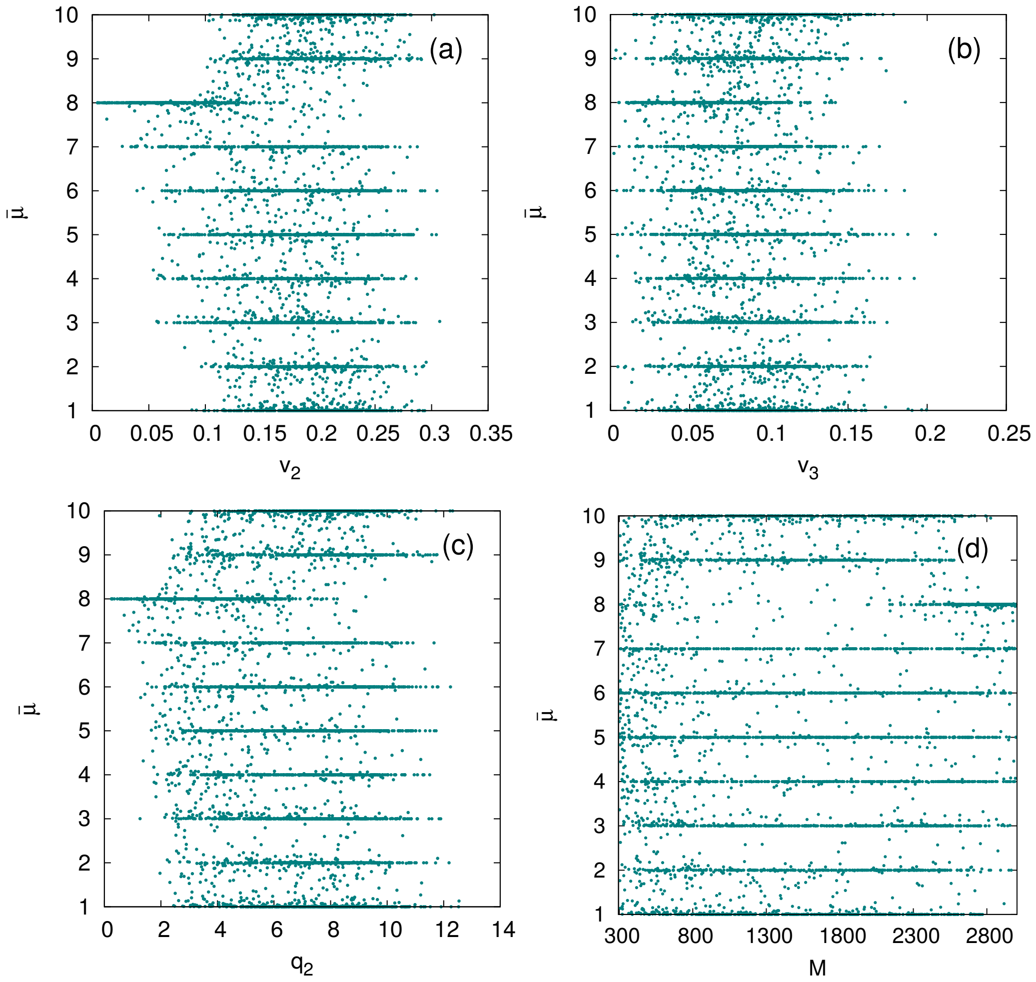

Figure 3: Correlation of various observables with final sorting variable $\bar{\mu}$. Simulated are events with anisotropies up to 5th order and initial rotation is according to ψ_{2-3}. Correlation with a) v_2, b) v_3, c) q_2, d) event multiplicity.

3.3 AMPT

We simulated 2000 events using the AMPT model [6]. The events corresponded to 0-20% centrality class produced in Pb+Pb collisions at $\sqrt{s_{NN}} = 2.76\,\text{TeV}$. The parton screening mass was set to 2.097 fm^{-1}. In order to avoid underestimation of partonic effects, string melting is turned on [6].

In those events rapidity cut $|y| < 1$ was made in order to roughly simulate detector acceptance. We have analyzed the distribution of all charged particles.

The results of applying the algorithm on events rotated according to ψ_{2-3} can be seen in fig. 4. It is clear that v_2 is dominant. The correlation is stronger in the case of using p_T

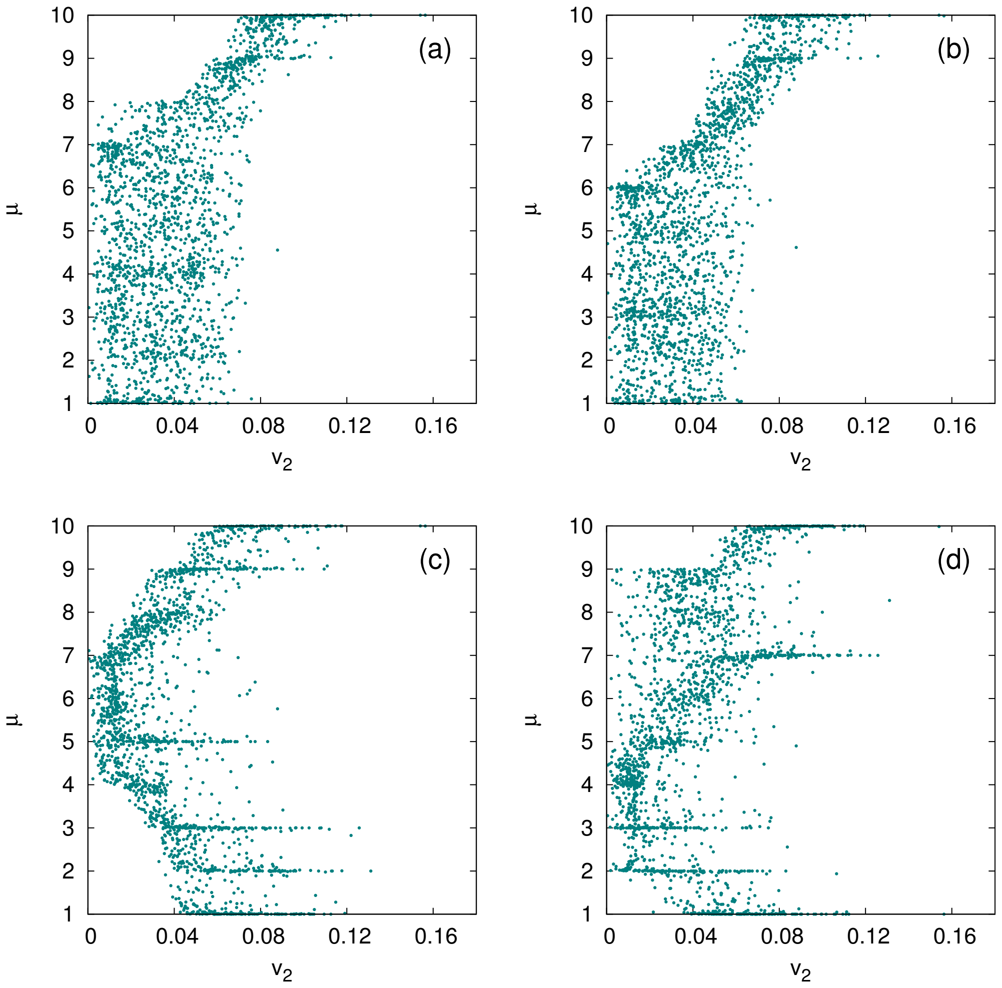

Figure 4: Correlation of the final sorting variable $\bar{\mu}$ with v_2 of individual events for events generated by AMPT. a) Initial alignment of the events according to ψ_2, b) initial alignment according to ψ_2 and v_2 evaluated with p_T weight, c) initial alignment according to ψ_3, d) initial alignment according to ψ_{2-3}.

as a weight in evaluating v_2. In order to better understand the differences between event bins we present the average histograms for each even bin after the sorting procedure is completed in fig. 5. The gradual growth of v_2 in event bins 8, 9, and 10 is evident. The other event bins evince a more complicated structure, higher order anisotropies play an important role as well. However, no clear correlation of any higher v_n with $\bar{\mu}$ is observed.

3.4 Conclusions and Outlook

This new approach can be useful in studies including mixed events technique. Using this algorithm, one could do e.g. a femtoscopic study of an exclusive group of events. Moreover, this approach can be applied when studying U+U collisions. The asymmetric shape of U nucleus results in large fluctuations of anisotropies of the transverse flow. Our algorithm could distinguish non-central tip-tip collisions from side-side or body-body collisions.

There are several issues we are going to investigate. First, the required computational

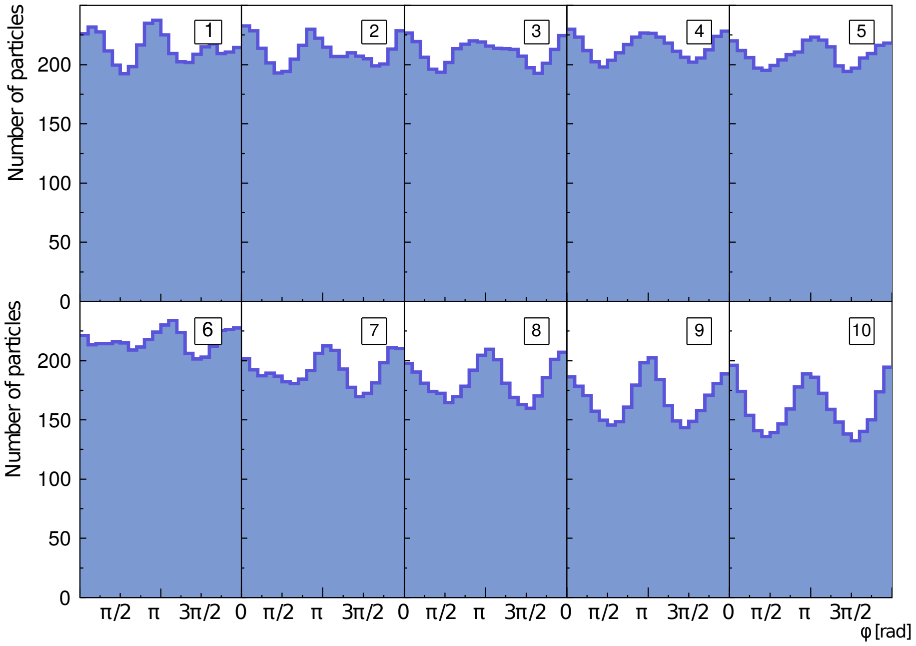

Figure 5: Average histograms of the azimuthal angles for event bins 1–10, from events generated with AMPT. Initial alignment of events according to ψ_2.

time is rather high. However, we have not optimized our algorithm yet, so we expect the required CPU time to decrease significantly. Second problem is the initial rotation of events. So far, we have not determined the ideal initial rotation.

Moreover, we are studying a set of less central events obtained by AMPT. This might help us better understand the event shape. Despite the difficulties mentioned here, we believe that the method we presented is worth applying in real data and that it will bring more detailed insight into heavy-ion collision dynamics.

References

[1] S. Lehmann, A.D.Jackson, B. Lautrup: Measures and Mismeasures of Scientific Quality, Arxiv: physics/0512238

[2] J. Schukraft, A. Timmins, S. Voloshin, Phys. Lett. B **719**(2013) 394

[3] G. Aad *et al.* [ATLAS Collaboration], Phys. Rev. C **86** 014907 (2012) [arXiv:1203.3087 [hep-ex]].

[4] G. Eyyubova [for the ALICE Collaboration], EPJ Web of Conferences **70** 00075 (2014).

[5] R. Kopečná and B. Tomášik, arXiv:1506.06776 [nucl-th].

[6] Z.-W. Lin *et al.*, Phys. Rev. C **72** 064901 (2005)

Performance of the ALICE secondary vertex b-tagging algorithm

Lukáš Kramárik *(kramaluk@fjfi.cvut.cz)*

1 Introduction

Jet reconstruction provides access to the kinematics of partons produced in hard scatterings in the initial stage of heavy-ion collisions and that later suffer energy loss in the medium via gluon radiation and elastic collisions. The parton energy loss in the quark-gluon plasma (QGP) depends on the colour charge and mass of the parton. For heavy quarks it is expected that radiative energy loss is suppressed due to coherence effects [1, 2]. This should lead to a smaller modification of the transverse momentum spectra for particles containing heavy quarks than for inclusive charged hadrons. On the other hand, for heavy quarks in the QGP, collisional energy loss may be important at low transverse momentum p_{T}. The jet quenching phenomenon and the properties of produced matter can be further understood by measuring beauty jets at low jet transverse momentum in comparison with light-flavour jets [3].

The ALICE detector [4] is capable to discriminate jets originating from b quarks with different tagging algorithms. Here we study the performance of the b-jet tagging algorithm based on displaced secondary-vertex topologies for p-Pb collisions at $\sqrt{s_{\mathrm{NN}}} = 5.02$ TeV. The p-Pb collisions serve as a test for cold nuclear effects which are important in measurements of jet quenching in Pb-Pb collisions.

2 Analysis details

In this analysis we use MC with simulated responses of ALICE detector by GEANT3 [5] for p-Pb collisions at $\sqrt{s_{\mathrm{NN}}} = 5.02$ TeV. A MC simulation for pp collisions at $\sqrt{s} = 5.02$ TeV with a Lorentz boost to get the same rapidity shift as in p-Pb collisions is used to study detector response for jets without underlying event. PYTHIA6, with tune Perugia 2011 [6], is employed for MC pp simulations. The MC for p-Pb collisions is represented by a cocktail of event generators PYTHIA6 (Perugia 2011) + HIJING [7] which correspond to hard physics and p-Pb background respectively.

The efficiency of b-tagging is defined as the number of b jets in sample after applying cuts (tagged sample), divided by "true" number of b jets in MC data sample with no cuts applied. In addition, the purity is fraction of b jets in the tagged sample. These variables could be accessed in the MC simulations. In order to estimate the efficiency and the purity, we use input ("true") b jets in MC, which can be identified by different labelling methods. High purity allows to suppress the contamination of light-flavour and charm jets, which is important since the measured fraction of b jets to inclusive jets is at the level of 2-4% (as measured by CMS experiment), both in pp collisions at $\sqrt{s} = 7$ TeV [8] and in p-Pb collisions at $\sqrt{s_{\rm NN}} = 5.02$ TeV [9].

2.1 Jet reconstruction and background estimation

For the estimation of the background density and fluctuations in jet reconstruction, we use a similar approach as it was applied by ALICE for charged jet measurements in p-Pb collisions [10]. Namely, the anti-$k_{\rm T}$ algorithm from the FastJet package [11] with resolution parameter of $R = 0.4$ is used to reconstruct charged jets. We use the CMS method [12], which is suited for more sparse environment in p-Pb collisions w.r.t Pb-Pb collisions, for the calculation of the background density. Only jets with jet axis in the pseudorapidity interval $|\eta_{\rm jet}| < 0.5$ are considered. In this study the background fluctuations are measured with HIJING p-Pb events with particle transport through the ALICE detector. The background fluctuations under the jet area are found to be slightly smaller in the HIJING simulation than in the p-Pb data [10].

2.2 Correction for detector effects and background fluctuations

The jet momentum distribution is distorted by the detector mainly due to tracking inefficiency and momentum resolution. In order to correct for detector effects the detector simulation with GEANT is performed. Reconstructed jets at particle level without detector effects and jets at the detector level after particle transport through the ALICE detector are matched and based on it the detector response matrix is built. From the inverse response matrix and the momentum distribution at detector level one finds the true jet momentum distribution. The Singular Value Decomposition (SVD) approach [13] is used in this performance study.

After subtracting the constant background in each event in order to correct the jet $p_{\rm T}$, one has to keep in mind that the background is not necessary constant, but may differ for different jets in a given event. This is corrected statistically (not event by event) via an unfolding technique with a background fluctuation matrix. The actual unfolding is done with a matrix which is a product of two matrices: detector response matrix and background fluctuation matrix.

2.3 Secondary vertex tagging algorithm

Due to the long life-time of B hadrons, in most cases their decay vertex is displaced from the primary vertex of a collision. This algorithm reconstructs secondary vertices (SV) in a jet and uses their properties to discriminate b jets among lighter flavour jets. The tracks participating in SV reconstruction are tracks belonging to a jet with additional requirements: the point in the Silicon Pixel Detector and $p_{\rm T,track} > 1$ GeV/c. All combinations of three tracks, satisfying the requirement, are used to build secondary vertices in a jet. The quality of vertex reconstruction is characterized by the dispersion of the tracks in the vertex $\sigma_{\rm vtx} = \sqrt{d_1^2 + d_2^2 + d_3^2}$, where $d_{1,2,3}$ are the distances of the three tracks from SV. The sign of the SV flight distance is defined w.r.t. the jet direction, so that the signed length is $L = |\vec{L'}|\mathrm{sign}(\vec{L'} \cdot p_{jet})$, where $\vec{L'}$ is the SV position. The cuts on the the most displaced SV found in the jet, namely SV dispersion, σ_{vtx}, and the significance of flight distance in a transverse plane, $L_{xy}/\sigma_{L_{xy}}$, are used for b-jet tagging in this analysis.

2.4 MC labelling

To assign the "true" flavour of reconstructed jets in the MC simulations, the MC event history is used. Here we treat a jet as coming from a beauty quark, if a B hadron was found in a cone $\Delta R < 0.7$ around jet axis. If no beauty hadron is present, but charm hadron was found in a cone $\Delta R < 0.7$, the jet is labelled as c-jet. All other jets are considered as light-flavour jets.

3 Performance of SV b-tagging algorithm

The discrimination power of the signed flight distance significance can be judged by the distribution of this variable for jets of different flavours, which is shown in Fig. 1. Secondary vertices are searched in jets with $p_{\mathrm{T,jet}} > 20$ GeV$/c$ and the most displaced vertex in a jet is considered. The larger the cut value of $L_{xy}/\sigma_{L_{xy}}$, the more light and charm jets are rejected compared to beauty jets. As mentioned above, the tagging procedure uses cuts on $L_{xy}/\sigma_{L_{xy}}$ and σ_{vtx} of SV. Different values of cuts yield different algorithm performance. For a particular algorithm an operating point is defined based on inclusive b-tagging efficiency and mistagging rate.

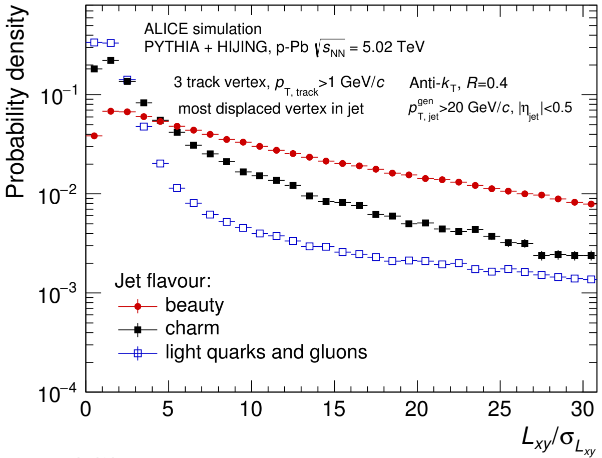

ALI-SIMUL-95610

Figure 1: Probability distribution of the signed flight distance significance of the most displaced secondary vertex, found in charged jets with $p_{\mathrm{T}} > 20$ GeV in p-Pb simulations at $\sqrt{s_{\mathrm{NN}}} = 5.02$ TeV. The different jet flavours are assigned as described in Sec. 2.4.

Figure 2, left, shows the mistagging rate vs the b-tagging efficiency in jet p_{T} range $30 < p_{\mathrm{T,jet}} < 40$ GeV$/c$ for different operating points, which are obtained by varying the cuts on $L_{xy}/\sigma_{L_{xy}}$ (from 2 to 14), while the cut $\sigma_{\mathrm{vtx}} < 0.02$ cm is kept fixed. The performance may depend on $p_{\mathrm{T,jet}}$. In the considered region, $30 < p_{\mathrm{T,jet}} < 40$ GeV$/c$, the mistagging and tagging efficiencies are almost flat. Looser cuts result in larger statistics and higher tagging efficiency, but also higher mistagging rate, and therefore reduce purity

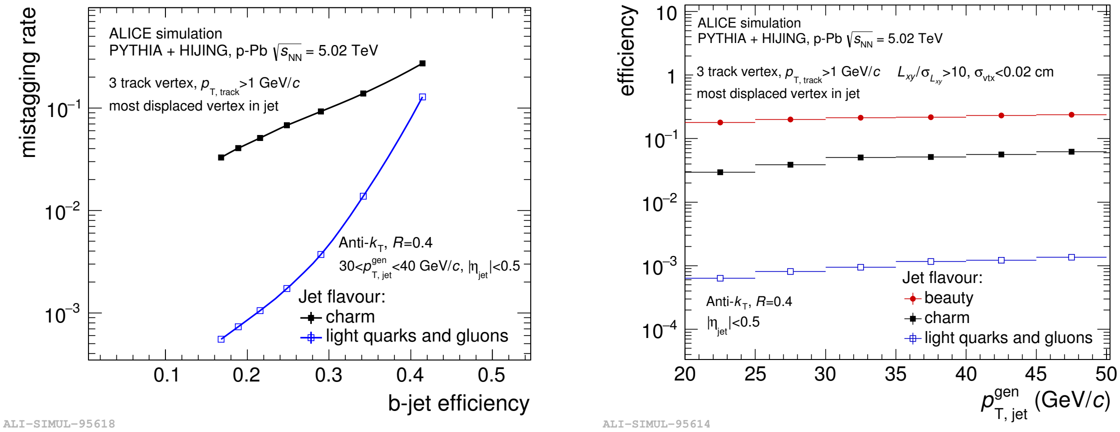

ALI-SIMUL-95618 ALI-SIMUL-95614

Figure 2: Left: Mistagging rate vs the b-tagging efficiency of SV tagging algorithm for different operating points for p_T range $30 < p_{T,jet} < 40$ GeV/c. Right: The $p^{gen}_{T,jet}$ dependence of the b-tagging efficiency and mistagging rate for $L_{xy}/\sigma_{L_{xy}} > 10$ and $\sigma_{vtx} < 0.02$ cm.

of sample. The operation point is chosen in a way that the mistagging efficiency for light-flavour jets would be about two orders of magnitude lower than the tagging efficiency. This comes from the CMS measurements on the ratio of b jets to inclusive jets, in which the b-jet fraction was found to be at the level of 2-4% in pp collisions at $\sqrt{s} = 7$ TeV [8]. The tagging and mistagging efficiencies $\epsilon(p^{gen}_{T,jet})$ at particle level for the chosen operating point with $L_{xy}/\sigma_{L_{xy}} > 10$ and $\sigma_{vtx} < 0.02$ cm are reported in Fig. 2, right. The b-tagging efficiency is at the level 0.2. The efficiency to tag light-flavour jets is two orders of magnitude lower and the efficiency to tag charm jet is about 3 to 5 times lower than the b-tagging efficiency.

The correction for detector effects is tested with two detector response matrices: the detector response for b-jets and the one for inclusive jets. Figure 3 shows the ratio of two unfolded b-jets p_T-spectra. In both cases the unfolding procedure yields similar result. This ensures that beauty and inclusive jets have similar detector response matrices and therefore the detectors response for inclusive jets can be used to unfold the tagged b-jet spectrum.

The different sequences of corrections are further studied in order to estimate the impact of background fluctuations on the stability of results. We perform the two scenarios of corrections:

1. the measured tagged b-jet spectrum is first unfolded for detector response and background fluctuations, then corrected for the b-tagging efficiency as a function of p^{gen}_T (at particle level).

2. the measured tagged b-jet spectrum is first corrected for the b-tagging efficiency as a function of p^{det}_T and then unfolded for detector response and background fluctuations.

The comparison of these two scenarios is shown on Fig. 4 as the ratio between the two corrected spectra. The two spectra are in agreement with each other, suggesting that both scenarios can be applied in p-Pb collisions.

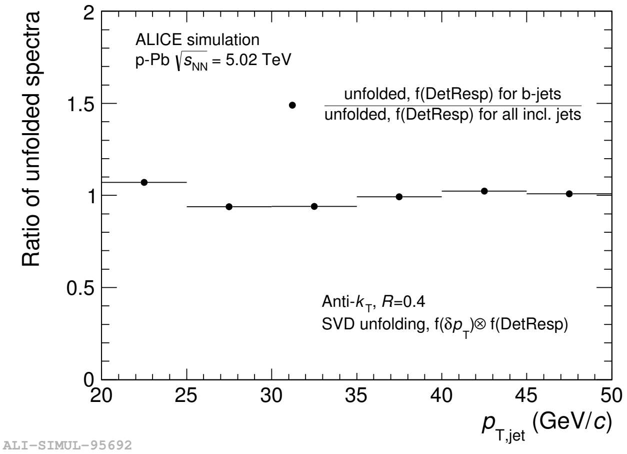

Figure 3: Comparison of SVD unfolding of b-jet spectrum with two matrices: detector matrix for inclusive jets and for b jets. Both matrices are combined with background fluctuation matrix from MC. The ratio of the two unfolded results is shown.

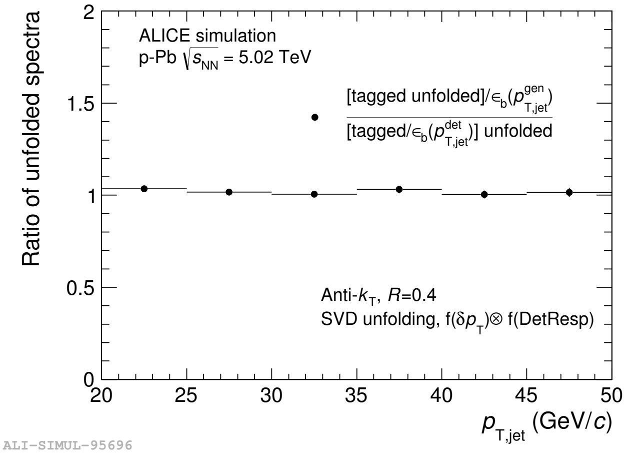

Figure 4: Comparison of two sequences of corrections: SVD unfolding and correction for tagging performance and vice versa. The ratio of the two corrected spectra is shown.

4 Summary

The performance of the b-jet tagging algorithm based on displaced secondary vertices was studied with MC simulation of p-Pb events for ALICE detector. The presented results were carried out in the jet p_T range $20 < p_{T,jet} < 50$ GeV/c.

For the selected operating point the tagging efficiency is at the level 20% while the mistagging efficiency for light-flavour jets is two orders of magnitude lower, which should result in high purity of the algorithm. The rejection of tracks with V0 topology is expected to enhance the algorithm performance by reducing light-flavour contamination and is currently under investigation.

Corrections for detector response and background fluctuations were studied. It was found that the b-jet spectrum can be corrected with a detector response matrix for inclusive jets. The order of corrections (tagging efficiency vs unfolding) gives compatible results.

References

[1] Y. L. Dokshitzer, D. E. Kharzeev, Phys. Lett. **B519**, 199 (2001).

[2] N. Armesto, C. A. Salgado, U. A. Wiedemann, Phys. Rev. **D69**, 114003 (2004).

[3] J. Huang, Z. Kang, I. Vitev, Phys.Lett. **B726**, 251 (2013).

[4] ALICE Collaboration, B. Abelev et al., Int. J. Mod. Phys. **A29**, 1430044, (2014).

[5] R. Brun, F. Carminati, CERN Program Library Long Writeup W5013, (1993).

[6] T. Sjoestrand, S. Mrenna, P. Skands, JHEP **05**, 026 (2006);
P. Z. Skands, Phys. Rev. **D82**, 074018, (2010).

[7] X.N. Wang, M. Gyulassy, Phys.Rev. **D44**, 3501, (1991).

[8] S. Chatrchyan *et al.* [CMS Collaboration], JHEP 04 (2012) 084.

[9] V. Khachatryan *et al.* [CMS Collaboration], arXiv:1510.03373 (2015).

[10] J. Adam *et al.* [ALICE Collaboration], Phys. Lett. **B749**, 68 (2015).

[11] M. Cacciari, G. P. Salam, Phys. Lett. **B641**, 57, (2006).

[12] S. Chatrchyan *et al.* [CMS Collaboration], JHEP **1208**, 130, (2012).

[13] A. Hocker, V. Kartvelishvili, Nucl. Instrum. Meth. **A372**, 469, (1996).

Nuclear effects in gauge bosons production

Michal Krelina*(mkrelina@hotmail.com)*

In this work, nuclear effects in Drell-Yan production in association with Z^0 boson in $p{+}Pb$ collisions at LHC within the color dipole approach are studied. There, various dipole cross section are tested and the impact of each investigated nuclear effects are studied. We focused on quark shadowing, gluon shadowing and effective energy loss. The results of this work were published in [1]. Here, nuclear effects will be studied through the the nucleus-to-nucleon ratio, the so called nuclear modification factor, $R_{pA} = \sigma^{p+A\to ll+X}/A\sigma^{p+p\to ll+X}$.

The color dipole formalism is treated in the target rest frame, where the Drell-Yan production can be viewed as a radiation of a virtual photon by a projectile quark. Assuming only the lowest $|q\gamma^*\rangle$ Fock component, the pseudorapidity or the p_T distribution of the photon bremsstrahlung in quark-nucleon interaction can be expressed as a convolution of the dipole cross section $\sigma_{q\bar{q}}(\rho)$, which is function of the transverse separation, and the light-cone (LC) wave function of the projectile $q\gamma^*$ fluctuation [2]. The differential hadronic cross section for Drell-Yan production in $p+p$ collisions can be expressed as a convolution of the qN differential cross section with corresponding parton distribution functions. The Z^0 boson, which has a large impact for the Drell-Yan production at LHC energies, can be included by adding the next LC wave functions [3].

Next, we consider several phenomenological models for the dipole cross section which take into account the DGLAP evolution or BK evolution as well as the saturation effects. For comparison with the previous results existing in the literature, we consider the Golec-Biernat-Wusthoff (GBW) model [4], models based on the DGLAP evolution denoted as BGBK [5] and IP-sat [6], which is generalization of the BGBK model in order to take into account the impact parameter dependence of the dipole-proton cross section. Finally, we also consider the running coupling solution of the BK equations for the partial dipole amplitude obtained in [7] using the GBW model as an initial condition.

The magnitude of nuclear effects within the color dipole framework is controlled by the coherence length, l_c. In the case of LHC energy of proton-lead collisions the coherence length is enough long to safe use the long coherence length (LCL) limit [8] for quark-nucleus cross section, where the dipole cross section is modified

$$\sigma_{q\bar{q}}(\rho) \Rightarrow \sigma^A_{q\bar{q}}(\rho) = 2\int d^2b\, \left(1 - \exp\left(-\frac{1}{2}T_A(b)\sigma_{q\bar{q}}(\rho)\right)\right), \tag{1}$$

where $T_A(b)$ is the nuclear thickness function. Due to the calculation in the lowest Fock state, $|qG^*\rangle$, the quark shadowing and quark broadening are included in the LCL limit. Therefore, the gluon shadowing corrections are calculated separately that correspond to the Fock states with at leat one gluon, $|qG^*g\rangle$. The corresponding suppression factor R_G

is calculated as the correction for the longitudinally polarized photons in the nuclear DIS using the Green function technique for the $|qG^*g\rangle$ Fock state [9].

The last studied effect is the effective energy loss due to the initial state interactions (ISI effects) [10]. This effect aspirates to explain observed suppressions at high transverse momentum and at forward rapidities at RHIC and LHC, see our previous publication, that cannot be fully or not at all explained by the coherence effects such as nuclear shadowing or color glass condensate (CGC). This effect also lead to the breakdown of the QCD factorization.

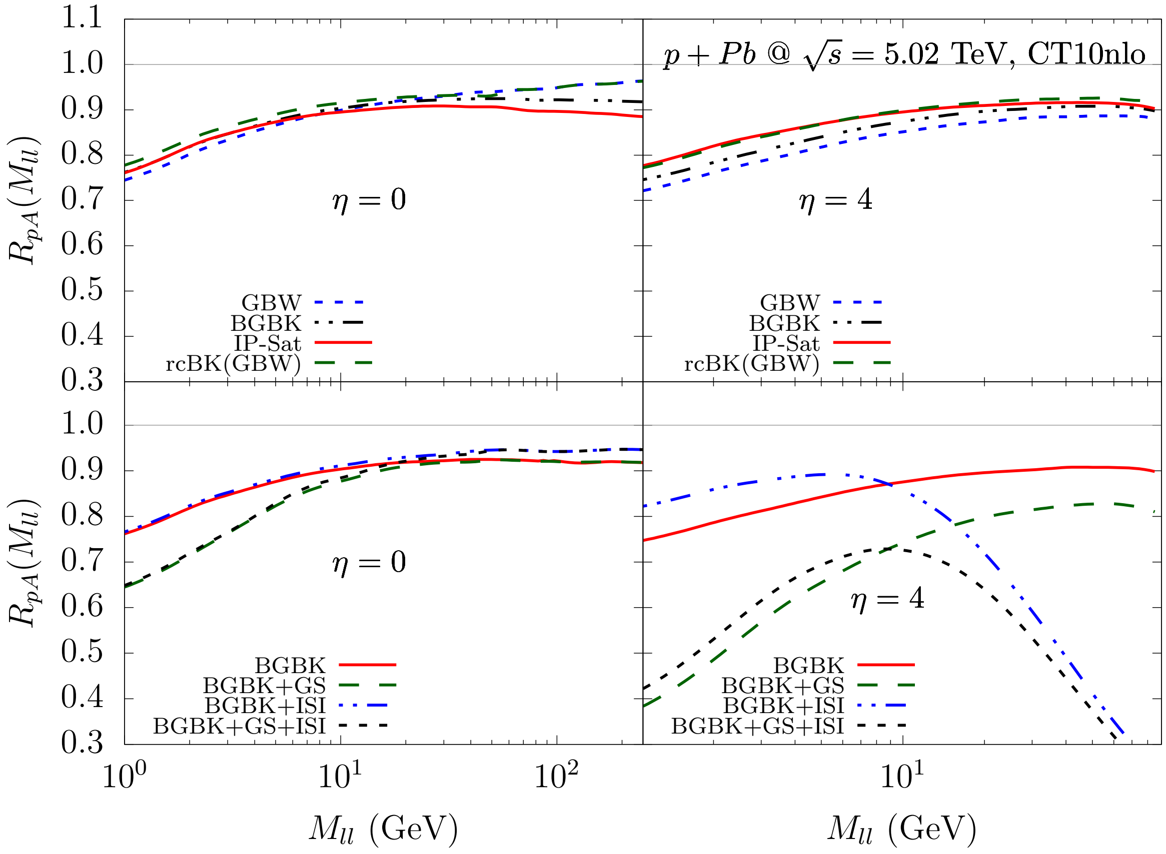

Figure 1: Nuclear modification factor for the Drell-Yan production: using LCL limit and various dipole cross sections (top) and the comparison of LCL limit, gluon shadowing correction and ISI effects (bottom) as function of the dilepton mass.

Predictions for the nuclear modification factor for the Drell-Yan production at the LHC for $p + Pb$ collisions are presented in Fig. 1 as a function of the dilepton mass and in Fig. 2 as a function of the transverse momentum. In both figures the top graphs using the LCL limit only and compare various dipole cross sections. Bottom graphs were calculated only for BGBK model and compare the impact of each studied nuclear effects.

In Fig. 1 the suppression up to the mass of 200 GeV is predicted. For small dilepton masses at midrapidity and for all dilepton masses at forward rapidity stronger suppression is predicted due to the gluon shadowing. Moreover, for the forward rapidities the strong suppression due to the ISI effects is expected at large dilepton masses, where the momentum fraction $x_2 \to 1$. In Fig. 2, next to the suppression due to the nuclear shadowing, we predict also small Cronin effect, whose magnitude and shape depends on the chosen

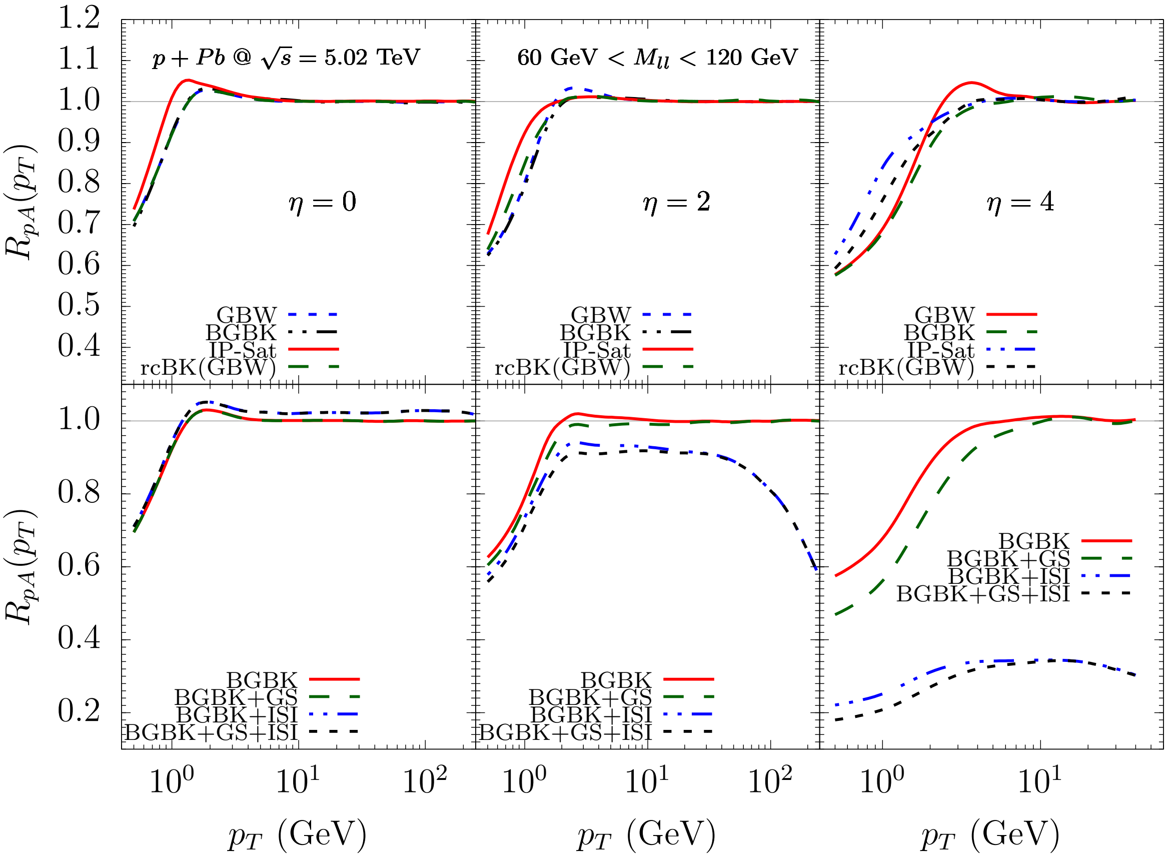

Figure 2: Nuclear modification factor for the Drell-Yan production: using LCL limit and various dipole cross sections (top) and the comparison of LCL limit, gluon shadowing correction and ISI effects (bottom) as function of transverse momentum.

dipole cross section. Finally, at forward rapidity we predict a very strong suppression due to the ISI effects that can be verified by the future measurements at the LHC.

References

[1] E. Basso, V. P. Goncalves, M. Krelina, J. Nemchik, and R. Pasechnik, (2016), arXiv:1603.01893.

[2] B. Z. Kopeliovich, A. V. Tarasov and A. Schafer, Phys. Rev. C59, 1609 (1999).

[3] R. Pasechnik, B. Kopeliovich, and I. Potashnikova, Phys. Rev. D86, 114039 (2012), arXiv:1204.6477.

[4] K.J. Golec-Biernat, M. Wusthoff, Phys. Rev. D59, 014017 (1998).

[5] J. Bartels, K. Golec-Biernat, and H. Kowalski, Phys. Rev. D66, 014001 (2002).

[6] H. Kowalski, L. Motyka and G. Watt, Phys. Rev. D74, 074016 (2006);
A.H. Rezaeian, M. Siddikov, M. Van de Klundert and R. Venugopalan, Phys. Rev. D87, 034002 (2013).

[7] J.L. Albacete, N. Armesto, J.G. Milhano and C.A. Salgado, Phys. Rev. D80, 034031 (2009).

[8] B.Z. Kopeliovich, L.I. Lapidus, A.B. Zamolodchikov, JETP Lett. 33, 595-597 (1981).

[9] B.Z. Kopeliovich, A. Schaefer, and A.V. Tarasov, Phys. Rev. D62, 054022 (2000);
B.Z. Kopeliovich, J. Nemchik, A. Schaefer, Phys. Rev. C65, 035201 (2002);
B.Z. Kopeliovich, J. Nemchik, I.K. Potashnikova, I. Schmidt, J. Phys. G35, 115010 (2008).

[10] B.Z. Kopeliovich, J. Nemchik, I.K. Potashnikova, M.B. Johnson, I. Schmidt, Phys. Rev. C72, 054066 (2005);
B.Z. Kopeliovich, J. Nemchik, I.K. Potashnikova, I. Schmidt, Int. J. Mod. Phys. E23, 1430006 (2014).

Heavy Flavor Tracker Pixel simulator

Jakub Kvapil*(kvapijak@fjfi.cvut.cz)*

STAR main midrapidity detectors are Time Projection Chamber (TPC), Time of Flight (TOF), Muon Telescope (MTD) and Heavy Flavor Tracker (HFT). Heavy Flavor Tracker (HFT) was installed in January 2014 and consists of two Pixel layers at 2.8 and 8 cm from the beampipe, Intermediate Silicon Tracker (IST) at 14 cm and Silicon Strip Detector (SSD) at 22 cm.

Pixel detectors are using the Monolithic Active Pixel Sensors (MAPS) technology which is used for the first time in collider experiments. The problem that had to be overcome during the construction of the MAPS sensors is that different silicon properties are needed for sensor and electronics. Advantage of MAPS technology in comparison to Hybrid technology is that sensors can be smaller, thinner, and thus have smaller capacitance and noise level. This, moreover, decreases the overall material budget of the vertex detector. They can measure higher particle density, therefore can be placed closer to the interaction point. The disadvantage of the MAPS technology is that MAPS have smaller radiation tolerance. The MAPS sensors are not fully depleted. Thus, the charge collection is conducted in part thanks to electron diffusion, in addition to the drift, present in the hybrid sensors.

HFT significantly improves open heavy flavor measurements, greatly benefiting from the excellent resolution of primary and secondary vertices which is greater than 30 um. The mean decay length for D^0 is 120 μm, for λ_c 60 μm and for $B-mesons$ 500 μm. Due to 1 mm TPC resolution without HFT it is impossible to distinguish between primary and secondary vertices of these particles. HFT suppresses the combinatorial background of 4 orders of magnitude as can be seen on D^0 invariant mass graph in Figure 1. The intercept graph shows signal with and without HFT. Without HFT, no peak in signal can be measured.

DIGMAPS is a slow simulator developed to simulate MAPS sensors. In comparison to a fast simulator, DIGMAPS can simulate MAPS sensor response to the level of a single pixel. DIGMAPS uses several input parameters, e.g. pitch, epitaxial layer thickness, ADC threshold, etc. The simulation consists of several steps: First particle is generated with only angular dependence, energy dependence is not implemented. Then the particle traverses through the sensor, deposits energy and creates electron-hole pair which obey Landau law with MPV = 80 $e^-/\mu m$. After the charge is transported to collecting N-well diodes which is approximated by Lorentzian and Gaussian. Finally, zero suppression and clustering is done. The clustering counts all the hits in the simulated sensor. DIGMAPS has been tuned for cosmic data as can be seen in Figure 2. The blue line is simulation for 5° and the red dots are data for angle between 0° and 10°.

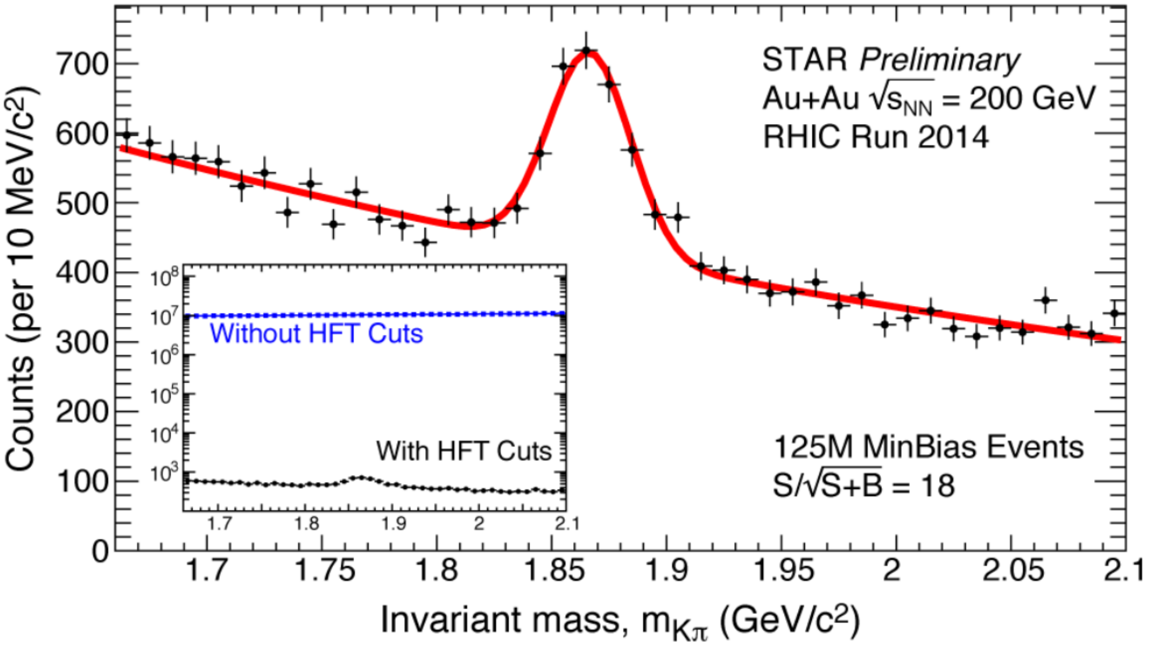

Figure 1: Invariant mass of D^0 and signal with and without HFT. [1]

Now, simulator needs to be tested on all particle species. That has been done with Run14 low luminosity Au+Au 200 GeV data. After the reconstruction, we check cluster size as it is the only variable we can compare between data and simulator. It is expected that most of the hits will have cluster size 1, after cuts to eliminate fake hits it is, however, expected that the peak will appear at around $3-4$.

In the reconstruction PXL and IST were included in tracking. It is required to have at least one hit in each HFT layer in IST window 1×4 mm and PXL windows 20×20 μm. Using global tracks the result can be seen in Figure 3. The blue area represents simulation scaled to data (red points). The simulation fits the data at high cluster sizes. Additional cuts are needed to improve fit of smaller cluster sizes. The 3-size drop is similar to drop in cosmic with unknown origin.

The results were improved can be done using primary tracks only. We will require exactly one hit in each layer. We will raise the PXL windows obtained from fit by separating inner and outer layer. Finally, we can make PID for protons, Kaons and Pions.

DIGMAPS can greatly improve accuracy of the simulations together with noise estimate. In conclusion, a comparison between the slow simulator and detector response from the Pixel detector has been done. The results show good agreement in high cluster sizes (more than 5). However, more checks have to be made to show that the slow simulator DIGMAPS simulates the data realistically.

References

[1] G. Van Buren. Vertex 2015, Santa Fe, USA.

[2] M. Šimko. Vertex 2015, Santa Fe, USA.

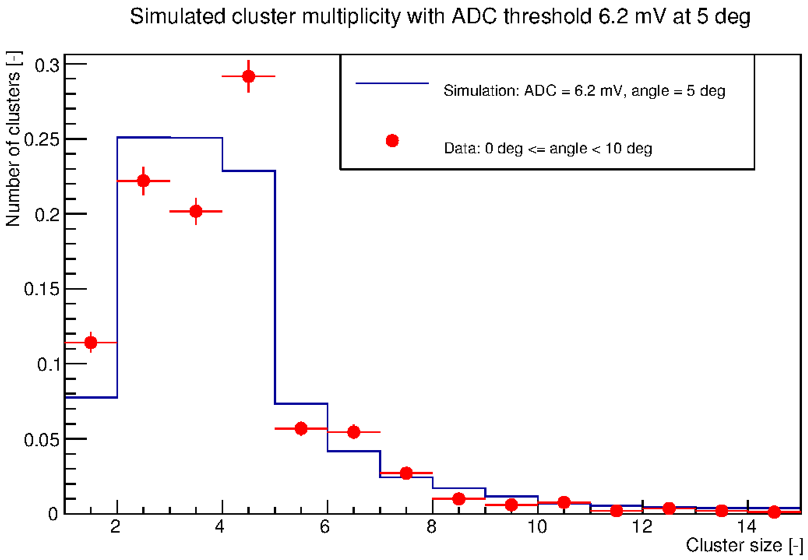

Figure 2: DIGMAPS simulation for 5° (blue) and cosmic data for angle 0° and 10°. [2]

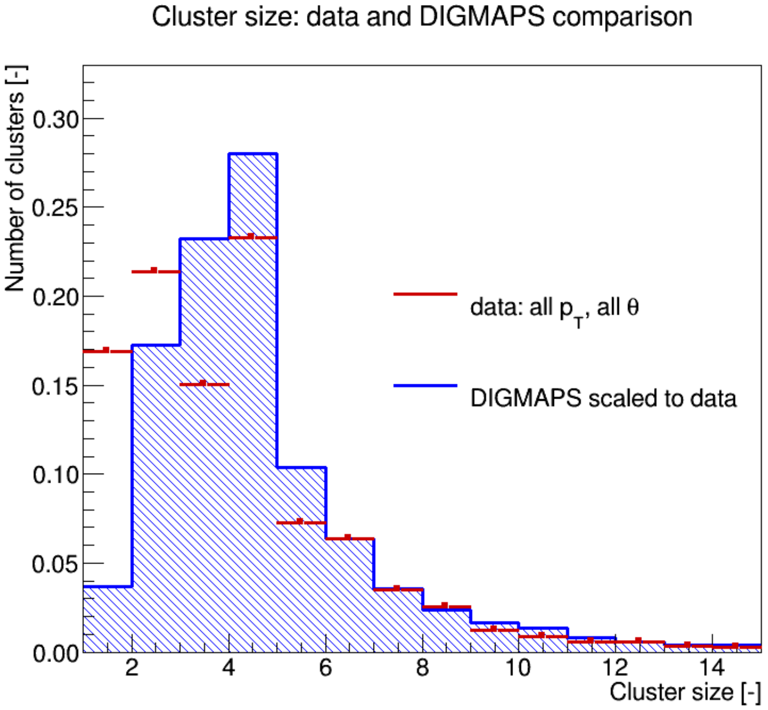

Figure 3: Simulation (blue) scaled to data (red) for all angles.

t-Dependence of the cross section for the coherent production of J/ψ in Pb-Pb UPC

Roman Lavička*(roman.lavicka@cern.ch)*

Here, I present my progress on results for my diploma thesis, which is the analysis of coherent J/ψ production at mid rapidity with ALICE in ultra-peripheral collisions (UPC) of lead-lead beams at LHC.

UPC occur when two projectiles interact at an impact parameter larger than the sum of their radii. What happens is, that the strong interaction is suppressed and they interact principally via their clouds of quasi-real photons. Number of quasi-real photons is proportional to Z^2. This fact brings an idea to use heavy-ion collisions to study electromagnetic interactions. Pb-Pb collisions at LHC offers interesting data, which can be analyzed in many ways.

The goal of my work is to study the dependency of coherent J/ψ production cross section on the Mandelstam variable t, which in this case describes the amount of transfered momentum between target nucleus and resulting vector meson. This we want to study on data, which were measured in 2011, and if the reconstruction of newly collected 2015 data will go according to the time schedule, we will include results on these data to the diploma thesis as well. In general, data need to be corrected for detector effects. Monte Carlo simulations are usually produced for this reason. In the talk I gave at this workshop I summarize my results obtained from Monte Carlo simulated by STARLIGHT. This simulation produces decays of J/ψ mesons to dimuons from UPC lead-lead collisions at the energy of 2.76 TeV. Three samples are available. One with J/ψ produced coherently, one with incoherent production and one contains a di-lepton events. In the presentation I talked about the coherent sample.

Since we want to obtain the t-dependence of the cross section, we want to fit the behavior of p_t^2 distribution of the J/ψ. But as it can be seen in the Figure 1, it is not exactly equal to the wanted transfered momentum t, but one has to also take into account a contribution of the quasi-real photon, which comes from the second nucleus and it is needed to satisfy the momentum conservation law. Because of the lack of information about the momentum of the photon and t, we prepared a new simulation of 500 000 events, which contains the information. We found out that we cannot simply neglect the photon momentum and an extra correction has to be introduced.

A correction for detector effects was also prepared. In principle, we just took the p_t^2 distribution of the generated particles and divided it by the p_t^2 distribution of the reconstructed tracks.

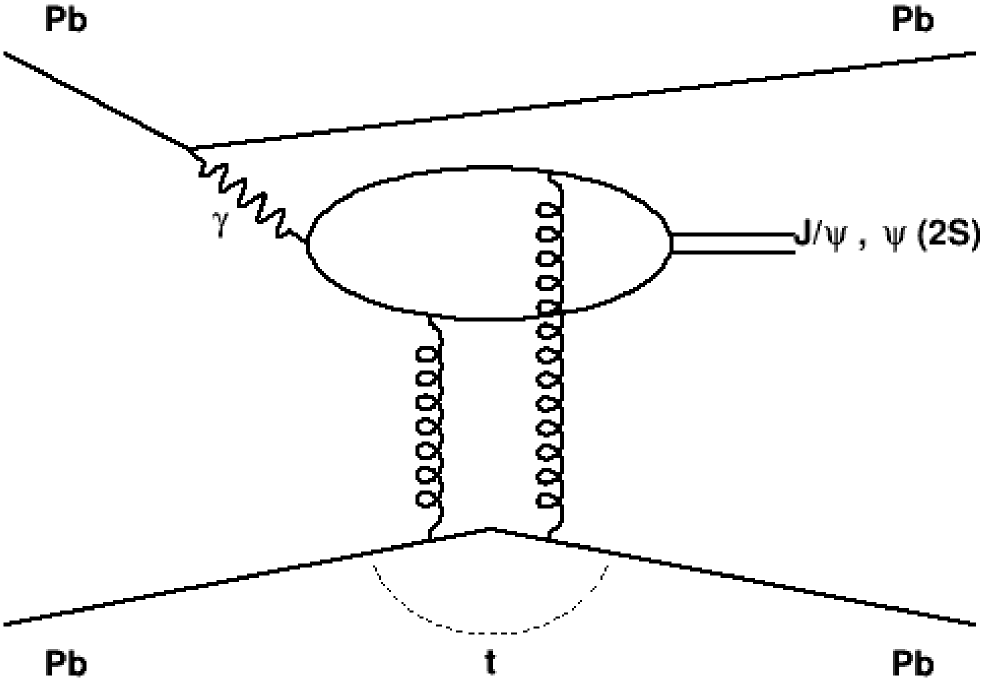

Figure 1: A diagram of the process Pb + Pb → $\mu\mu$. t is the Mandelstam variable, other symbols are names of the particles.

Both distributions had the same binning, which was also obtained from the Monte Carlo simulations. For this process we need to plot an efficiency and purity of the sample. The efficiency shows us, how p_t of generated particles migrates for reconstructed tracks, i.e. if for the same event we find a p_t value in the same bin both the generated particles and the reconstructed tracks. The binning, which yields the smallest migration, tell us, that this binning will be recover the p_t with the best efficiency. The purity process is conceptually the same one, but we are looking for the migration of p_t from reconstructed particles to generated particles. This plot tell us, how big error we should expect for each bin.

All these corrections and binning were applied on the p_t^2 distribution of the reconstructed tracks and this was fited with the function which was used by STARLIGHT to generated trasfered momentum t. In the formula we have 2 unknown parameters, we want to get from the fit. The first is the range of the Yukawa potential a and the second is the transversal nucleus radius R_A. STARLIGHT uses theoretical values $a = 0.7$ fm and $R_A = 6.62$ fm. Our fits of samples of reconstructed tracks with 291 events give us values, which are in a good agreement with the simulation.

The next step is to use the corrections and the binning on the measured data and obtain the fit. The results will be published in my diploma thesis, which is planned to be defended in June 2016.

References

[1] B Abelev et al. [ALICE Collaboration], Charmonium photoproduction at midrapidity in ultra-peripheral Pb-Pb collisions at $\sqrt{s} = 2.76$ TeV, arXiv:1305.1467 [nucl-ex]

[2] K. Aamodt et al., The ALICE experiment at the CERN LHC, ALICE Collaboration, 2008. 259 pp., Published in JINST 3 (2008) S08002

[3] A. J. Baltz, S. R. Klein and J. Nystrand, Coherent vector meson photoproduction with nuclear breakup in relativistic heavy ion collisions, Phys. Rev. Lett. **89** (2002) 012301 doi:10.1103/PhysRevLett.89.012301 [nucl-th/0205031].

Quarkonia And Their Production

Robert Licenik*(licenrob@fjfi.cvut.cz)*

1 Overview & Motivation

This paper gives a brief overview of the quarkonia-QGP relation including both theoretical and experimental parts (with results from both LHC and RHIC). It also summarizes the author's bachelor thesis topic (Υ production at STAR experiment, supervised by Dr. Olga Rusnakova) and states its main objective.

Quarkonia serve as a probe in quark-gluon plasma (QGP). Quarkonia production and its suppression are measured to help determining the QGP temperature which is key to obtaining its phase diagram which would help pushing the boundaries of human understanding of nature.

2 Quarkonia & Quark-Gluon Plasma

Quarkonium is a bound state of a quark-antiquark pair. Only bound $c\bar{c}$ and $b\bar{b}$ pairs are called (heavy) quarkonia (charmonium, bottomonium). The charmonia have masses between $m_{J/\psi} = 3.1$ GeV/c^2 of J/ψ meson and $m_{2D^0} = 3.8$ GeV/c^2 which is the mass of 2 D^0 mesons - the open charm threshold. For bottomonia, the range is between $m_\Upsilon = 9.5$ GeV/c^2 of $\Upsilon(1S)$ meson and the open beauty threshold $m_{2B^0} = 10.6$ GeV/c^2. Their formation is not yet fully understood in the QCD framework. As the author focuses on the $\Upsilon(nS)$ mesons - with main objective to obtain the invariant mass spectrum of the particle - so does this paper.

Quark-gluon plasma is a state of matter where quarks and gluons are thought to be free as opposed to being confined in hadrons. An early Universe is thought to be in this state. However, this state of matter is not observable in present Universe, so particle colliders (RHIC, LHC) are built and QGP is created in nucleus-nucleus collisions. High A nuclei (Au, Pb, U) are commonly used. QGP physics is not well understood yet, but experiments show that there are similarities with ideal fluids. The main goal is to obtain a phase diagram (dependence of temperature on baryonic chemical potential) of QGP and find the critical point.

3 Basic Theory

Because of their high rest masses, quarkonia can be considered to be non-relativistic. Therefore, NRQCD can be used for computation. They are mainly produced during the hard scattering. Several theoretical models are used to describe the production of quarkonia in p-p collisions (CSM, CEM, NRQCD,...). However, neither is fully predictive. To compare the production in A-A collisions to p-p collisions, Nuclear Modification Factor is introduced. It is defined as a ratio of overall A-A collision yield and cross section in p-p collision multiplied by mean value of nucleons participating in the collision:

$$R_{AA} = \frac{N_{AA}}{\langle T_{AA} \rangle \times \sigma_{pp}^{q\bar{q}}}. \tag{1}$$

Intuitively, this factor should have a value of 1. This is not the case as seen (4, 5). First proposed in 1986 [1], the free charges in QGP cause the confinement radius r_c to decrease with increasing temperature. When this temperature rises above certain value ($T > T_c$), the quarks cannot see each other and the quarkonium melts. Other factors, including cold nuclear matter effects, shadowing, anti-shadowing, regeneration, feed down and hydrodynamics have to be included in theoretical models describing the quarkonia production suppression by QGP formation.

There are several properties that make Υ mesons a more convenient QGP probe than ψ mesons. First of all, there are three Υ states as opposed to only two ψ states. This is a major advantage as it provides finer scale for the QGP temperature. Furthermore, those states are closer in relative abundance (7:2:1 ratio for Υ, 50:1 for ψ) so they stay more easily observable during the suppression. Another advantage is that the Υ states have much higher mass. As a result, they decay almost at rest and their decay products - leptons - are more energetic and scatter at very high mutual angle (close to π). This leads to an easier detection, as they are very specific. The high mass of Υ also eliminates any further production after the hard scattering. Finally, there is no feed down from b quark decay. There are some disadvantages, however. One are the more complex decay channels/feed down, so there are higher requirements for detector resolution. The other is the lower total abundance, which is a problem at RHIC energies. However, at LHC energies, the production of Υ is comparable to ψ.

4 Experimental Results

The Υ invariant mass spectrum measurement has been conducted at both LHC and RHIC. As seen in 3, STAR detector is unable to detect separate resonances - producing a combined peak in the invariant mass spectrum instead - at RHIC energies. At LHC energies, it is possible to detect peaks from all resonances separately, as seen in 1. In 2, a comparison between invariant mass spectrum obtained in A-A collisions and the one from p-p collisions can be seen. The difference of the peak height is clearly visible, indicating the existence of QGP resulting in the suppression as described before.

The measurement of R_{AA} is also conducted at both RHIC and LHC energies, the main objective being obtaining its dependence on rapidity and centrality of the collision. Taking errors in consideration, the dependence of R_{AA} on centrality can be considered to be well described by theoretical models. The observed trend is in line with expectations, as the values of R_{AA} gradually decrease with increasing number of participants in the collision (4). The same cannot be said about the results from measurements of R_{AA} dependence on rapidity, where there is a discrepancy between theoretical models and LHC data (5).

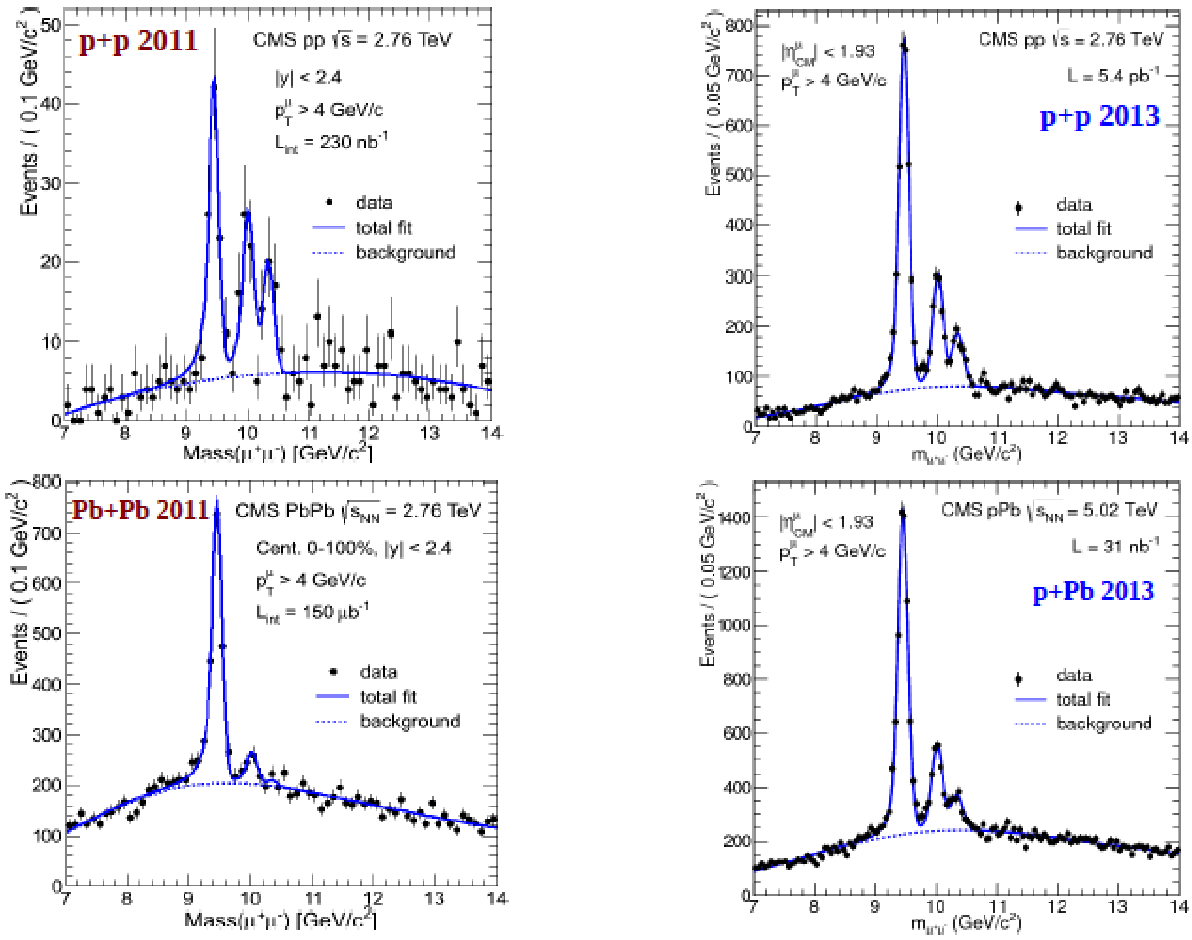

Figure 1: CMS results of invariant mass spectrum of $\Upsilon(nS)$ in p-p, p-A, A-A collisions [5]

5 Summary & Outlook

Measurements of quarkonia production in A-A collisions serve as a probe in a state of matter the early Universe is thought to be in. The formation of QGP causes the quarkonia to melt, so the temperature interval the QGP is in can be determined by measuring yields of different quarkonia. The main parameter characterizing the suppression is the nuclear modification factor, R_{AA}. Its dependence on the number of participants is described sufficiently, while solid theoretical models for rapidity dependence are lacking and have to be introduced or implemented in existing theoretical models for them to be more consistent with data. Determining the temperature of QGP is a crucial step in creating the phase diagram of the QGP.

References

[1] T. Matsui, H. Satz, Phys. Lett. B178, 416 (1986)

[2] R.J.Reed, "Υ production at $\sqrt{s_{NN}}$ = 200 GeV in p+p and Au+Au collisions at STAR", Dissertation Thesis, UC Davis, 2011

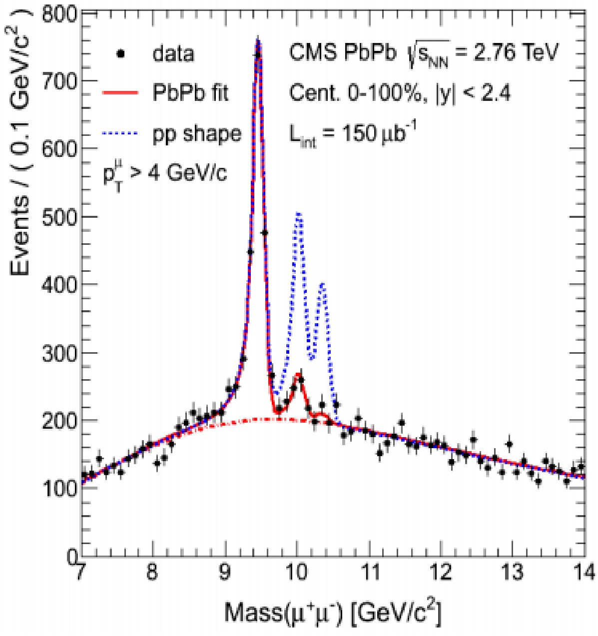

Figure 2: CMS result of invariant mass spectrum of $\Upsilon(nS)$ in A-A compared to p-p collisions, [4]

[3] A. Andronic *et al.*, "Heavy-flavour and quarkonium production in the LHC era: from proton-proton to heavy-ion collisions", arXiv:1506.03981 [nucl-ex].

[4] S. Chatrchyan *et al.*, "Observation of Sequential Υ Suppression in PbPb Collisions", Phys. Rev. Lett. 109, 222301, 26 November 2012

[5] Abdulla Abdulsalam, "Bottomonium production in p+p, p+Pb and Pb+Pb collisions with CMS", Quark Matter 2014, Darmstadt

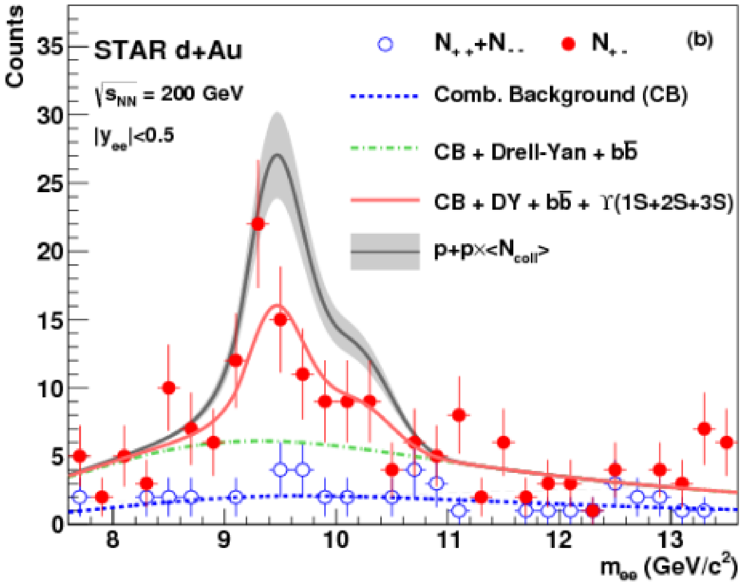

Figure 3: STAR result of invariant mass spectrum of $\Upsilon(nS)$ in d-Au collision, arXiv:1312.3675 [nucl-ex]

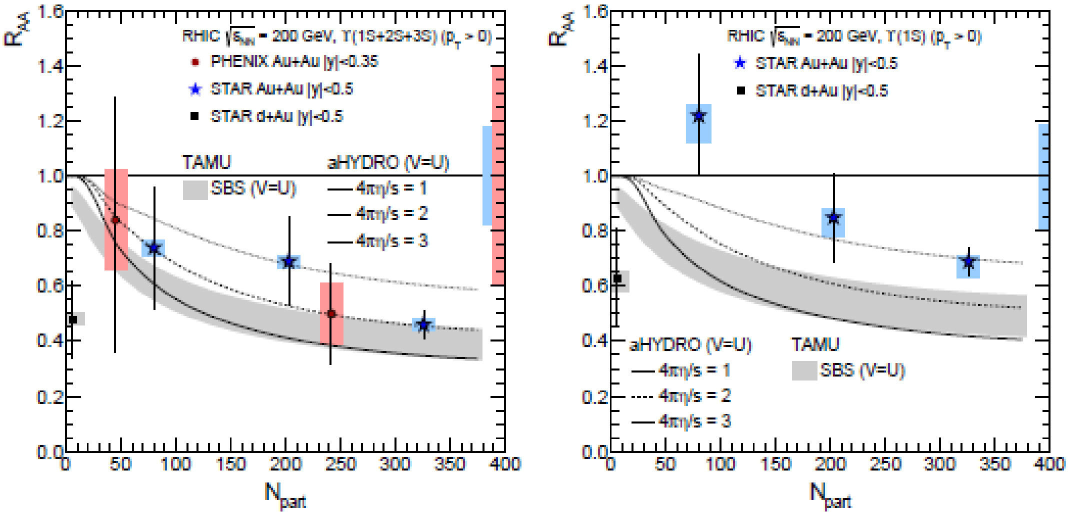

Figure 4: R_{AA} dependence on collision centrality N_{part} @RHIC [3]

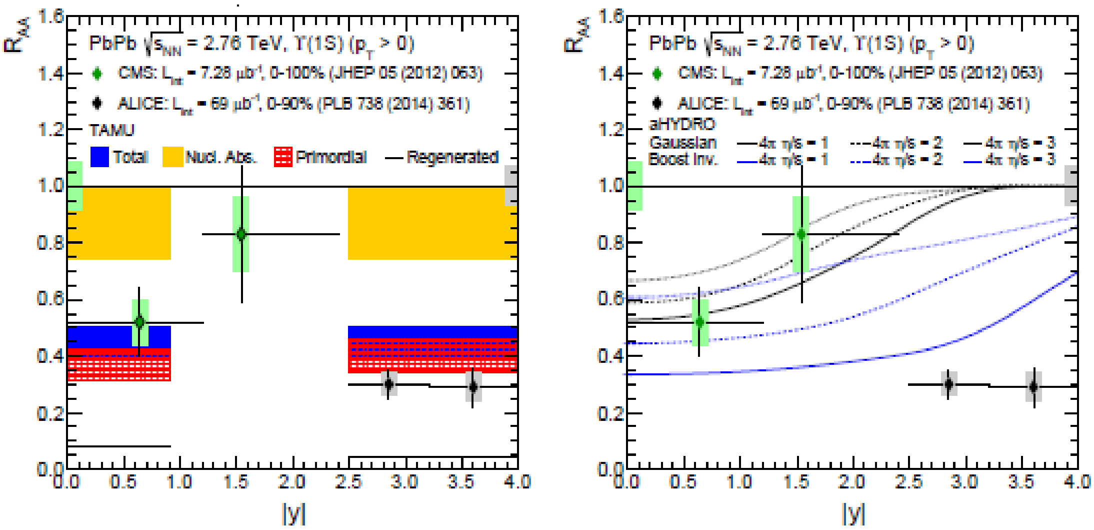

Figure 5: R_{AA} dependence on rapidity @LHC [3]

Non-identical kaon femtoscopy at STAR experiment

Jindřich Lidrych *(lidryjin@fjfi.cvut.cz)*

---

1 Abstract

In the collisions of heavy-ions the nuclear matter can undergo a phase transition from hadrons to a state of deconfined quarks and gluons called the Quak-gluon Plasma. Femtoscopic measurements of two-particle correlations at small relative momenta reveal information about the space-time characteristics of the system at the moment of particle emission. The correlations result from quantum statistics, final-state Coulomb interactions, and the strong final-state interactions between the emitted particles.

It has been predicted that correlations due to the strong final-state interactions in a system where a narrow resonance is present will be sensitive, in the region of the resonance, to the source size and momentum-space correlations. Such a measurement can provide complementary information to the measurements at very low relative momenta. This paper presents theoretical background how to experimentally measure the unlike-sign kaon correlations function including the region of $\phi(1020)$ resonance.

2 Introduction

In the 1950s Robert Hanbury Brown and Richard Q. Twiss invented a technique allowing to measure space characteristics of stellar objects based on measurements of the photon intensity interferometry [1]. Few years later, in 1960, similar technique was used in particle physics to describe observed enhancement of the identical pion pairs produced in the proton-antiproton annihilation by Goldhaber and his collaborators [2]. These observed correlations, as experimenters correctly asserted, came as a result of quantum statistics. Based on this observation the theoretical background of femtoscopy was developed by G. I. Kopylov and M. I. Podgoretsky in the 1970s [3]. Since then the femtoscopic measurements of two-particle correlations at low relative momenta became a standard tool for extracting the space-time extents of particle emitting sources. Nowadays femtoscopic studies include identical particles, as well as non-identical interacting particles [4, 5, 6, 7].

The approach proposed by Lednicky [8] extends the femtoscopic formalisms to higher relative momenta between the two emitted particles in a system where the final-state interactions (FSI) contain a narrow, near-threshold, resonance. It is predicted that the correlation function will be more sensitive in the region of the resonance, where the strength of the correlation should change with the source size, r as $\sim r^{-3}$ in comparison with measurements at the very low relative momenta, where the correlation function depends on r^{-2} or r^{-1}. In addition, these measurements will be statistically advantageous, since the particle spectra fall rapidly at low relative momenta.

Pairs of unlike-sign kaons are ideally suited for such femtoscopic analysis as they contain the narrow $\phi(1020)$ resonance. The $\phi(1020)$ resonance is characterized by the decay width $\Gamma = 4.3$ MeV and the decay momentum in the rest frame $k^* = 126$ MeV/c. It is hoped, that at the low q_{inv}, the attractive Coulomb interaction and strong interaction in s-wave will be able to observed, while in the region of $q_{inv} \sim 0.25$GeV/c the strong interaction in p-wave via $\phi(1020)$ resonance in FSI should be present.

3 Methods

The data, which can be used for this analysis, will be collected in Au+Au collisions at $\sqrt{s_{\mathrm{NN}}} = 200$ GeV by the Solenoidal Tracker at RHIC (STAR) [9]. The most important subdetectors for kaon identification are the Time Projection Chamber (TPC) and the Time of Flight (ToF). The TPC records charged particle tracks and measures their momentum p, while the ToF measure particle velocity β, which is consequently used to calculate particle mass m according the relation

$$\frac{1}{\beta} = \sqrt{1 + m^2/p^2}, \tag{1}$$

where the momentum p is measured by the TPC.

Experimentally, the two-particle correlation function $CF(q_{inv})$ will be constructed as the ratio of the correlated two-particle distribution from the same event, $N_{same}(q_{inv})$, and the uncorrelated two-particle distribution from mixed events, $N_{mixed}(q_{inv})$:

$$CF(q_{inv}) = \frac{N_{same}(q_{inv})}{N_{mixed}(q_{inv})} = \frac{\text{real pairs}}{\text{mixed pairs}}, \tag{2}$$

where $q_{inv}^2 = -(p_1^\mu - p_2^\mu)^2$.

For comparison of the experimentally obtained unlike-sign correlation function to the theoretical prediction, measurement of like-sign kaon correlation function will have to be performed. The kaon source radii R_{inv} and the λ parameters will be obtained from fitting experimental correlation functions with a standard Bowler-Sinyukov [10] form of one-dimensional correlation function.

The theoretical correlation function can be calculated by

$$CF\left(q_{inv}\right) = \int d^3 r S\left(r, k^*\right) \left|\psi_{1,2}\left(r, k^*\right)\right|^2, \tag{3}$$

where $S\left(r, k^*\right)$ is the source function describing emission of two particles at a relative distance r with the relative momentum k^* in the pair rest frame (PRF). The interaction between the two emitted particles is characterized by their wave function $\psi_{1,2}\left(r, k^*\right)$. Since the theoretical function does not include effects contained in the experimental λ parameter, it should be scaled for the comparison according to

$$CF = \left(CF^{theor} - 1\right)\lambda + 1, \tag{4}$$

where λ parameter will be obtained from the fit to the like-sign correlation function.

4 Conclusion

In this paper, the theoretical background for the construction of unlike-sign kaon correlation function has been presented. These predictions can be tried and tested on recent data from the STAR experiment.

References

[1] R. Hanbury Brown, R.Q. Twiss, Nature **178**, 1046-1048, (1956)

[2] G. Goldhaber, S. Goldhaber, W.Y. Lee, A. Pais, Phys. Rev. **120**, 300 (1960)

[3] G.I. Kopylov, Phys. Lett. **B50**, 472 (1974)

[4] B.I. Abelev et al. (STAR), Phys. Rev. **C80**, 024905 (2009)

[5] L. Adamczyk et al. (STAR), Phys. Rev. **C88**, 034906 (2013)

[6] L. Adamczyk et al. (STAR), Nature **527**, 345-348, (2015)

[7] L. Adamczyk et al. (STAR), Phys. Rev. Lett. **114**, 022301 (2015)

[8] R. Lednicky, Phys. Part. Nucl. Lett. **8**, 965 (2011)

[9] K.H. Ackermann et al. (STAR), Nucl. Instrum. Meth. **A499**, 624 (2003)

[10] M.G. Bowler, Phys. Lett **B270**, 69 (1991)

Study of properties of the dipole scattering amplitude using Balitsky-Kovchegov evolution equation

Marek Matas *(matas.marek1@gmail.com)*

1 Introduction

One of the most important ways to study the high energy limit of QCD is the Deep Inelastic Scattering at small values of Bjorken-x. Experimental results show that the gluon density grows with decreasing of the Bjorken-x. This increase in gluon density is thought to be eventually tamed by recombination. Balitsky-Kovchegov equation describes such systems and it is important to know how the solution depends on the implicit parameters of the numerical solution. We numerically solved the BK equation and searched for an optimal setup of parameters that would grant us a good running time while still keeping high precision. We also searched for initial condition that would require less parameters that need to be fitted from data and solved BK equation without neglecting the impact parameter-dependence.

2 Optimizing parameter setup

2.1 The rcBK evolution equation

The rcBK evolution equation with running coupling kernel reads [5].

$$\frac{\partial N(r,Y)}{\partial Y} = \int d\vec{r_1} K^{run}(\vec{r},\vec{r_1},\vec{r_2})(N(\vec{r_1},Y)+N(\vec{r_2},Y)-N(\vec{r},Y)-N(\vec{r_1},Y)N(\vec{r_2},Y)), \quad (1)$$

where $K^{run}(\vec{r},\vec{r_1},\vec{r_2})$ can be expressed as [9]

$$K^{run}(\vec{r},\vec{r_1},\vec{r_2}) = \frac{N_c \alpha_s(r^2)}{2\pi^2}\left(\frac{r^2}{r_1^2 r_2^2} + \frac{1}{r_1^2}\left(\frac{\alpha_s(r_1^2)}{\alpha_s(r_2^2)} - 1\right) + \frac{1}{r_2^2}\left(\frac{\alpha_s(r_2^2)}{\alpha_s(r_1^2)} - 1\right)\right), \quad (2)$$

$\vec{r_2} = \vec{r} - \vec{r_1}$ and $Y = ln\frac{x_0}{x}$. If we disregard the last term in Eq.1, we obtain a linear equation that can be shown to be equivalent to the BFKL evolution equation [4]. The running coupling depends on the number of considered quark flavors, in this work we use $n_f = 3$

$$\alpha_{s,n_f}(r^2) = \frac{4\pi}{\beta_{0,n_f} ln\left(\frac{4C^2}{r^2\Lambda^2_{n_f}}\right)}, \tag{3}$$

where

$$\beta_{0,n_f} = 11 - \frac{2}{3}n_f. \tag{4}$$

The constant C^2 is the uncertainty coming from the Fourier transformation and is usually fitted to data [1], $\Lambda^2_{n_f}$ is called the scale parameter and its value depends on the value of n_f (we set it to $\Lambda_{n_f} = 0.241\,\text{GeV}$). Since all dipole sizes are accounted for in the rcBK evolution equation, coupling needs to be reduced after a certain value is reached, so that the maximal value of the coupling constant would not exceed a set limit [1] (in our case $\alpha_s = 0.7$).

We used the MV initial condition [1] with parameters $C = 2.52, \Lambda_{QCD} = 0.241\,\text{GeV}$, $\gamma = 1.135$, $Q^2_{s0} = 0.165\,\text{GeV}^2$, $N_c = 3$ [1],

$$N^{MV}(r, x = x_0) = 1 - \exp\left(-\frac{(r^2Q^2_{s0})^\gamma}{4}\ln\left(\frac{1}{r\Lambda_{QCD}} + e\right)\right), \tag{5}$$

where e is the elementary charge.

2.2 Solving the rcBK evolution equation

The rcBK equation does not have an analytic solution, so it has to be solved numerically [3, 2, 1]. A usual way of solving this equation involves dividing the integral over r_1 into a logarithmic grid with a constant step, then one uses a Runge-Kutta method for solving the differential equation, the Simpson method for numerical integration and linear interpolation for acquiring values of $N(r)$ for an arbitrary point.

The parameters of the numerical computation have been varied and their influence to the resulting scattering amplitude was studied. The proportional change $D(r, Y)$ was computed as

$$D(r, Y) = \frac{\mid N_{orig}(r, Y) - N_{new}(r, Y) \mid}{N_{orig}(r, Y)}. \tag{6}$$

The initial values for the computation were 25 steps over one order of magnitude of the dipole size r over the interval $[10^{-7}, 10^2]$, 10 steps over the interval of $[0; \pi]$ in θ, which is the angle between r and r_1, and a Runge-Kutta method of fourth order with step of 0.01 in rapidity.

In Fig. 1 we can see the integrand for the structure function F_2 (see for example Eq. 9 in [7]) and its dependence on r for $Y = 2$ and $Y = 10$. We can see that the interval that contributes the most to the total value of F_2 is at about $r \sim (0.1, 20)\,\text{GeV}^{-1}$. The highest precision needs to be obtained namely for these values of r.

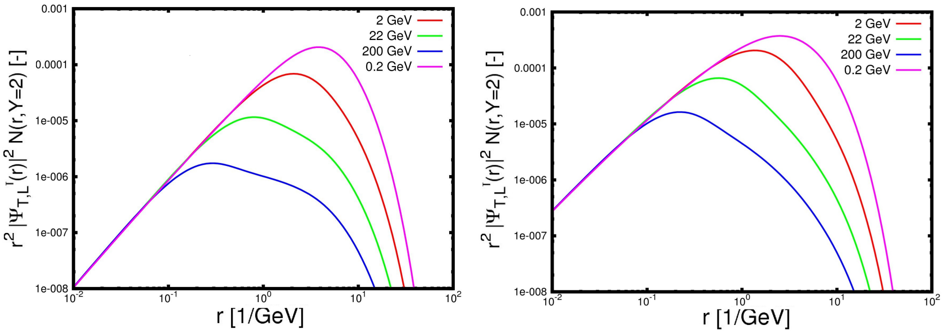

Figure 1: Integrand for the structure function as a function of r for $Y = 2$ (left) and $Y = 10$ (right). Each line corresponds to a different value of the photon virtuality Q^2.

2.3 Results

There is less than 0.7% difference in the rcBK solution when comparing first order Runge-Kutta method to the second order up to $Y = 10$ and less than 0.4% for comparing second order to fourth. Therefore, there is less than 1% uncertainty coming from the choice of the Runge-Kutta method and the uncertainty rises with rapidity. Considering the step in rapidity for the Runge-Kutta method, it can be seen that the difference between the step of 0.5 to the step of 0.1 is up to 4% and the biggest difference is in the region where the integrand dominates. Therefore it can be presumed that the uncertainty will also rise with rapidity. The difference between the step of 0.1 to the step of 0.05 is less than approximately 0.5%.

When the variation of the number of steps for the magnitude of r_1 is done from 10 steps to 25 steps per order of magnitude of r_1, the difference quickly rises with rapidity up to 2.5% at $Y = 10$. Using 50 steps instead of 25 steps does not yield any considerable difference for all rapidities. The results at low values of r have small significance since their contribution to the final structure function is negligible as shown in Fig. 1.

Also, the variation of the number of steps for the angle θ between $\vec{r_1}$ and $\vec{r}$ from 5 steps to 10 steps over the interval $[0, \pi]$ has been performed resulting in huge difference up to 25% which quickly rises with rapidity. Adding more steps does not yield to any notable difference.

Running time for a fixed scale was about 100 s on a regular personal computer and the mean square variation was below 1.5% of the experimentally measured values of F_2.

3 Geometrical scaling

We tried to find the "Eigen initial condition" for the rcBK evolution equation by running the MV initial condition up to high rapidity ($Y = 100$) where the integro-differential equation "forgot" the shape of the initial condition and then re-scaling it to the starting value. We used the effect called geometrical scaling that was observed with the rcBK evolution equation, which means that the shape of the solution does not change for higher values of rapidity, it only shifts towards lower values of r. The saturation scale Q_s^2 is a free parameter that needs to be fitted and it determines the position of shift of the solution $N(r, Y)$ by the condition $Q_s = 1/r_0$ and $N(r_o) = 0.5$. We used value of $Q_s^2 = 0.075$ *Gev*. The values of $\frac{F_2 data}{F_2 rcBK}$ were evaluated and fitted with a constant to determine the new value of σ_0 since the original value obtained with MV initial conditions can differ. A second propagation to $Y = 100$ and re-scaling of the initial condition was carried out to determine the validity of the assumption that by $Y = 100$, the rcBK equation "forgot" its initial condition. Fig. 2 shows the dependence of the solution on rapidity. It shows that its shape does not change significantly with increasing rapidity, it just shifts towards lower values of r.

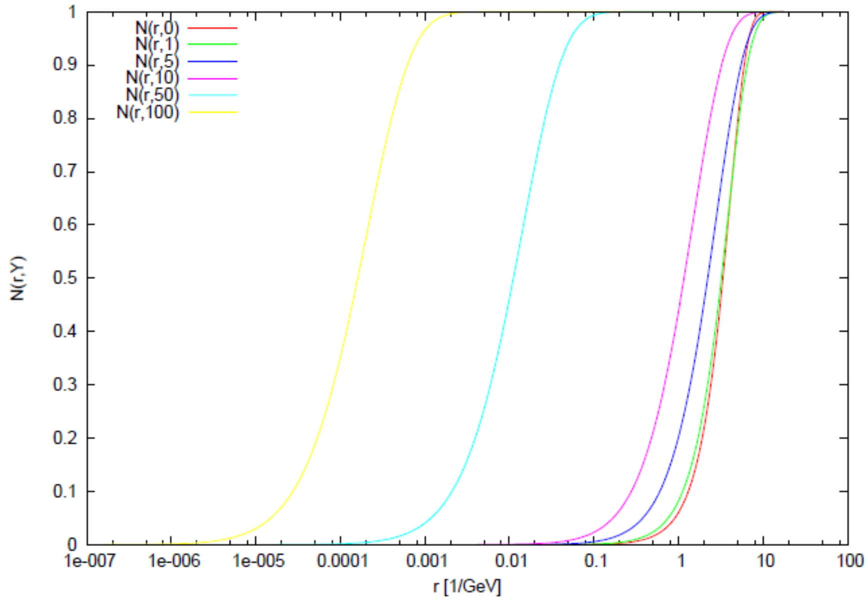

Figure 2: The shape of the solution to the BK equation shows geometrical scaling properties.

4 b-dependent solutions to the BK equation

Of course, the approximation

$$\int N(x, r, \vec{b}) d\vec{b} = \sigma_0 N(x, r) \tag{7}$$

is not always valid. In this approach we assumed non-trivial b-dependence and final cross section is calculated as

$$\sigma(r, x) = 2 \int d\vec{b} N(x, r, \vec{b}) \tag{8}$$

This approach makes the computation much more demanding. With maintaining same precision as in the last case, one run would take 60 hours. Following initial condition was used for the computation where $c = 10$ and $d = 1/2$:

$$N(r, b, 0) = 1 - exp[-cr^2 exp(-bd^2)] \tag{9}$$

The Balitsky-Kovchegov evolution equation in this approach reads

$$\frac{\partial N_{x_0 x_1}}{\partial Y} = \int \frac{d^2 x_2}{2\pi} K(x_{01}, x_{12}, x_{02}) [N_{x_0 x_2} + N_{x_2 x_1} - N_{x_0 x_1} - N_{x_0 x_2} N_{x_2 x_1}], \tag{10}$$

where

$$K(x_{01}, x_{12}, x_{02}) = \frac{N_c \alpha_s(x_{01}^2)}{\pi^2} \left(\frac{1}{x_{02}^2} \left(\frac{\alpha_s(x_{02}^2)}{\alpha_s(x_{12}^2)} - 1 \right) + \frac{1}{x_{12}^2} \left(\frac{\alpha_s(x_{12}^2)}{\alpha_s(x_{02}^2)} - 1 \right) + \frac{x_{01}^2}{x_{12}^2 x_{02}^2} \right). \tag{11}$$

The variables x_{ij} determine vectors between the quarks in the color dipoles as shown in Fig. 3. Running coupling is then calculated in a similar manner as in the case with neglected b-dependence. The shape of the solution differs significantly to the solution obtained without the impact parameter dependence. It would be optimal to obtain a geometrically scaled initial condition for the b-dependent case as in the previous section. The shape of the solution for two choices of impact parameter is shown in Fig. 4.

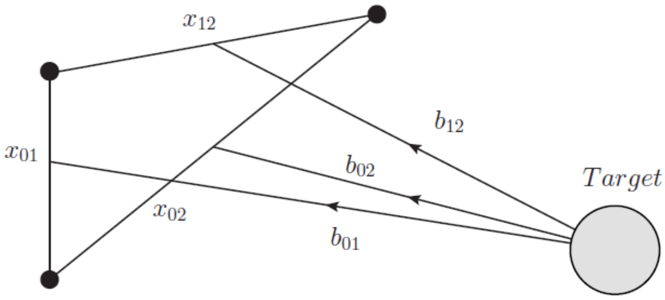

Figure 3: The color dipole triangle shows variables that are used in the BK equation [6].

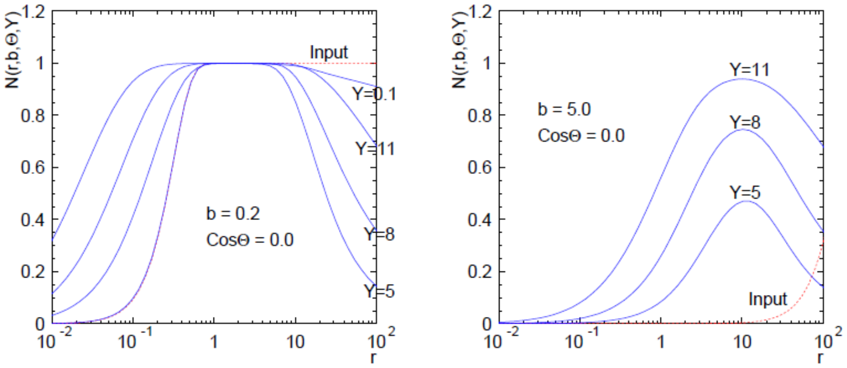

Figure 4: Solution to the rcBK equation with the b-dependence [8].

5 Conclusion

The optimal parameter setup for the rcBK equation computation has in our case proven to be:

- 25 steps per one order of magnitude of r,
- 10 steps in θ over the interval $[0; \pi]$,
- Runge-Kutta method of fourth order,

- A step of 0.01 in rapidity for the Runge-Kutta method.

We used the optimized rcBK computation to test the effect of geometrical scaling. To compute the "eigen initial condition" that would result in reducing the number of free parameters that need to be fitted from the data. MV initial condition was used and propagated to rapidity $Y = 100$, then it was re-scaled according to $Q_s^2 = 0.075$ where $Q_s = 1/r_0$ and $N(r_o) = 0.5$. A non-constant dependence of σ_0 on Q^2 was observed that needs further theoretical or phenomenological explanation.

rcBK equation with non-trivial b-dependence was also studied, since the introduction of impact parameter into the computation changes the resulting scattering amplitude significantly. Physical meaning of such results can then be used for better understanding of QCD processes. A combination of both phenomena (geometrical scaling and b-dependence) will be studied further and is beyond the scope of this paper.

References

[1] Javier L. Albacete, Nestor Armesto, Jose Guilherme Milhano, Paloma Quiroga-Arias, and Carlos A. Salgado. AAMQS: A non-linear QCD analysis of new HERA data at small-x including heavy quarks. *Eur. Phys. J.*, C71:1705, 2011.

[2] Javier L. Albacete, Nestor Armesto, Jose Guilherme Milhano, and Carlos A. Salgado. Non-linear QCD meets data: A Global analysis of lepton-proton scattering with running coupling BK evolution. *Phys. Rev.*, D80:034031, 2009.

[3] Javier L. Albacete and Yuri V. Kovchegov. Solving high energy evolution equation including running coupling corrections. *Phys. Rev.*, D75:125021, 2007.

[4] Javier L. Albacete and Cyrille Marquet. Gluon saturation and initial conditions for relativistic heavy ion collisions. *Prog. Part. Nucl. Phys.*, 76:1–42, 2014.

[5] Ian Balitsky. Quark contribution to the small-x evolution of color dipole. *Phys. Rev.*, D75:014001, 2007.

[6] Jeffrey Berger and Anna M. Stasto. Small x nonlinear evolution with impact parameter and the structure function data. *Phys. Rev.*, D84:094022, 2011.

[7] Jan Cepila and Jesús Guillermo Contreras. Rapidity dependence of saturation in inclusive HERA data with the rcBK equation. 2015.

[8] Krzysztof J. Golec-Biernat and A. M. Stasto. On solutions of the Balitsky-Kovchegov equation with impact parameter. *Nucl. Phys.*, B668:345–363, 2003.

[9] Yuri V. Kovchegov and Heribert Weigert. Triumvirate of Running Couplings in Small-x Evolution. *Nucl. Phys.*, A784:188–226, 2007.

Heavy Ion Physics at the ATLAS experiment

Oliver Matonoha*(oliver.matonoha@centrum.cz)*

Heavy Ion Physics (HIP) is a field of particle physics studying collisions of heavy atomic nuclei at high energies. One of the key motivations for this is the possible creation of quark-gluon plasma (QGP) and its further analysis. QGP is a very unusual form of matter, predicted by the theory of strong interaction (QCD) to exist under extreme conditions. In such, the normally bound quarks and gluons gain asymptotic freedom and can exist and travel unbound - similarly to electrons in traditional plasma. Hence, a hadron gas undergoes a phase transition into QGP. It is also hypothesised to form the universe in its earlier states. By researching the rules of QGP creation and its behaviour, one can learn about why was the universe created in the manner it was. Other, none the less important, motivations to study HIP are to understand the phenomenon of colour confinement and the creation of hadrons along with the potential asymmetries therein.

Pivotal research facilities studying HIP are located at CERN's LHC and BNL's RHIC colliders. At RHIC, various heavy ions (mostly of gold and uranium) collide, at the collision energy of up to $\sqrt{s_{\mathrm{NN}}} = 200$ GeV. RHIC's promiment experiments are STAR and PHENIX. They were the first to announce the possible discovery of QGP. At LHC, lead ions are collided with max. $\sqrt{s_{\mathrm{NN}}} = 2.76$ TeV and ALICE is the experiment focused on HIP. However, thanks to their respective strengths in certain areas, HIP programmes also exist within ATLAS, CMS and LHCb. At both accelerators, collisions of protons and ions are also studied.

With its cavern having the size of half of the Notre-Dame Cathedral and its construction weighing more than 7000 tons, ATLAS is CERN's biggest experimental facility. It is a multi-purpose experiment, nevertheless, its main objective was to discover the Higgs boson (which it was successful at in 2013). This is reflected in the experiment's design; its most notable features are the large muon chambers covering almost entire pseudorapidity region. Apart from that, it utilizes highly-granular inner tracker (PD, SCT, TRT) as well as electromagnetic and hadronic calorimeters. It is subjected to the magnetic field of strength 2 T. Unlike the STAR or the ALICE experiments, ATLAS lacks the Time Projection Chamber. However, it is better suited for muon measurements.

Within the ATLAS workgroup, HIP group is among the smallest ones. The dominant ones focus on studying the Standard Model, b-physics, top-physics, and Higgs boson. Nonetheless, the HIP group has come up with some valuable results, mainly in the fields of jet studies (jet quenching, jet fragmentation), production of W,Z bosons, and quarkonia production. Noticeably, ATLAS' muon measurement capabilities are utilized in these.

To elaborate on the last, quarkonia are the bound states of a quark and its antiquark. When talking about heavy quarkonia, one has in mind the quarkonia of c quark (charmonia) or b quark (bottomonia) and their respective excited states. These are: J/ψ, χ_c, ψ' (charmonia); and Υ, χ'_b, Υ', χ'_b, Υ'' (bottomonia). Heavy quarkonia have significant dileptonic decay, which makes some of them well reconstructible through the muons measuring. Since heavy quarkonia are created only in the initial stages of the collision (unlike lighter particles), any change in yields thereof in A+A collision with respect to p+p collision can deliver substantial information about the medium created in it, i.e. the QGP. This change is often quantified by means of nuclear modification factor R_{AA}, which in its simplest form is defined as follows:

$$R_{\mathrm{AA}}(Q\bar{Q}) = \frac{N_{\mathrm{AA}}(Q\bar{Q})}{N_{\mathrm{coll}}N_{\mathrm{pp}}(Q\bar{Q})} \tag{1}$$

where N_{AA} and N_{pp} are the yields of the quarkonium in A+A and p+p collision respectively, and N_{coll} is the number of participant nucleons collisions. Alternatively, it is calculated by the use of cross sections [1].

One of the causes of the suppression of quarkonia production is attributed to the screening effect. Due to the dense presence of colour charge carriers, the distance at which two quarks can 'see' each other decreases. This distance is denoted as Debye screening radius r_{D}. Effectively, if r_{D} gets smaller than the radius of a quarkonium $r_{\mathrm{Q\bar{Q}}}$, the bond can no longer exist and the quarkonium *melts*. Since r_{D} is inversely proportional to medium's temperature and the quarkonia (and the excited states) vary in size, one can use the $R_{\mathrm{AA}}(Q\bar{Q})$ to determine QGP's temperature. However, one needs to proceed carefully with this interpretation method, for there are other phenomena affecting the production, some of which are enhancing. Nuclear shadowing, Cronin effect, nuclear absorption and gluon radiation are collectively called cold nuclear matter (CNM) effects and occur even when QGP is not expected to be created, i.e. in p+A collisions. Other effects include: statistical regeneration (recombination), leakage, Landau damping, gluodissociation. [2]

For the analysis done as part of my bachelor thesis, I plan to study the Υ quarkonium suppression, using the data acquired from ATLAS. One studies this using the muon measurement, which should make ATLAS a perfectly viable source of data for this analysis. This, however, remains to be determined, as there have been no results published by ATLAS on the topic to this date. There are many incentives for focusing on Υ, instead of J/ψ. The bottomonia are more stable, less prone to recombination, and are generally deemed a cleaner probe of QGP. The disadvantage is the less generous yield per collision, hence more difficult analysis. A clean example of the Upsilon's excited states suppression in A+A collision is well depicted in the Fig. 1, brought by the CMS group. I intend to reach a similar, if not better, result in my thesis. Graphs delivered by ALICE or STAR do not reach CMS's precision in this regard, as is also displayed in Fig. 1.

References

[1] Cheuk-Yin Wong. *Introduction to high-energy heavy-ion collisions.* World Scientific, Singapore River Edge, NJ, 1994.

[2] Ramona Vogt. *Ultrarelativistic heavy-ion collisions.* Elsevier, Oxford, 2007.

[3] CMS Collaboration. Suppression of non-prompt j/psi, prompt j/psi, and y(1s) in pbpb collisions at sqrt(snn) = 2.76 tev. Available at `http://arxiv.org/abs/1201.5069v2`.

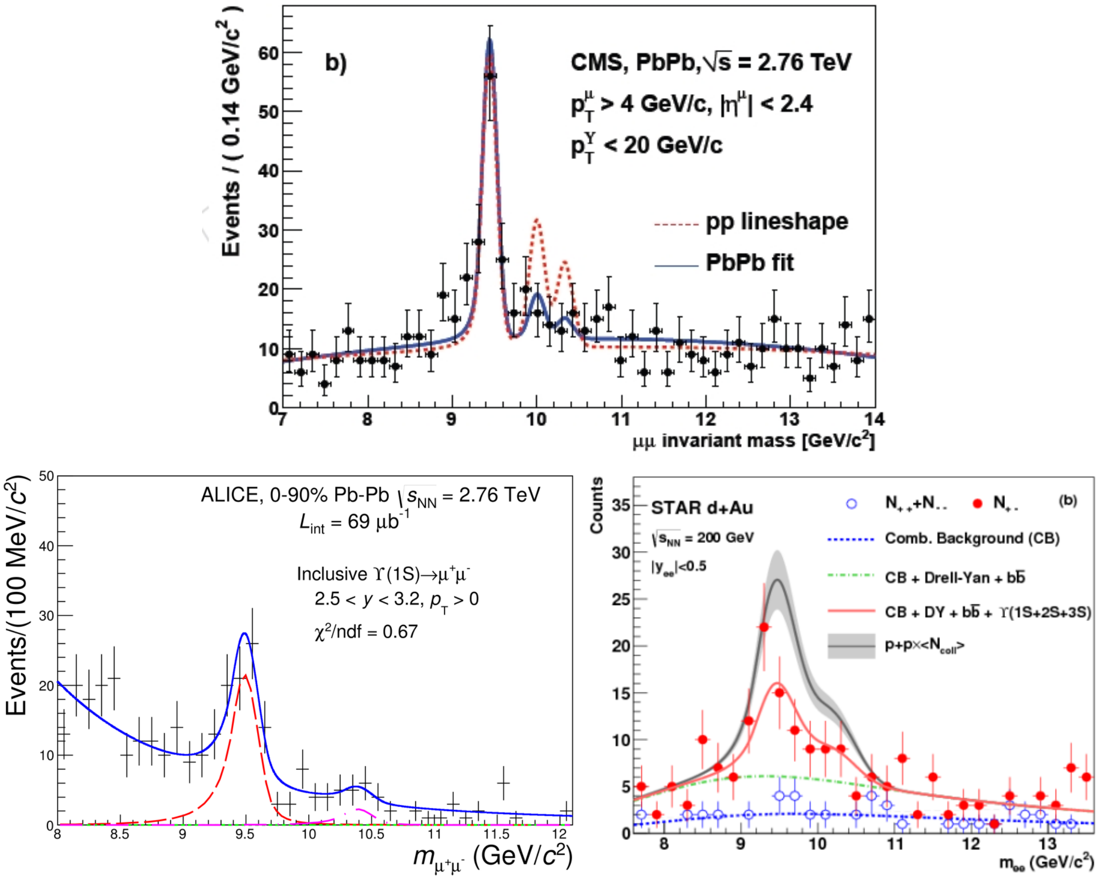

Figure 1: Dimuon invariant mass distribution, done by (a) CMS, (b) ALICE, (c) STAR. Yields in p+p and A+A collisions are shown [3] [4] [5].

[4] ALICE Collaboration. Suppression of upsilon(1s) at forward rapidity in pb-pb collisions at $\sqrt{s_{\rm NN}} = 2.76$ tev. Available at `http://arxiv.org/abs/1405.4493v3`.

[5] STAR Collaboration. Suppression of upsilon production in d+au and au+au collisions at $\sqrt{s_{\rm NN}} = 200$ gev. Available at `http://arxiv.org/abs/1312.3675v3`.

Jet substructure

Katerina Moudra*(katerina.moudra@cern.ch)*

The study of jet substructure is important to a variety of analyses, particularly involving highly boosted massive objects such as top quarks or vector bosons. With increasing center-of -mass energy, boosted kinematics becomes more and more important. The more massive decaying particle is, the more boosted are the decay products. This leads to necessity to use boosted final states in analyses, where massive particles are being searched. For example, dark matter is being searched in associated production with a vector boson in hadronic channel, where the hadrons are boosted into a single jet.

Several variables have been devised to isolate jets with different internal topologies. Different analyses prefer different variables. One of these is the calibrated jet mass, M_j, taken as the invariant mass from the four-momenta of all of the jets constituents. Another parameter is useful in boosted top identification, the N-subjettiness ratio t_{32}, which indicates the preference of the jet topology for a 3-component vs. 2-component structure. For boson identification there is an analogous ratio being used, t_{12}. The 2-component substructure can be recognized also with help of the energy correlation ratio, $D2$. Detailed description of all these variables can be found in [1].

In the ATLAS detector, jets are reconstructed mainly in electromagnetic and hadronic calorimeters. Jet reconstruction is affected by various apparatus effects. One of those effects is pile-up. Pile-up is the term given to the extra signal produced in the detector in addition to the expected signal from the hard-scattering process. There are two types of pile-up :

1. In-time pile-up is due to the interactions happening in the same bunch crossing in addition to the hard-scattering interaction of interest. It is well quantified by the number of reconstructed primary vertices in the event.

2. Out-of-time pile-up is due to the preceding and subsequent bunch crossings, the signal of which effects the response of the detector as integration times in the calorimeter span multiple bunch crossings.

The average number of interactions per bunch crossing (measured over a luminosity block), $< \mu >$, is used to parameterise the pile-up.

The sensitivity of some jet based physics analyses is dependent on an effective resolution of jet substructure variables. These performance characteristics of reconstructed quantities exhibit significant dependence on pile-up conditions present in ATLAS operation.

In order to remedy the pile-up dependence, pile-up noise cleaning is applied to the jet constituent at topocluster cell level. Such pile-up noise cleaning technique is parametrized by topocluster noise threshold, $< \mu_{threshold} >$, which is tuned to the presumed $< \mu >$.

Since all jet quantities have topoclusters as their rudimentary constituent, studies necessary must focus on the proper choice of topocluster reconstruction parameters to ensure optimal performance. It is therefore important to investigate these parameters in terms of their pile-up dependence. The MC15 *mu-scan* studies will test the tuning of noise thresholds in the topocluster reconstruction. Currently, ATLAS is using the same threshold as in 2012, $< \mu_{threshold} >= 30$, since the expected $< \mu >$ was around 20 in 2015 (very similar to 2012).

In 2016 we may see $< \mu >$ up to 50, so we need to increase the thresholds (for instance, to be able to run the HLT with the desired rate). In order to study the impact of higher thresholds we used MC samples with $< \mu >= 40, 50$ and $< \mu_{threshold} >= 30, 40, 50, 60, 70$ for various final states: dijets, Z$'$ $\rightarrow t\bar{t}$, and W$'$ $\rightarrow$ WZ, where the later two consist of solely hadronic decays of top, W' and Z'. The preliminary result is, that all jet substructure variables depend slightly on $< \mu >$, dependence on $< \mu_{threshold} >$ is negligible. More detailed studies are yet to come.

References

[1] Dasgupta, Mrinal and Fregoso, Alessandro and Marzani, Simone and Salam, Gavin P., JHEP (2013)

Exclusive dilepton production in *pp* collision at 13 TeV

Filip Nechanský *(nechafil@fjfi.cvut.cz)*

An ultra-relativistic proton has a deformed electromagnetic field due to the relativistic contraction. The transverse component of such field can be interpreted as a quasi-real photon - a photon with low value of virtuality $Q^2 = -P_\gamma^2$, where P_γ is four momentum of the photon. On experiments as is the ATLAS at the LHC, a collision of such photons can be studied.

Between the great number of final states of such collision, one particular process resulting in dilepton pair was studied. Feynman diagram of this process is in the Figure 1. Production of the dilepton pair can be used for luminosity measurements, since it contains only two particles in the final state and is therefore easily identifiable. Situation is of course more complicated than that and theoretical cross-section is reduced due to additional interactions between the colliding protons. The difference between the theoretical σ^{theory} and measured cross-section σ^{meas} is quantized by so-called survival factor R :

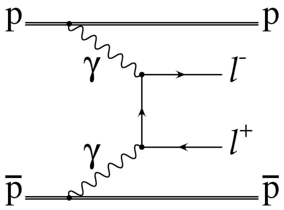

Figure 1: Feynman Diagram of exclusive di-lepton production in proton-proton collision. Taken from [1].

$$\sigma^{meas} = R \cdot \sigma^{theory} \tag{1}$$

The interaction of the quasi-real photons is characteristic by low transverse momentum of the dilepton state. The leptons are therefore back-to-back, which is another factor useful for background subtraction.

The main background to the dilepton production is Drell-Yan process (see Figure 2), which is an interaction between quarks of the colliding protons. Since one of the propagators of this process can be the Z quarks, Drell-Yan is dominated by a resonance around the mass of the Z boson (approximately 90 GeV). Even though Drell-Yan makes up the majority of the final states containing dilepton, it is usually accompanied by a large number of additional particles and has different kinematic properties than the exclusive production and thus its contribution is significantly reduced by carefuly chosen cuts. Second most significant background is dissociation.

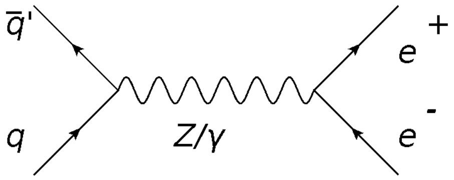

Figure 2: Feynman Diagram of Drell-Yan process. Taken from [2].

Single- and double-dissociation (SD,DD) is process where either one or both colliding protons dissociate - break into variety of final states, most of which have large rapidity. Since the ATLAS detector does not detect all outgoing particles (mainly in the forward rapidity regions), such events are often indistinguishable from the exclusive production. Mainly the SD contribution is significant even after all cuts and is subtracted using a fit of the exclusive and the single-dissociative distributions on the data.

Since the ATLAS has large number of collisions per bunch crossing, we cannot simply look for events with only two leptons and nothing else. Exclusive events can however be identified by requesting only two particles in proximity of the dilepton vertex (this selection is called exclusivity cut). Furthermore, the contribution of the Drell-Yan can be significantly reduced by removing events in the mass window around the Z-mass peak.

Finally, since the leptons are back-to-back and the dilepton system has low transversal momentum, it is useful to cut either on the angle between the two leptons (acoplanarity) or on the p_T of the dilepton. Spectrum of the dilepton pairs as function of acoplanarity and p_T from previous analysis can be found in Figure 3. This analysis was done for energy $\sqrt{s} = 7$ in both the ATLAS and CMS at the LHC. The results are summarized in Figure 4. The survival factor R was found to be around 80%.

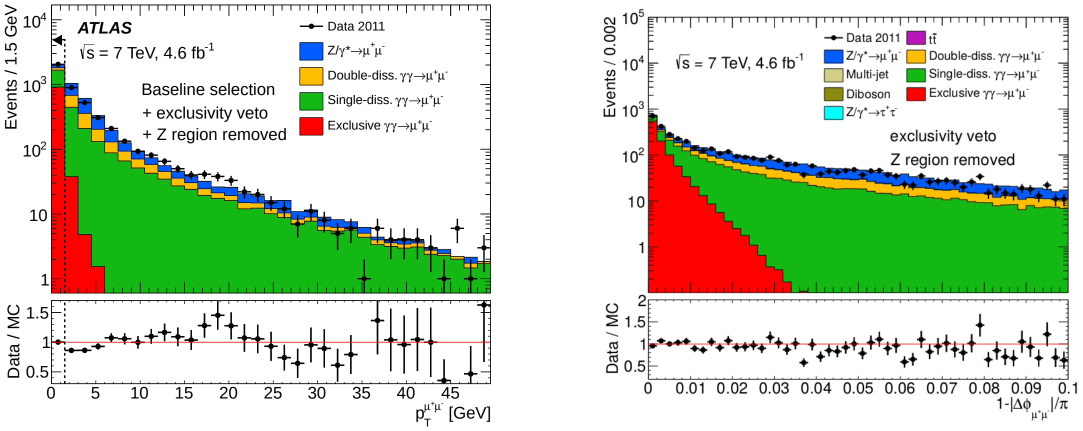

(a) (b)

Figure 3: Results of exclusive dilepton analysis at 7 TeV with the ATLAS and CMS experiments. Taken from [3].

The $\sqrt{s} = 13$ TeV analysis is already in progress. Aside from producing result for the new energy, examination of dependence of the survival factor on various variables (e.g. $m_{l^+l^-}, p_{T,l^+l^-}$) is planned. Current focus is on the Monte Carlo production and preliminary examination of the data from 13 TeV.

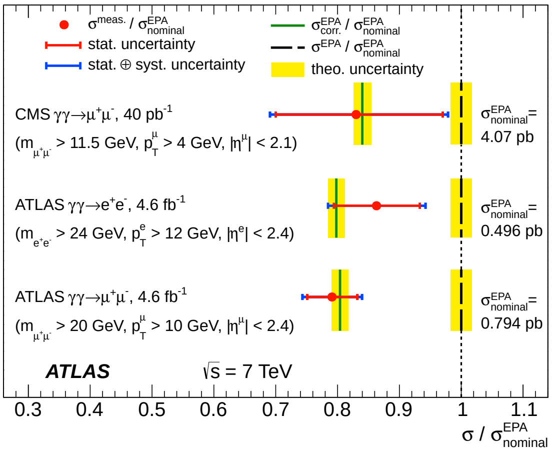

Figure 4: Results of exclusive dilepton analysis at 7 TeV with the ATLAS and CMS experiments. Taken from [3].

For some period of the 2015 LHC run, a low-p_T muon trigger was used. This allows us to do the analysis for lower transverse momentum of the muon. Preliminary results show circa 13% more selected events if the low-p_T muon trigger is implemented. Otherwise situation is similar to 7 TeV and it seems it will not be necessary to make significant adjustments to the cuts.

References

[1] Michael Albrow and Emily Nurse, A search for exclusive Z→ll events and a measurement of the $pp \to p\gamma\gamma p \to pllp$ cross section for dilepton invariant mass > 40 GeV/c^2, http://www-cdf.fnal.gov/physics/new/qcd/exclZ_08/exclusive/

[Cited on 22. 2. 2016]

[2] nxhlh.com, Collision symmetry and measuring the asymmetry in the Drell-Yan process, http://www.nxhlh.com/collision-symmetry-and-measuring-the-asymmetry-in-the-drell-yan-process/

[Cited on 22. 2. 2016]

[3] Measurement of exclusive $\gamma\gamma \to l^+l^-$ production in proton-proton collisions at $\sqrt{s}$=7 TeV with the ATLAS detector, Phys.Lett. B749 (2015) 242-261

Study of B_s meson properties at ATLAS

Zbyněk Nguyen *(zbynek.nguyen@fjfi.cvut.cz)*

1 Introduction

In the field of high-energy physics, the so-called B–physics is known as the study concerning b quarks and their composite particles, referred to as B mesons. These are particularly interesting for a variety of reasons. Namely, for the quark mixing and its role in CP violation, or for measurements of production cross-sections of heavy-flavor quarkonia. Last but not least, several massive particles decay into b quarks, e.g. top quarks and the Higgs.

In particular, the B_s meson is a bound state of a bottom antiquark and a strange quark. Thanks to flavour-changing weak decays of the constituent quarks, the B_s meson is able to spontaneously transform into its own antiparticle $\bar{B}_s$. Physical properties of these particles and the nature of their mixing might shed some light on the discrepancy between matter and antimatter in the observable universe, which is of interest in cosmology.

The ATLAS at the LHC is one of the two experiments studying B meson decays, the other one being the LHCb. This work-in-progress study is using ATLAS 2012 data from pp collisions at $\sqrt{s} = 8$ TeV and integrated luminosity 14.3 fb^{-1}. From these data, the properties of the B_s meson are extracted using the unbinned maximum likelihood fit.

2 Analysis

The aim of this study will be to perform the full CP violation analysis, as described in ATLAS article [2]. As of today, only the simultaneous mass and lifetime fit was performed. The main building block for the fit is the likelihood function which is composed from probability density functions (pdf for short).

The lifetime of the candidate for the B_s meson is the proper decay time, defined as the projection of the transverse decay length onto the transverse momentum, multiplied by PDG average B_s meson mass [3].

The utilized ATLAS data contain mass and lifetime points m_i and τ_i, each with their corresponding uncertainties σ_{m_i} and σ_{τ_i} given by the decay vertex reconstruction. These data points were fitted as-is, without being binned into histograms, hence the term unbinned fit. The maximization of the likelihood function yields the parameters that are sought – the average mass and lifetime of the B_s meson.

The likelihood function L was based on the [1], taking the form of

$$L = \prod \{ f \cdot M_{\text{sig}} T_{\text{sig}} + (1-f) \cdot M_{\text{bkg}} T_{\text{bkg}} \}, \tag{1}$$

where the product runs over all events, f denotes the fraction of the signal candidates, M_{sig} and M_{bkg} the mass pdfs for the signal and background, and analogously T_{sig} and T_{bkg} the time pdfs.

The mass signal $M_{\text{sig}}(m_i|\sigma_{m_i})$ consists of a per-candidate gaussian (i.e. each mass point m_i has a different variance given by σ_{m_i}), the mass background M_{bkg} is an exponential function, shifted along the y-axis.

The time signal $T_{\text{sig}}(\tau_i|\sigma_{\tau_i})$ for each lifetime point τ_i and its uncertainty σ_{τ_i} is modeled as a convolution

$$T_{\text{sig}}(\tau_i|\sigma_{\tau_i}) = \left[\frac{1}{\tau(B_s)}\exp\left(-\frac{\tau}{\tau(B_s)}\right)\right] \otimes R(\tau - \tau_i, \sigma_{\tau_i}). \tag{2}$$

where the the first term is the exponential decay function (defined for $\tau > 0$) and the second is the time resolution function defined simply as a gaussian centered at zero.

The time background pdf contains two components, the first one being the B_s candidates from the prompt J/ψ, whereas the second from the non-prompt J/ψ. The prompt component is

$$T_p(\tau_i|\sigma_{\tau_i}) = \left[p\delta(\tau) + \frac{1-p}{2\tau_3}\exp\left(-\frac{|\tau|}{\tau_3}\right)\right] \otimes R(\tau - \tau_i, \sigma_{\tau_i}), \tag{3}$$

note that it is symmetric with respect to the y-axis due to the Dirac delta function $\delta(\tau)$ and absolute value $|\tau|$ both being even functions. The parameter p then yields the fraction between the two functions. The non-prompt component is

$$T_{np}(\tau_i|\sigma_{\tau_i}) = \left[\frac{n}{\tau_1}\exp\left(-\frac{\tau}{\tau_1}\right) + \frac{1-n}{\tau_2}\exp\left(-\frac{\tau}{\tau_2}\right)\right] \otimes R(\tau - \tau_i, \sigma_{\tau_i}), \tag{4}$$

consisting of a faster and slower decays with decay times τ_1 and τ_2, and n being the fraction between the two functions. Finally, these time background pdfs are combined using $T_{\text{bkg}} = t_{bkg}T_p + (1 - t_{bkg})T_{np}$, concluding the description of the likelihood function.

3 Results

These preliminary studies of B_s meson properties showed good agreement with result from the ATLAS articles [1, the first observance of B_s mesons at ATLAS] and [2, the latest article about B_s meson CP violation at ATLAS] as well as the PDG values [3]. So far, no occurence of new physics can be reported.

Quantitatively, no values can be given here as they are not published yet. Nonetheless, more thorough analysis is to be performed.

References

[1] The ATLAS Collaboration. Observation of the B_d^0 and B_s^0 mesons in the decays $B_d^0 \to J\psi K^{*0}$ and $B_s^0 \to J\psi\phi$ (2011), ATLAS-CONF-2011-092.

[2] The ATLAS Collaboration. Measurement of the CP–violating phase ϕ_s and the B_s^0 meson decay width difference with $B_s \to J/\psi\phi$ decays in ATLAS (2016), arXiv:1601.03297 [hep-ex].

[3] K.A. OLIVE et al. (Particle Data Group), Chin. Phys. **C 38**, 090001 (2014).

Characteristics of cosmic ray showers with respect to type of primary particles

Šimon Novák*(novaksi1@fjfi.cvut.cz)*

Earth's atmosphere is being constantly bombarded by cosmic rays of various energies arriving isotropically from the universe. The flux of incoming particles is decreasing sharply with rising energy, hence a particle with energy 10^{11} eV hits every square meter once per second, whereas one with energy 10^{18} eV will hit it only once per year. Primary cosmic rays are mainly composed of charged nuclei such as that of hydrogen, helium or iron, nevertheless electrons, photons and neutrinos can also be found.

Upon reaching the atmosphere, the energy of primary particle is consecutively released via collisions with air molecules producing secondary particle showers - mainly negative pions, immediately decaying into gamma pairs, forming an electromagnetic (soft) component of the shower. Also charged pions, subsequently decaying into mion - neutrino pairs, can be found. Mions thus produced represent a hard component of the shower, reaching up to the Earth's ground. Third and final is hadronic component formed by newly-emerged neutrons, protons, kaons and pions. All three components repetitevely collide with air molecules resulting into cascade-type shower propagation.

The Pierre Auger Observatory is the world's largest cosmic ray observatory. On area exceeding 3000 square kilometres an array of 1660 water Cherenkov particle detector stations is spread. In addition, the site is overlooked by 24 air fluorescence telescopes. The observatory hybrid design allows one to study properties of cosmic rays with energies above 10^{17} eV both by measuring the fluorescence light emitted by excitated nitrogen molecules as the shower propagates itself through the atmosphere and by detecting the Cherenkov photons emitted by charged shower particles in water Cherenkov tanks.

One of the most important measurable characteristics of an extensive air shower is atmospheric depth of its maximum or X_{max} $[g/cm^2]$. At this depth the energy deposition in the atmosphere is maximal. According to a superposition model, X_{max} is proportional to the logarithm of the primary particle energy:

$$X_{max} \sim \lambda_e \ln\left(\frac{E_0}{A}\right), \tag{1}$$

where λ_e is an elongation rate and A is the mass number of the primary particle. It is clear from (1) that X_{max} of showers induced by heavier primary particles is smaller than that of lighter particles with the same energy.

Some of the previous results by Pierre Auger Collaboration depicted in Figure 1 are indicating that with increasing energy of the most extensive air showers the amount of heavier primary particles such as iron nuclei rises. Further study of the composition of the particles inducing extensive air showers is required to understand the origin of the most energetic particles ever detected.

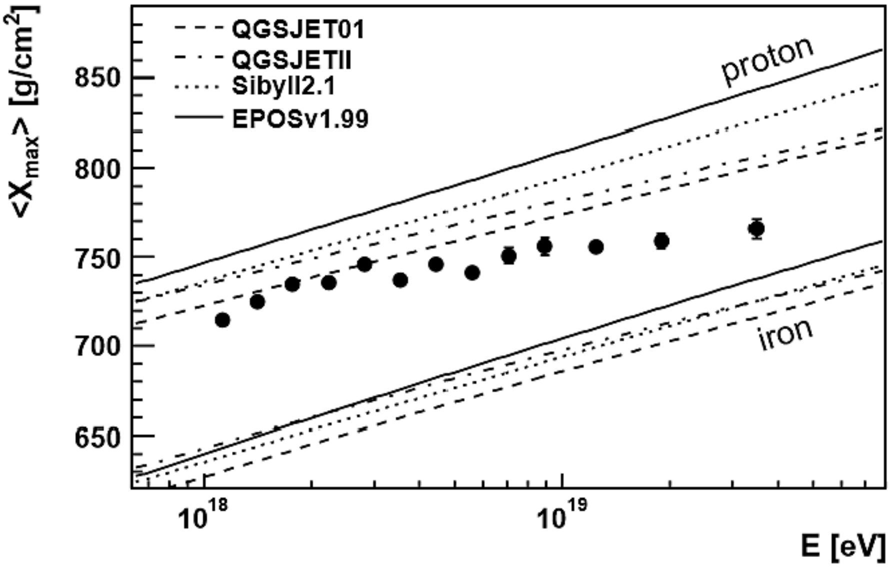

Figure 1: Measured mean value of X_{max} of extensive air showers by the Pierre Auger Observatory, [3]

References

[1] GRUPEN, Claus, *Astroparticle Physics*, Springer, 2005

[2] The Pierre Auger Collaboration, *The Pierre Auger Cosmic Ray Observatory*, 2015

[3] The Pierre Auger Collaboration, *Measurement of the Depth of Maximum of Extensive Air Showers above* 10^{18} *eV*, 2010

Charmonia and xAOD

Lukáš Novotný *(novotl23@fjfi.cvut.cz)*

1 Charmonia

1.1 J/ψ and $\psi(2S)$ Discovery

In the first half of the last century mankind discovered, that our world is composed of electrons, protons, neutrons and later pions and other particle. By the mid-1960's, physicists realized that this understanding is insufficient to explain the big number of new particles being discovered. For this reason, Gell-Mann's [7] and Zweig's [8] theory predicted the existence of quarks d, u and s. The existence of the fourth quark, named charm (c),was predicted in 1964 by Sheldon Glashow and James Bjorken. Six years later, Sheldon Glashow, John Iliopoulos, and Luciano Maiani showed the importance of charm quark in the Zweig's quark model. The charm quark allows a theory (GIM mechanism [9]) that has flavour-conserving Z^0-mediated weak interactions but no flavour-changing ones. Finally in November 1974, Burton Richter (SLAC) and Samuel Ting (BNL) [3] announced independently the discovery of particle J/ψ, which consist of two quarks, c and $\bar{c}$, so also existence of charm quark was confirmed.

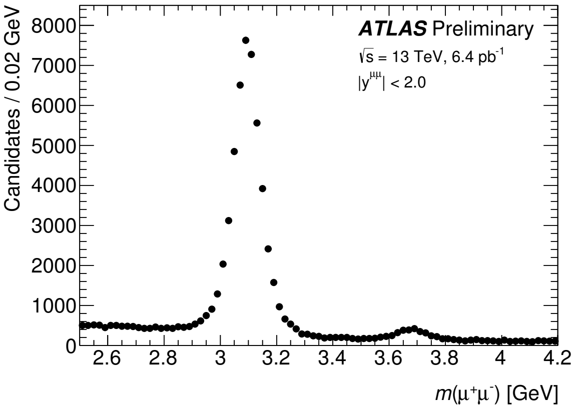

Figure 1: Invariant mass distribution of selected di-muon candidates, as seen by the ATLAS experiment in early phase of Run II. Peaks corresponding to the J/ψ and $\psi(2S)$ resonances are visible.[11]

S. Ting and collaborators in Brookhaven National Laboratory built spectrometer for a search of particle with same quantum numbers as photon and they found new particle

J in a process [1]:

$$e^{+} + e^{-} \rightarrow J + anything. \tag{1}$$

At the same time, R. Burton at SLAC (Stanford) observed also new particle ψ in a process [1]:

$$p + Be \rightarrow \psi + hadrons. \tag{2}$$

Both particles J and ψ have same mass $m \approx 3.1$ GeV, so physicists draw a conclusion that J and ψ are the same particle known nowadays with name J/ψ. Also another particle has been discovered in SLAC experiment, resonance ψ' with mass $m \approx 3.7$ GeV.

1.2 Charmonia Spectrum

Particle $J/\psi = \psi(1S)$ has mass $m = 3096.916 \pm 0.011$ MeV (see Figure 1)and decays into hadrons (88%), $e^{+}e^{-}$ pair (6%) or $\mu^{+}\mu^{-}$ pair (6%)[10]. J/ψ and ψ' are resonances of meson η_c and are together with other bound states of charm quark and anti charm quark called charmonia. We can see the spectrum of charmonia states in Figure 2.

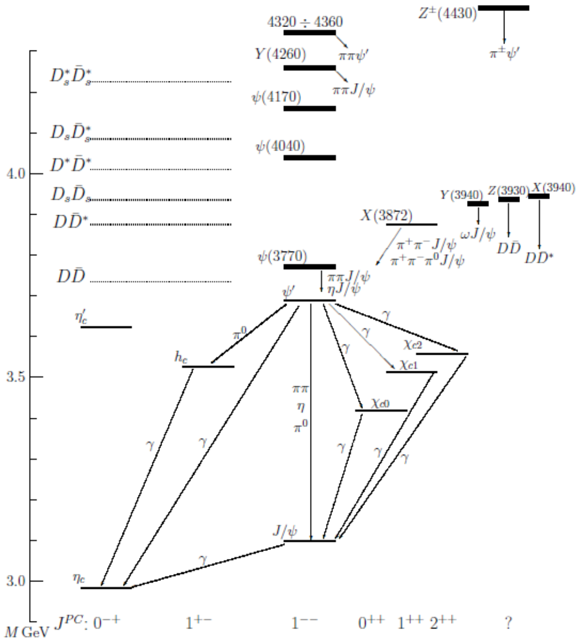

Figure 2: The energy-level diagram for charmonium.[5]

The advantage of charmonium is its similarity to positronium, so it helps us understanding strong interaction at short distance (which bounds c and $\bar{c}$ together in charmonium). The electromagnetic force can be described with Coulomb potential

$$V_{em} = -\frac{\alpha}{r}, \tag{3}$$

where r is distance between e^{+} and e^{-} and $\alpha \approx \frac{1}{137}$ is the fine structure constant. The exact potential between quark and antiquark is unknown, but can be approximated with formula [1]

$$V_{QCD} = -\frac{4}{3}\frac{\alpha_s(r)}{r} + kr, \tag{4}$$

where $\frac{4}{3}$ is a colour factor, r is the distance between quark and antiquark, $k = 1$ GeV $\cdot$ fm^{-1} is the constant and α_s is the quark-gluon coupling. It is evident that for short distances, electromagnetic and strong behave similarly.The equation (4) is only a model of the strong interaction, does not work for long distance and does not include the spin influence and the spin-orbit interaction.
Charmonia are not used only for study of the strong force, but they are useful in measuring the quark gluon plasma (QGP) temperature (because J/ψ is melting at different temperature than $\psi(2S)$), can be used for B hadron detection (it is "standard candle" to identify decays of B mesons using displaced J/Psi decay vertices) and last but not least it is widely used in detector performance studies for the measurement of the detector reconstruction efficiency and the detector resolution.

2 AOD and xAOD Data Format

During the Run I phase of the ATLAS experiment at LHC, digits representing physical detector information are obtained from detectors and were together with data from Monte Carlo simulation used for the reconstruction of event. Data after reconstruction were saved in AOD(Analysis Object Data) in the Run I. These data are not readable with ROOT, so they have to be transformed with Athena software into the format DPD (n-tuple data format), which is readable by ROOT and are more suitable for the following physics analysis. However, this has big disadvantage, because every physic group handles own "derivations" dAOD, which generally contain same information and and waste disk free space. Moreover, waiting for DPD production took months in some cases and it was difficult to compare analyses using different DPDs.
In the Run 2, data from reconstruction are saved in a new data format named xAOD[4].

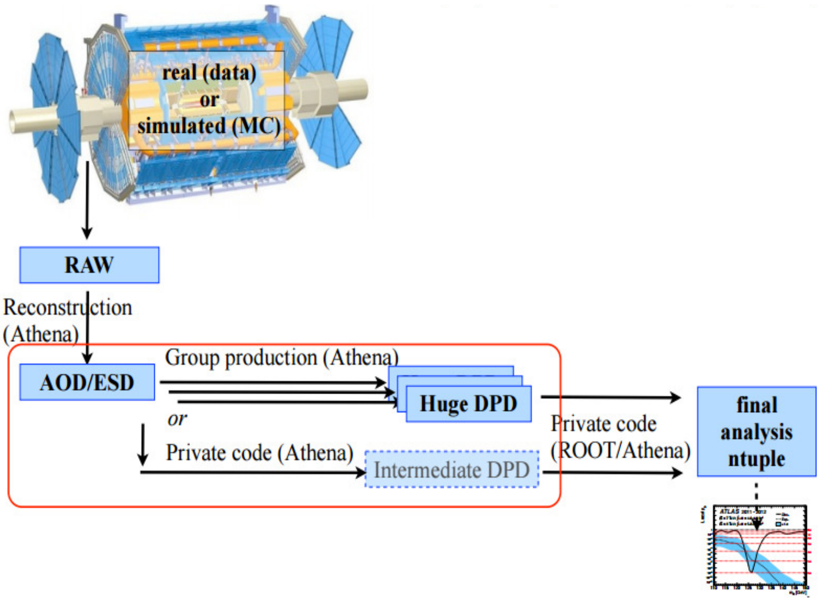

Figure 3: Run I analysis model, RAW is a persistent representation of the event data in byte-stream format, AOD is Analysis Object Data, ESD is Event Summary Data and DPD is n-tuple data format. The red rectangle is substituted by xAOD format in the Run II.[6]

As visible in the Figure 3, xAOD format substitutes AOD and DPD format, it is object oriented, so this format is readable by Athena software and also by ROOT. xAOD also uniform across all reconstructed object types (jets, muons, etc.). Derivations DxAOD are produced centrally and re-run the derivation framework is more frequently than the full reconstruction step (to produce the xAOD)[12].
The xAOD consists of information about the event (EventInfo) and information about reconstructed objects within each event (jets, muons, tracks, etc.). These reconstructed objects inherit from a common class Particle. xAOD::EventInfo is only one object of this type for given event and contains current run number, event number, what was the pile-up for given event. Information about objects of particle type (electron, muon, tau, jet, photon, . . .) is saved as class xAOD::IParticle. Here are saved mass, energy, rapidity, transverse momentum and other information about given particle.
Information in xAOD is split into the objects and the Auxiliary Store, where object data are stored as vectors of values. The splitting allows reading of variable across objects without having to going through the full event, for example it enables fast reading in ROOT with TBrowser. Usually, programmers work with object and never need to interact with Auxiliary Store.

References

[1] PERKINS, Donald. Introduction to High Energy Physics. Cambridge University Press, 2000

[2] BETTINI, Alessandro. Introduction to Elementary Particle Physics. Cambridge University Press, 2014

[3] J. J. Aubert et al., Phys. Rev. Lett. 33, 1404 (1974)

[4] Eric Lançon. Preparing ATLAS Distributed Computing for LHC Run 2, PoS(ISGC2014)045, 2014

[5] M.B. Voloshin. Charmonium. Prog.Part.Nucl.Phys., 61:455–511, 2008

[6] Louise Heelan. ATLAS Analysis Model: (How analysis should be done). Software Tutorial at CERN, 2016

[7] M. Gell-Mann, Phys. Lett. 8, 214 (1964)

[8] G. Zweig, An SU(3) Model For Strong Interaction Symmetry And Its Breaking. 2, CERN-TH-412

[9] S.L. Glashow, J. Iliopoulos and L. Maiani, Phys. Rev. D2, 1285 (1970).

[10] K.A. Olive et al. (Particle Data Group), Chin. Phys. C, 38, 090001 (2014) and 2015 update

[11] ATLAS Collaboration, ATLAS-CONF-2015-023 (2015)

[12] Attila Krasznahorkay. The xAOD Event Data Model. ATLAS Software & Computing tutorials USM/PUC, Chile (2015)

J/ψ polarization studies at ATLAS

Radek Novotný *(novotr14@fjfi.cvut.cz)*

Abstract

This contribution is devoted to the brief overview of the quarkonia studies in proton-proton collisions at $\sqrt{s} = 8\,\mathrm{TeV}$ measured by the ATLAS detector. The special attention is given to the measurement of the prompt J/ψ polarization, which is the good test of several production scenarios.

The quarkonium is bound state of a heavy quark and antiquark pair with the same flavour, and it is the simplest system bound by a combination of the strong and electromagnetic interactions. Since the binding energies of the quarkonia systems are at the edge of perturbative QCD energy scale, study of the $Q\bar{Q}$ system properties serves to improvement the understanding of the strong force. For description of heavy quarkonium production three most prominent theoretical models, Color Evaporation Model, the Color Singlet Model and Nonrelativistic QCD Factorization Model, are used. None of these theoretical models is able to describe full spectrum of the heavy quarkonium properties. One of the crucial parameter, in which all of these models differ, is polarization of the J/ψ resonance. The polarization of the J/ψ resonance can be measured through the study of the angular distribution of the leptons produced in the decay ($\mu^+\mu^-$ or e^+e^-). The general decay frame of J/ψ candidate is given by

$$\frac{\mathrm{d}N^2}{\mathrm{d}\cos\theta^*\mathrm{d}\phi^*} = \frac{3}{4\pi(3+\lambda_\theta)} \cdot (1 + \lambda_\theta \cos^2\theta^* + \lambda_\phi \sin^2\theta^* \cos\phi^* + \lambda_{\theta\phi} \sin 2\theta^* \cos\phi^*), \qquad (1)$$

where the θ^* is the angle between the direction of the positive muon in the J/ψ rest frame and the momentum of the J/ψ in the laboratory frame, while ϕ^* is defined as the angle between the dimuon production and decay planes in the laboratory frame. The coefficients λ_θ, λ_ϕ and $\lambda_{\theta\phi}$ are related to the spin density matrix elements of the dimuon spin wave function.

These measurement focus at $J/\psi \to \mu^+\mu^-$ decay channel, which have clean signature in the detector and the background is highly suppressed. The trigger used in the analysis requires at least two muons with p_T greater than $4\,\mathrm{GeV}$. The first step is to separate the prompt and non-prompt component of the J/ψ contribution. For that purpose, the unbinned maximum likelihood fit in invariant mass and pseudo proper-lifetime variables is performed. For the description of the both prompt and non-prompt signal in invariant mass frame the CrystallBall distribution was used. In the pseudo-proper time frame is used the dirac function convolved with the resolution function for prompt and one-sided exponential convolved with the same resolution function for non-prompt. The resolution function is described with the gaussian distribution and is the same for all of the pseudo-proper time distributions. The background is composed of three components. The prompt component of background is described by the linear function in invariant mass frame and dirac function convolved with the resolution function in pseudo-proper time frame. The non-prompt components of the background are two. The first one is exponential for invariant mass frame and single sided exponential convolved with the resolution function in pseudo-proper time frame. The second one is exponential for invariant mass frame and flipped single sided exponential convolved with the resolution function in pseudo-proper time frame. The negative part of the background is connected with miss match during reconstruction and combinatoric background.

Using the fit parameters, the dataset is divided to the signal region, primary consist of the prompt J/ψ, and background region with minimum prompt J/ψ. In both these regions, the polarization template fit is performed, thus we are able to subtract the polarization of the background from the signal.

The most important part of the analysis ahead of us, is to implement several detector effects and systematic uncertainties and verify the fitting procedure at Monte Carlo simulations with zero polarization.

References

[1] Measurement of the prompt and polarizations in pp collisions at. *Physics Letters B*, 727(4–5):381 – 402, 2013.

[2] R Aaij et al. Measurement of J/ψ polarization in pp collisions at $\sqrt{s} = 7$ TeV. *Eur. Phys. J.*, C73(11):2631, 2013.

[3] Yonathan Munwes and Erez Etzion. *J/ψ spin-alignment measurement in pp collisions at $\sqrt{s} = 8$ TeV with the ATLAS detector at the LHC.* PhD thesis, Tel Aviv U., Jan 2014. Presented 27 Jul 2014.

[4] Georges Aad et al. Measurement of the differential cross-sections of prompt and non-prompt production of J/ψ and $\psi(2S)$ in pp collisions at $\sqrt{s} = 7$ and 8 TeV with the ATLAS detector. 2015.

Neutral strange particle production in charged jets measured with ALICE

Vojtěch Pacík *(pacikvoj@fjfi.cvut.cz)*

Theory of Quantum Chromodynamics (QCD) predicts a phase transition of hadronic matter at high temperatures and high energy densities. Under such extreme conditions quarks and gluons are no longer confined inside hadrons and form a state called "quark-gluon plasma" (QGP). It is believed that this form of matter existed in the early stage of the evolution of the Universe. According to experimental results, it seems that this state can be recreated in ultra-relativistic heavy-ion collisions. Study of QGP properties may improve our knowledge of QCD.

One of the ways of studying this new state of the hadronic matter is via the partons (quarks and gluons) with high p_{T}, which are produced in the very early stages of the collision. These hard probes fragment into the softer ones leading to a cascade of partons which subsequently hadronise. Since the partons themselves cannot be experimentally detected, the study of such collimated sprays of particles, called jets, coming from initially hard partons is often performed instead.

Transverse momentum (p_{T}) spectra of identified hadrons and their ratios provide a unique tool to study the possible effects of the QGP [1]. It was first observed at RHIC at Brookhaven National Laboratory [2, 3], that the baryon-to-meson ratio is enhanced in central heavy-ion collisions in comparison with the peripheral or proton-proton (pp) collisions. This enhancement has been observed not only in light flavour hadrons, such as protons and pions (containing only u and d quarks), but also in case of the inclusive strange particles, Λ and $\mathrm{K}^0_{\mathrm{S}}$ (see Figure 1). Similar analysis has been done by experiments at the Super Proton Synchrotron (SPS) and later at the Large Hadron Collider (LHC) [4] at CERN both in pp and heavy-ion collisions.

This so-called "baryon anomaly" phenomenon is still not fully understood, although various models have been proposed, namely parton fragmentation and hadronisation modification, parton recombination and radial flow [5]. A detailed investigation of the origin of this phenomenon is currently ongoing at A Large Ion Collider Experiment (ALICE), one of the four main experiments at the LHC.

The main motivation of study of neutral strange particles production in the charged jets[1] is to understand the origin of discussed enhancement of $\Lambda/\overline{\Lambda}$ baryons with respect to the $\mathrm{K}^0_{\mathrm{S}}$ mesons and distinguish between the possible effects of hot and dense strongly interacting medium and other discussed mechanism (in general soft and hard processes) by

---

[1] Charged jets refers to the jets reconstructed only from detected charged particles.

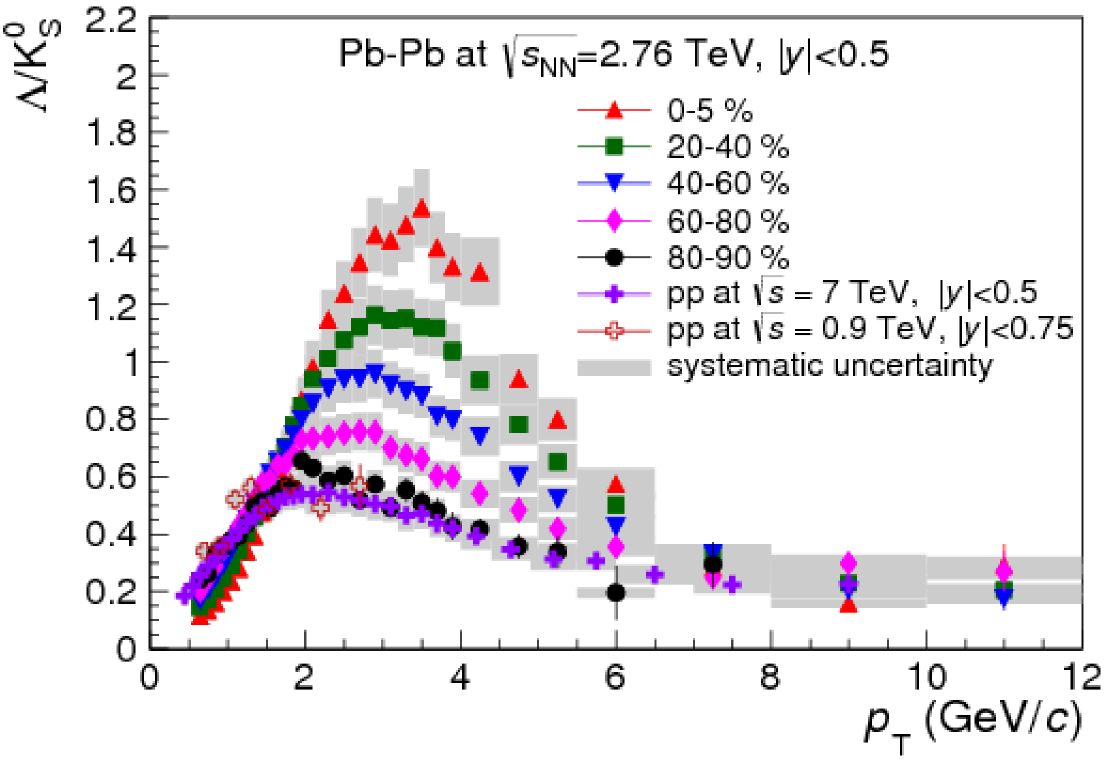

Figure 1: Ratio of inclusive production of neutral strange Λ baryons and K^0_S mesons [4] illustrating the so-called baryon anomaly, the enhancement of baryon production with respect to the meson production in Pb-Pb relative to the pp collisions.

comparing the identified hadrons inside the jet cones with the inclusive hadrons produced by the thermalized bulk. Additional aspect of such analysis in the pp collisions is providing a suitable reference for Pb-Pb and p-Pb system, since information from all collisional systems is necessary for proper understanding of this phenomenon.

In order to reconstruct the neutral strange hadrons, K^0_S and Λ (containing one s quark), a special hadronic decay channel has been chosen. In this channel, electrically neutral mother particle decays into a pair of daughter particles, one with positive and the other with negative electric charge. Namely $K^0_S \to \pi^+ + \pi^-$ and $\Lambda \to p + \pi^-$. Due to this typical "V-shaped" topology, the mother particles are referred to as V^0 particles. The reconstructed V^0 particles are obtained from the fitting of invariant mass distribution of candidates fulfilling applied topological cuts and quality requirements used in order to suppress as much of the combinatorial background as possible. The p_T spectra are then corrected for reconstruction efficiency as well as detector acceptance. In addition, the feed-down fraction of Λ particles coming from decays of Ξ resonances is estimated and the final spectra is corrected for this effect.

The jets are reconstructed via the anti-k_T algorithm implemented in the `FASTJet` package [6] from the sample of charged tracks passing basic quality criteria. The V^0-jet matching procedure is done on rather simple geometrical basis, based on distance between the reconstructed V^0 momentum vector and jet axis in $\eta \times \phi$ space (where η denotes pseudorapidity and ϕ azimuthal angle).

References

[1] V. Kučera, J. Phys.: Conf. Ser. 612, 12-13 (2015)

[2] B. I. Abelev, et al (STAR Coll.), Phys. Lett. B655, 104-113 (2007)

[3] M. A. C. Lamont, et al (STAR Coll.), J.Phys. G30, 963-968 (2004)

[4] B. B. Abelev, et al (ALICE Coll.), Phys. Rev. Lett. 111 (2013)

[5] R. J. Fries, B. Muller, C. Nonaka, S. A. Bass, Phys. Rev. Lett. 90 (2003)

[6] M. Cacciari, G. P. Salam, G. Soyez, Eur. Phys. J. C72 (2012)

The design and performance of the ATLAS Inner Detector trigger for Run 2

Ondrej Penc *(penc.ondrej@gmail.com)*

1 Introduction

After a two year upgrade that took place between 2013 and 2015, the LHC and all its experiments are going to extend their previous successes from the first period of their operation called Run 1. No doubt the greatest success of the ATLAS experiment was the observation of a new particle in the search for the Standard Model Higgs boson performed along with the CMS experiment in 2012 [1]. This discovery is a great success of particle physics that proposed the mechanism that suggested the existence of such a particle almost half a century ago in 1964 [2], [3]. To build on this success in Run 2 — the second operation period of the LHC — the hardware and software for the ATLAS detector was upgraded to perform efficiently in the new conditions.

2 LHC upgrade and ATLAS Detector

Table 1: Comparison of the LHC parameters at the end of Run 1 and the highest expected parameters after the upgrade for Run 2.

Machine parameter	Run1	Run2	Unit
Centre-of-mass energy	8	13	TeV
Luminosity	7×10^{33}	2×10^{34}	$\mathrm{cm}^{-2}\mathrm{s}^{-1}$
Bunch crossing spacing	50	25	ns
L1 input frequency	20	40	MHz
Mean pileup	~ 20	~ 40	interactions per crossing

Towards the end of Run 1, the LHC was routinely delivering instantaneous luminosities of $7.7 \times 10^{33}\,\mathrm{cm}^{-2}\mathrm{s}^{-1}$ with proton-proton collisions at 8 TeV centre-of-mass energy. Following the upgrade, the centre-of-mass energy was increased to 13 TeV and the luminosity is intended to be $2 \times 10^{34}\,\mathrm{cm}^{-2}\mathrm{s}^{-1}$. The parameters of the LHC after the upgrade are summarized in Table 1. Almost twice the beam energy provides a new probe of high energy physics. It will bring the confirmation of the Standard Model at yet unexplored energy regime or a discovery of physics beyond the Standard Model. The increased luminosity allow the precision study of Standard Model particles such as the top quark and especially the Higgs boson.

The ATLAS is a general-purpose detector at LHC located at CERN [4]. The detector comprises of several subsystems (ordered outside in) such as muon spectrometer in magnetic field of toroidal superconducting magnet, hadronic and electromagnetic calorimeters and the Inner Detector (ID). The ID is a high precision tracking device surrounding the ATLAS interaction point of the LHC beams to detect charged particles — products of the proton-proton collisions. It is placed inside 2 T axial magnetic field provided by a solenoid that is essential for particle charge and momentum identification.

3 Run 1 vs. Run 2 trigger architecture

Due to the LHC upgrade, the ATLAS trigger architecture had to undergo several changes to be able to fully exploit the new potential.

The time between bunch crossings was reduced from 50 ns to the 25 ns from the original design. This places a significant burden on the hardware and software subsystems of the ATLAS Trigger and lead to the trigger architecture upgrade. Also the high pileup multiplicity expected for Run 2 demands the need for a new tracking strategy and software optimisation. The CPU time consumption in simulated Run 2 events as a function of the pileup interaction multiplicity is illustrated in Fig. 1. Shown are the times for the two most time consuming stages of the Event Filter Inner Detector (EFID) trigger strategy as used during Run 1. The time consumption clearly grows non-linearly with the pileup multiplicity indicating that this would quickly become too costly to run in the ATLAS High Level Trigger (HLT) at high multiplicities.

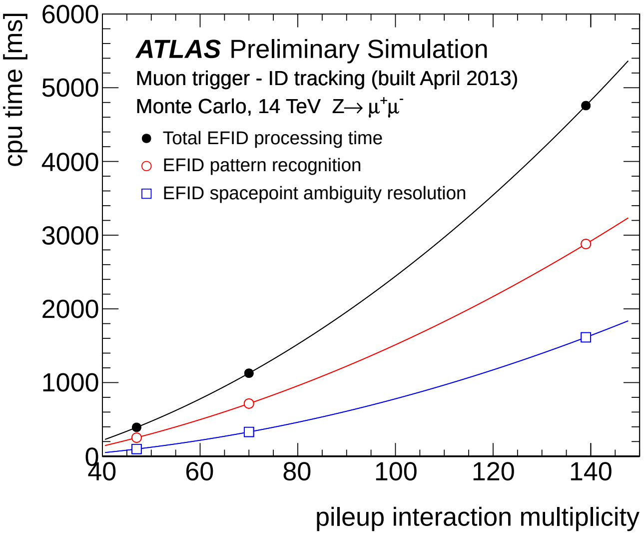

Figure 1: Dependence of the EFID trigger track reconstruction time on the mean number of pileup interactions using Z $\rightarrow \mu^+\mu^-$ Monte Carlo simulated data. Shown are the times for the most time-consuming tracking parts the main pattern recognition algorithm (circles) and Ambiguity Solver (squares) together with the total EFID tracking time (solid points) [5].

For the upgrade, the HLT architecture was simplified such that both the Run 1 software stages of the HLT – the Level 2 (L2) and Event Filter (EF) – have been merged into a single HLT stage to run on single CPU nodes. It simplifies the data-flow, removing the need for network communication between the L2 and EF trigger levels, and furthermore reduces requests to the DAQ system since common data preparation and storage was established.

The trigger processing still consists of similar algorithms as in the Run 1 [6]. It still works within the RoIs, but instead of two separate stages, L2 and subsequent EF where the processing started from scratch and repeated the CPU expensive pattern recognition on a different processing unit, the EF processing just becomes an additional step performed on the single HLT CPU node. Due to that the equivalent sequence of algorithms can be more efficiently combined, avoiding repetition and thus reducing reconstruction time [7]. Additionally the positioning of the full Event Building in the full processing chain is more flexible, and can be deferred until much later in the processing chain.

The new HLT processing has two parts. The first algorithm handles the pattern recognition and is known as the Fast Track Finder (FTF). The pattern recognition forms a track based on spacepoint triplets across the layers in the ID. The FTF is designed to generate medium quality tracks as quickly as possible and to provide them as the seeds for the subsequent Precision Tracking (PT) algorithm. The PT is offline-like algorithm optimised for speed. It resolves the hit to track association ambiguities and removes duplicate tracks via tracks scoring to finally perform accurate track fitting.

4 Optimisations for Run 2

The architectural changes of the ATLAS trigger were complemented by code optimisations as well. The upgrade provided an opportunity to optimise the old code and write the new one to be efficient from start.

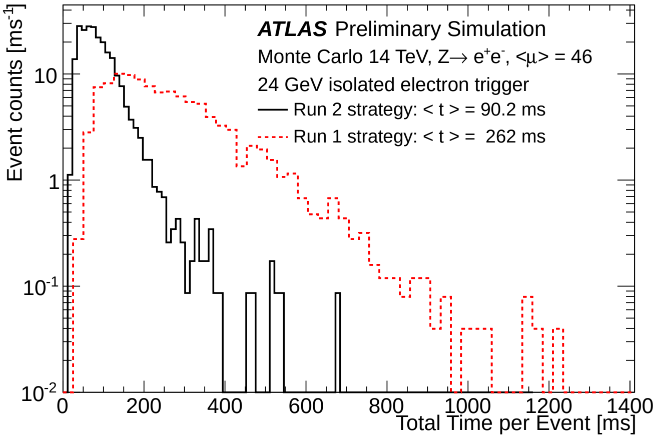

Figure 2: The distribution of total processing time of the electron trigger is shown. The plot compares the tracking strategy that was executed during Run 1 (dashed red line) to the new Run 2 strategy (solid black line) both running on $Z \rightarrow e^+e^-$ Monte Carlo simulated data [5].

The optimisation was initiated by the identification of inefficient parts of the ATLAS trigger code — referred to as hot spots — which were target of optimisations. These most often called, or computationally expensive parts of the code were determined using a profiling tool Valgrind [8]. Other optimisations, such as including modifications to avoid branch misprediction or cache misses, have also been studied previously [9]. The architectural changes, optimisations, faster linear algebra library, etc. contributed to threefold reduction of the execution time of the Run 2 ATLAS trigger tracking code as shown in Fig. 2 in comparison with the Run 1 strategy on simulated Run 2 data in 2014. The detailed timing study of the Run 2 HLT ID tracking code is described in Ref. [10].

5 Run 2 Inner Detector trigger performance

The ATLAS ID trigger is a key component of the HLT that has to make a decision whether to keep the collision event recorded by the ATLAS stored or not in a very short time period. The trigger performance is commonly measured with respect to the offline tracking algorithm that has more time for the event reconstruction. The trigger reconstruction is also referred as the online reconstruction.

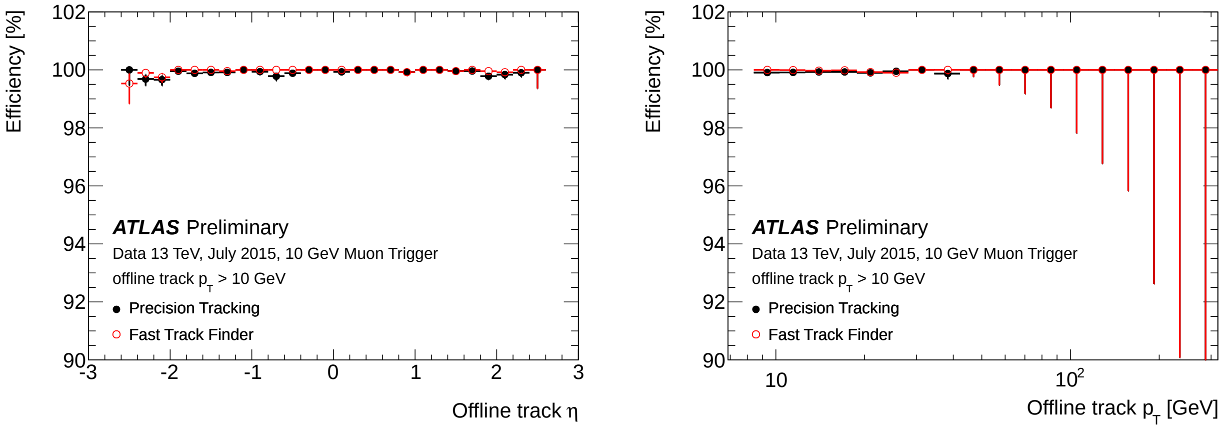

(a) (b)

Figure 3: The HLT ID tracking efficiency in the muon trigger as a function of pseudorapidity (a) and transverse momentum (b) with respect to the offline muon candidate. Measured on the earliest Run 2 data for FTF and PT stage [5].

The efficiency of the trigger tracking algorithm is a fraction of the number of all reconstructed tracks by online algorithm that match with the offline reconstructed tracks over the all offline tracks. The closest matching trigger track within a cone of $\Delta R < 0.05$ to the offline track is chosen. The efficiency as a function of pseudorapidity (η) and transverse momentum (p_{T}) is shown in Fig. 3(a) and (b) for muon chain and in Fig. 4(b) and (a) for electron chain. The efficiencies are shown for both trigger stages the FTF and PT. The efficiency of the muon trigger is almost 100 % in the first Run 2 data which confirms the efficiency is as good as in Run 1. The electron trigger efficiency is higher than 99 % and again is similar to the Run 1 efficiency. The FTF efficiency is slightly higher due to looser track requirements than in the PT which rejects the tracks of worse quality in the final stage.

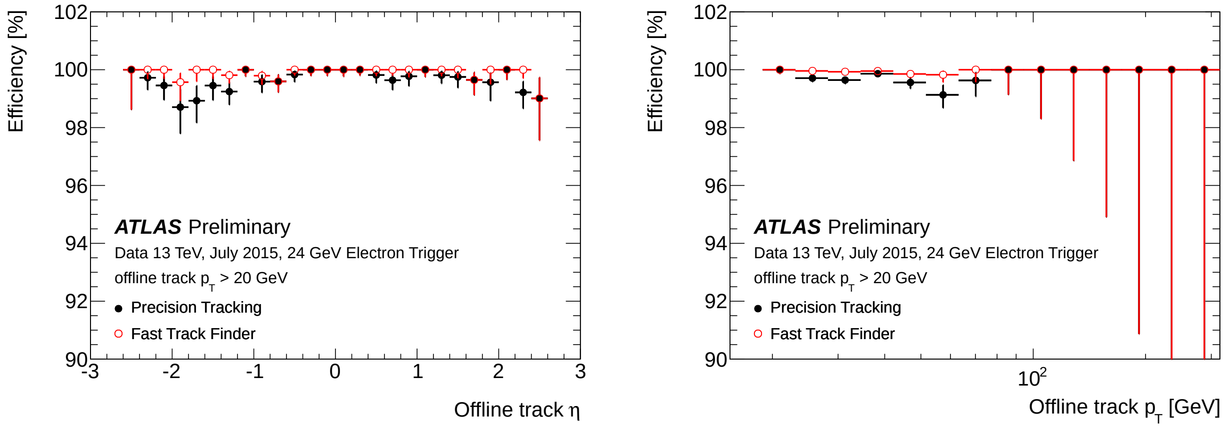

(a) (b)

Figure 4: The HLT ID tracking efficiency in the electron trigger as a function of pseudorapidity (a) and transverse momentum (b) with respect to the offline electron candidate. Measured on the earliest Run 2 data for FTF and PT stage [5].

6 Summary

The ATLAS trigger system underwent several upgrades to be able to fulfill the new requirements given by enhanced parameters of the Run 2 LHC. The upgrade was done in a way to maintain the outstanding performance from Run 1 for the next operation period. The trigger architecture was simplified to be more flexible and now provides new options improving the reconstruction process in the ATLAS HLT, such as the two-step tracking. Extensive profiling studies and optimisations were performed on the ATLAS tracking software to speed up the trigger decision process.

The results show the ATLAS ID trigger performance is in good shape for Run 2 and will help to extend the exceptional achievements of the detector from the first years of its operation.

References

[1] ATLAS Collaboration. Observation of a new particle in the search for the standard model higgs boson with the atlas detector at the lhc. *Physics Letters B*, 716(1):1 – 29, 2012.

[2] P.W. Higgs. Broken symmetries, massless particles and gauge fields. *Physics Letters*, 12(2):132 – 133, 1964.

[3] F. Englert and R. Brout. Broken symmetry and the mass of gauge vector mesons. *Phys. Rev. Lett.*, 13:321–323, Aug 1964.

[4] ATLAS Collaboration. The ATLAS experiment at the CERN large hadron collider. *Journal of Instrumentation*, 3(08):S08003, 2008.

[5] ATLAS Collaboration. HLT tracking public results, October 2015.

[6] ATLAS Collaboration. Performance of the ATLAS trigger system in 2010. *The European Physical Journal C*, 72(1), 2012.

[7] R Bartoldus et al. Technical Design Report for the Phase-I Upgrade of the ATLAS TDAQ System. Technical Report CERN-LHCC-2013-018. ATLAS-TDR-023, CERN, Geneva, Sep 2013. Final version presented to December 2013 LHCC.

[8] Nicholas Nethercote and Julian Seward. Valgrind: A framework for heavyweight dynamic binary instrumentation. In *Proceedings of the 2007 ACM SIGPLAN Conference on Programming Language Design and Implementation*, PLDI '07, pages 89–100, New York, NY, USA, 2007. ACM.

[9] ATLAS Collaboration. Studies for the development of the Inner Detector trigger algorithms at ATLAS. Technical Report ATL-DAQ-PUB-2013-002, CERN, Geneva, Sep 2013.

[10] O Penc and ATLAS Collaboration. The performance and development for the inner detector trigger algorithms at ATLAS. *Journal of Physics: Conference Series*, 608(1):012008, 2015.

Hypernuclear physics

Jan Pokorny *(pokorj29@fjfi.cvut.cz)*

1 Brief introduction to hypernuclear physics

Hypernuclear physics (also known as Strangeness nuclear physics) is a branch of nuclear physics which studies nuclei with strangeness $S \neq 0$, which means that there is a particle with $S \neq 0$ present in the nuclei, usually the Λ hyperon. Bound systems of nucleons and one or more hyperons are called hypernuclei.

Hypernuclear physics lies at the intersection of nuclear physics and particle physics. It has also important connection to astrophysics, because it is thought that hypernuclei might be created in the dense nuclear matter in the cores of neutron stars.

2 History of hypernuclear physics

The first hypernuclear event was observed in Poland in 1952 by physicists Jerzy Pniewski and Marian Danysz. They observed a track of nuclei in the nuclear emulsion plate which ended with great amount of energy released comparable to the decay of the π-meson. At first they brought up hypothesis that π-meson was bound in the nuclei the same as the electrons are bound in an atom, but this hypothesis was lately discarded because of the improbability of the π-meson capture.

Few weeks after the discovery they formed a correct hypothesis, that the nucleus contained bound Λ particle, discovered in 1951.

3 Experimental background and research groups

Experiments regarding strangeness nuclear physical phenomena are conducted in research facilities worldwide, for example J-PARC, KEK (Japan), MAMI (Germany), JLab (USA).

Further progress can be expected with the building of new facilities in J-PARC and $p\bar{p}$ collider in FAIR (Germany). These facilities will study the properties of $S = -2$ hypernuclei, containing either Ξ or $\Lambda\Lambda$.

Well known hypernuclear research groups are for example the Nuclear theory group in the Tohoku university, group of prof. Hiyama in RIKEN, Strangeness nuclear physics group in Nuclear Physics Institute in Rez and several others.

4 Nomenclature and production of hypernuclear systems

A hypernucleus is an atomic nuclei with atomic weight A, atomic number Z and one or more bound hyperons. A hyperon is a baryon containing at least one strange valence quark, i.e. Λ, Σ, Ξ or Ω^-. An example of conventional hypernuclear nomenclature would be

$$^{13}_{\Lambda}C,$$

a hypernucleus called 13-Λ-hypercarbon. It contains 13 baryons, one of which is a Λ hyperon. In case of the hypernuclei, the atomic number Z does not represent necessarily number of protons rather than a charge of the hypernucleus, therefore charged hyperons need to be included in the atomic number.

4.1 Production mechanisms

Hypernuclei are produced mainly via these mechanisms:

1. $K^- + n \rightarrow \Lambda + \pi^-$,
2. $K^- + p \rightarrow \Lambda + \pi^0$,
3. $\pi^+ + n \rightarrow \Lambda + K^+$,
4. $e^- + p \rightarrow e^- + \Lambda + K^+$,

where in the first two reactions an s quark is transferred from the kaon to a nucleon, whereas in the last two a pair $s\bar{s}$ is generated. Process 4. is usually called photo-production reaction.

5 Calculations of hypernuclear spectra

The topic of the author's bachelor thesis, supervised by Mgr. Petr Vesely, PhD. from the Nuclear Physics Institute in Rez, is Systematic calculations of hypernuclear spectra. This topic covers calculating of the hypernuclear spectra, single particle properties and radial density distributions of hypernuclei. The model used by author is based on the mean-field approximation - a method well suited to solve the many-body problem of interacting fermions.

5.1 Nuclear many body problem

Nucleus containing A particles is described by a Hamiltonian

$$\widehat{H} = \sum_{i=1}^{A} \widehat{t}_i + \sum_{i<j} \widehat{V}(\vec{r}_i, \vec{r}_j), \tag{1}$$

where

$$\widehat{t}_i = \frac{\widehat{P}_i^2}{2M} \tag{2}$$

is the kinetic energy operator and $\widehat{V}(\vec{r}_i, \vec{r}_j)$ is two-body interaction operator. Nuclear many body problem then means finding a spectrum of $\widehat{H}$, thereby solving Schroedinger's equation

$$\widehat{H}\psi_n = E_n\psi_n. \tag{3}$$

Unfortunately, equation (3) can be solved analytically only for nuclei containing maximum two nucleons. Spectra of light nuclei with $8 > A > 3$ can be solved using ab initio calculations. However, for heavier nuclei this presents a numerically difficult calculation, therefore the mean field approach is introduced.

5.1.1 Mean-field and the Hartree-Fock method

Mean-field approximation (in the description of nucleus) is based on the idea that we replace the mutual interactions of nucleons by an interaction of each nucleon with external field. Such external field (i.e. mean field) is constructed from the nucleon-nucleon interaction by solving the Hartree-Fock equation.

Unlike Coulomb potential for the electrons, there is no initial potential in the nuclei, mean field is generated fully self-consistently. Let $\xi = (\vec{r}, s)$ be a coordinate from the coordinate-spin space $\mathcal{H}$,

$$\mathcal{H} = \mathcal{H}_c \otimes \mathcal{H}_s, \tag{4}$$

then the HF equation can be expressed as

$$-\frac{\hbar^2}{2M} \triangle \psi_\beta(\xi) + U(\xi)\psi_\beta(\xi) - \int \mathrm{d}\xi' \, W(\xi, \xi')\psi_\beta(\xi') = E_\beta\psi_\beta(\xi). \tag{5}$$

5.1.2 Second quantization formalism

Hartree-Fock equation (5) can be reformulated in the language of second quantization which changes the integral-differential equation into problem of finding the eigenvalues of a matrix. This is very advantageous in the case when we represent the interaction in the form of the matrix elements V_{ijkl}.

The interaction operator is divided into interaction operators $pp, np, nn, p\Lambda, n\Lambda$. Note, that there is no $\Lambda\Lambda$ interaction. This is because we study only hypernuclei containing one Λ hyperon. One-body and two-body operators are in second quantization expressed as

$$\widehat{F} = \sum_{ij} \langle i|f|j\rangle a_i^\dagger a_j, \tag{6}$$

$$\widehat{V} = \frac{1}{4} \sum_{ijkl} \langle ij|v|kl\rangle a_i^\dagger a_j^\dagger a_l a_k, \tag{7}$$

where $a_i^\dagger, a_i$ are the creation and annihilation operators in a coordinate-spin space.

5.1.3 Realistic and phenomenological interactions

We distinguish between realistic and phenomenological interactions. The realistic interactions are derived microscopically from meson exchanges between two nucleons or between nucleon and hyperon. These interactions have to describe properly the experimental nucleon-nucleon or nucleon-hyperon scattering data (there is much less of the nucleon-hyperon experimental data than for the nucleon-nucleon case which limits significantly our knowledge about nucleon-hyperon interaction). On the other hand the phenomenological interactions have no relation to the two-body experimental data and depend on a number of parameters which have to be tuned to describe the nuclear and hypernuclear bulk properties. In our calculations we use the realistic nucleon-nucleon as well as nucleon-hyperon interactions.

5.1.4 Hartree-Fock method in the second quantization formalism

The objective of the HF method in second formalism is to find a basis $a_i'^{\dagger}, a_i'$, in which the matrix

$$t_{ij} + \sum_{kl} v_{ijkl} \langle \; | a_k^{\dagger} a_l | \; \rangle \tag{8}$$

is diagonal. This basis is called HF basis. For simplicity the equation (8) refers only to the Hartree-Fock method with one type of particle. However, in the hypernuclei there are two types of nucleons present. HF method then gives two equations for protons (π) and neutrons (ν):

$$t_{ij}^{\pi} + u_{ij}^{\pi} = \delta_{ij} \varepsilon_i^{\pi}, \tag{9}$$

$$t_{ij}^{\nu} + u_{ij}^{\nu} = \delta_{ij} \varepsilon_i^{\nu}. \tag{10}$$

As mentioned above, there is no initial mean field in the nuclei, we start with some known basis, i.e. harmonic oscillator or Wood-Saxon, etc. Therefore we start with initial ε_i. The HF equations give some new basis and new ε_i', which is used as a new input into the equations. This process is repeated until

$$|\varepsilon_i - \varepsilon_i'| \approx 0. \tag{11}$$

The Λ particle then interacts with the mean-field of nucleons which can be described by the equation:

$$t_{ij}^{\Lambda} + u_{ij}^{\Lambda} = \delta_{ij} \varepsilon_i^{\Lambda}. \tag{12}$$

6 Problems

The approximation of mean field treats the nucleons and Λ as independent non-interacting particles. Such approximation can be useful to describe certain properties of hypernucleus (mainly the single-particle properties) but is not sufficient in general. To improve our calculations we anticipate to incorporate the beyond mean field configurations (we refer to them also as complex configurations). For this we need to take into account the residual interactions - a part of Hamiltonian which does not take part at the mean field level. Other problem is that so far we do not include yet the core polarization effects of Λ particle. This effect will be treated by coupling of Λ with the complex configurations.

References

[1] Petr Bydzovsky, Avraham Gal, Jiri Mares, *Topics in Strangeness Nuclear Physics*, Lect. Notes Phys. 724 (2007)

[2] A. Feliciello, T. Nagae, *Experimental review of hypernuclear physics: recent achievements and future perspectives*, Rep. Prog. Phys. 78 096301 (2015)

[3] Andrzej K. Wroblowski, *Hypernuclei (and strange particles) - how it all began?*, Acta Physica Polonica B vol. 35 (2004)

[4] B. Alex Brown, *Lecture notes in nuclear structure physics*, Michigan State University (2005)

Semi-inclusive p_T spectra of jets in light systems at the LHC energies

Peter Príbeli *(peter.pribeli@cern.ch)*

1 Introduction

It is customary to discuss high energy hadron collisions in terms of partons (quarks and gluons) described by QCD. Due to the colour confinement in QCD, individual quarks or gluons may not exist as isolated free particles in vacuum. Hence a parton that underwent a hard scattering process tends to restore it's colour field equilibrium configuration. It does so by radiating partons—*parton showering*. These energetic, collimated high energy parton showers are called *jets*.

Jets are used in many areas of physics analyses and may help in understanding various properties of the top quark, hadronisation, hadron structure, quark gluon plasma and others.

A jet might not be an obvious structure when looked upon by eye and a rigorous definition of the concept is needed. Using this definition a *jet algorithm* can reconstruct a jet from the signals measured in a detector. An event display of two jets reconstructed by the OPAL detector may be seen in Figure 1.

Corrections on various detector effects on acquired data are often necessary. A linear relation of true and measured quantities is expected. This linear transformation is described by the so-called response matrix $\mathbb{A}$ of the detector which is usually acquired by means of Monte-Carlo simulations.

Suppose that a vector $\vec{b}^{rec}$ is composed of a physical quantity reconstructed by the detector. This can be achieved by assigning a particular count of an histogram bin to each element of $\vec{b}^{rec}$. It is desired to obtain the true physical quantity $\vec{b}^{true}$. Hence one has to solve a linear system

$$\mathbb{A}\vec{b}^{true} = \vec{b}^{rec}. \tag{1}$$

Thus the elements of the response matrix represent *probabilities* of b_i^{true} corresponding to b_i^{rec} for all values of i.

The process of solving (1) and thereby obtaining $\vec{b}^{true}$ is called *unfolding*.

Two approaches to unfolding are presented. One is based on the Singular Value Decomposition (SVD) theorem[1] and the other on Bayes' theorem[2].

Let us redefine $\vec{x} := \vec{b}^{true}$ and $\vec{b} := \vec{b}^{rec}$ for further convenience.

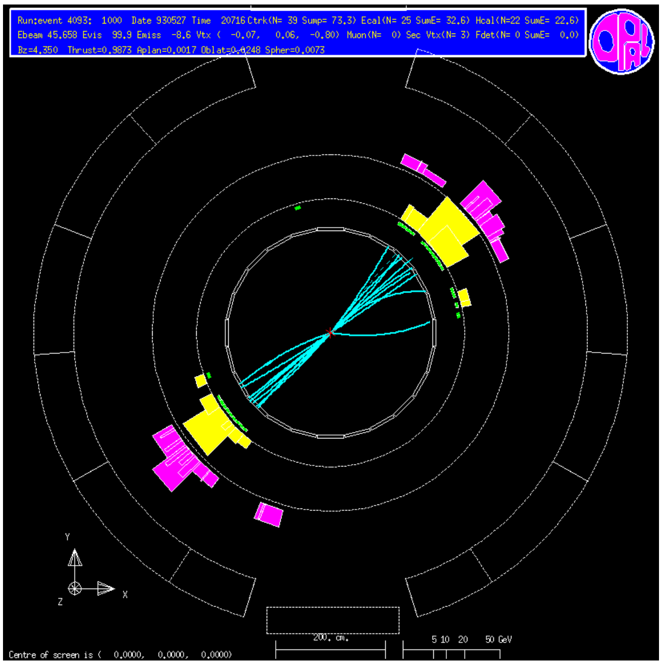

Figure 1: A two-jet event produced by the Z^0 boson decay as reconstructed by the OPAL detector at LEP[3].

2 Singular Value Decomposition

This method of unfolding is based on the SVD theorem which states that an arbitrary matrix $\mathbb{A} \in \mathbb{R}^{m,n}, n, m \in \mathbb{N}$ admits a decomposition of the form

$$\mathbb{A} = \mathbb{U}\mathbb{S}\mathbb{V}^T, \tag{2}$$

where $\mathbb{U} \in \mathbb{R}^{m,m}$ and $\mathbb{V} \in \mathbb{R}^{n,n}$ are orthogonal matrices and $\mathbb{S} = diag(\sigma_1, \sigma_2, ..., \sigma_r)$. The numbers $\sigma_1 \geq \sigma_2 \geq \sigma_r \geq 0$ are called the singular values of $\mathbb{A}$ where $r = rank(\mathbb{A})$.

This simplifies the inversion of $\mathbb{A}$ because the inverse of an orthogonal matrix is equal to the transpose of the matrix and the inverse of a diagonal matrix is calculated by replacing the diagonal values by their reciprocals.

The problem with the SVD arises when the singular values of $\mathbb{A}$ are zero or close to zero. In that case $\mathbb{S}^{-1}$ does not exist and a regularization is needed.

A transformation may be applied to the matrices and unknowns in order to normalize the unknowns.

Consider $\forall i \in \{1, 2, ..., m\}, \forall j \in \{1, 2, ..., n\}$

$$y_i := x_i / x_i^{ini}, \tag{3}$$

$$\bar{\mathbb{A}}_{ij} := \mathbb{A}_{ij} x_j^{ini}, \tag{4}$$

where $\vec{x}^{ini}$ is an initial estimate. It is obvious that $\bar{\mathbb{A}}\vec{y} = \vec{b} \Leftrightarrow \mathbb{A}\vec{x} = \vec{b}$. This transformation reduces the number of terms in the decomposition when $\vec{x}^{ini}$ and $\vec{x}$ are sufficiently close.

2.1 Regularization

Solving (1) is equivalent to minimising the quadratic form

$$(\bar{\mathbb{A}}\vec{y} - \vec{b})(\bar{\mathbb{A}}\vec{y} - \vec{b})^T + \tau\,(\mathbb{C}\vec{y})^T\,\mathbb{C}\vec{y} = \text{min.}, \tag{5}$$

where the second term, $\tau\,(\mathbb{C}\vec{y})^T\,\mathbb{C}\vec{y}$, is introduced for regularization purposes. The parameter τ represents the weight of the normalisation. While this parameter is strongly problem-dependent and must be determined numerically, the *a priori* condition $\mathbb{C}$ may be determined from general considerations.

The form of $\mathbb{C}$ may be chosen as

$$\mathbb{C} = \begin{pmatrix} -1+\varepsilon & 1 & 0 & 0 & \cdots & 0 \\ 1 & -2+\varepsilon & 1 & 0 & \cdots & 0 \\ 0 & 1 & -2+\varepsilon & 1 & \cdots & 0 \\ \vdots & \vdots & \vdots & \vdots & \ddots & \vdots \\ 0 & 0 & 0 & 0 & \cdots & -1+\varepsilon \end{pmatrix}, \tag{6}$$

where the small increment ε is added to the diagonal in order to render $\mathbb{C}$ invertible. A sensible choice for ε is on the order of $\varepsilon = 10^{-3}$.

The choice of $\mathbb{C}$ is justified by the requirement of smoothness on the solution.

2.2 Unfolding

This approach leads to an over-determined system of equations

$$\begin{pmatrix} \bar{\mathbb{A}}\mathbb{C}^{-1} \\ \sqrt{\tau}\mathbb{I} \end{pmatrix} \mathbb{C}\vec{y} = \begin{pmatrix} \vec{b} \\ \vec{0} \end{pmatrix}. \tag{7}$$

of which the solution is searched by the so-called *damped least squares* method.

Firstly, the parameter τ is set to zero and SVD is used to decompose $\bar{\mathbb{A}}\mathbb{C}^{-1}$ into

$$\bar{\mathbb{A}}\mathbb{C}^{-1} = \mathbb{U}\mathbb{S}\mathbb{V}^T, \tag{8}$$

where $\mathbb{U}$, $\mathbb{V}^{\mathbb{T}}$ are orthogonal and $\mathbb{S}$ is diagonal. Let

$$\vec{d} := \mathbb{U}^T\vec{b}, \tag{9}$$

$$\vec{z}^{(0)} := \mathbb{V}^T\mathbb{C}\vec{y}, \tag{10}$$

where the upper index represents the value of τ.

The system (7) now takes the form

$$\mathbb{S}\,\vec{z}^{(0)} = \vec{d}. \tag{11}$$

One can show that introducing a non-zero parameter τ is equivalent to modifying the vector $\vec{d}$ as

$$d_i^{(\tau)} = d_i \frac{\mathbb{S}_{ii}^2}{\mathbb{S}_{ii}^2 + \tau}, \tag{12}$$

and the $\vec{z}$ vector takes the form

$$z_i^{(\tau)} = \frac{d_i\,\mathbb{S}_{ii}}{\mathbb{S}_{ii}^2 + \tau}, \tag{13}$$

and thus the solution to (7) is

$$\vec{y}^{(\tau)} = \mathbb{C}^{-1}\,\mathbb{V}\,\vec{z}^{(\tau)}. \tag{14}$$

The role of τ as a regularization term is now obvious. The desired distribution $\vec{x}$ is obtained by rescaling $\vec{y}^{(\tau)}$ by $\vec{x}^{ini.}$.

The cut-off parameter τ can be determined by plotting $\log|d_i|$ versus i and selecting $\tau = \mathbb{S}^2_{kk}$ where k is the point where statistically significant entries dominate fluctuations.

3 A Bayesian approach

Let us use the following statement of Bayes' theorem.

Let $C_i,\ i \in [1, n_C]$ be independent causes that produce an effect E. Let further $P(\bullet|\bullet)$ be conditional probabilities. The conditional probability of C_i given E is then given by

$$P(C_i|E) = \frac{P(E|C_i)P(C_i)}{\sum_{j=1}^{n_C}\left[P(E|C_j)P(C_j)\right]}, \tag{15}$$

where $P(C_i)$ is the probability of C_i.

Bayes' theorem has the power to *increase* knowledge about the initial probabilities $P(C_i)$ with iteration. One can even begin without any *a priori* knowledge of $P(C_i)$ and use a uniform distribution. On the other hand, the conditional probabilities $P(E|C_i)$ are not effected and thus must be calculated beforehand, usually by means of Monte Carlo simulations.

Consider N measurements of an effect E_j where $j \in [1, n_E]$. The number of effects being caused by a cause C_i is then by definition

$$N_{C_i} = N\,P(C_i|E_j). \tag{16}$$

For each E_j the conditional probability $P(C_i|E_j)$ can be found according to Bayes' theorem.

The conditional probability $P(E_j|C_i)$ must be normalized ($\sum_{k=1}^{n_C} P(E_j|C_k) = 1$). This implies that all effects have a cause. The reverse however, does not hold true. There might be redundant causes included. Therefore it is convenient to define a measure of efficiency $0 \le \epsilon_i = \sum_{k=1}^{n_E} P(E_k|C_i) \le 1$.

3.1 Unfolding

To illustrate the usefulness of Bayes' theorem, one can associate the effects (E) with the observation of an event in a given bin of the reconstructed distribution. The causes (C_i) are then all the events in the bins of the true distribution.

Consider again the system of equations (1): $\mathbb{A}\vec{x} = \vec{b}$, where $\vec{x} \in \mathbb{R}^n$ is the true spectrum and $\vec{b} \in \mathbb{R}^m$ is the reconstructed spectrum. Let us identify

$$P(E_j|C_i) = A_{ij}, \tag{17a}$$

$$N_i = b_i, \tag{17b}$$

where N_i is the number of measurements of the effect E_i. The fact that no effect is without cause is consistent with the requirement $n \ge m$.

The unfolded spectrum is then given by

$$x_i = \begin{cases} \frac{1}{\epsilon_i} \sum_{j=1}^{n_E} N_j \, P(C_i|E_j), & \epsilon_i \neq 0 \\ 0, & \epsilon_i = 0. \end{cases} \tag{18}$$

The probability of the causes is

$$P(C_i) = \frac{x_i}{\sum_{j=1}^{n_C} x_j}. \tag{19}$$

3.2 Algorithm

The algorithm for the iterative Bayesian approach to spectra unfolding might be formulated as follows

1. Chose an initial $P(C_i)^{(0)}$. In case of complete ignorance, pick a uniform distribution. Further, calculate the initial $x_i^{(0)} = \frac{P(C_i)^{(0)}}{N_{ev.obs.}}$.
2. Compute x_i according to (18) (using $P(C_i)^{(0)}$).
3. Determine $P(C_i)$ according to (19).
4. Do a χ^2 comparison between x_i and $x_i^{(0)}$, if the χ^2 is too high replace $x_i^{(0)}$ by x_i and $P(C_i)^{(0)}$ by $P(C_i)$ and go to step 2.
5. Repeat until χ^2 is sufficiently small.

References

[1] Hocker, Andreas, and Vakhtang Kartvelishvili. *SVD Approach to Data Unfolding.* Nucl.Instrum.Meth. A372 (1996) 469-481.

[2] D'Agostini, G. *A Multidimensional Unfolding Method Based on Bayes' Theorem.* Nucl.Instrum.Meth. A362 (1995) 487-498.

[3] OPAL Events at LEP1. *OPAL Event Displays*, Accessed 18.01.2016. `http://opal.web.cern.ch/Opal/events/opalpics.html`

Analysis of D0 meson production in Cu+Au collisions in the STAR experiment

Miroslav Šaur *(saurmiro@fjfi.cvut.cz)*

Relativistic Heavy Ion Collider is located at Brookhaven National Laboratory in the USA. RHIC is able to collide various types of particles and ions. Over the years RHIC has collided symmetric system as: p+p, Cu+CU, Cu+AU, Au+AU, U+U. Also non-symmetric systems were collided: p+Au, d+Au, He+Au, Cu+Au. Primary field of study of RHIC is a quark-gluon plasma (QGP). Quarks and gluons are bounded in matter via the strong force and because of confinement effect they cannot be free. But in QGP, which is system with high temperature and pressure, quarks and gluons are free particles. For purpose of creating QGP we collide heavy ions to obtain high temperature and energy density. According the lattice QCD phase transition between hadronic matter and QGP occur at temperature $T_c = 170MeV$. QGP is created about $/tau = 1fm/c$ after collision and is dissolved in $/tau = 1fm/c$. This medium interact only via the strong force, that means, any strong-interacting particle should be affected by this medium. Main measurements of this affection are: Nuclear modification factor, jet quenching, broadening of jets. Another measurements include particle flow, . Is it believed todaz, that QGP is the state of matter in which universe existed in TIME after the Big bang.

To study this new type of matter, we need detectors and suitable probes. Solenoidal Tracker At RHIC (STAR) detector is primarily focused on study of heavy ion collisions and QGP. Main component of STAR is room-temperature solenoid magnet which cover most of subsystems of detector. Solenoid magnet have maximum magnetic field strength $B_{max} = 0.5T$ but can operate at one half of maximum field strength $B_{1/2} = 0.25T$. Magnetic field is parallel to beam axis. Primary tracking device of STAR is Time Projection Chamber (TPC). The TPC is cylindrical tracking device with full azimuthal coverage. TPC outer diameter is $r_{out} = 4m$ and inner $r_{in} = 1m$. Pseudorapidity coverage is ±1.8 units. Time-of-Flight detector (TOF) is designated to work together with TPC to obtain information about masses and velocity of particles passing through TPC a TOF. Barrel electromagnetic calorimeter (BEMC) is a sampling calorimeter situated between TOF and solenoidal magnet.The BEMC consists of 120 calorimeter modules. Each one module is divided into 40 towers, 2 towers are in ϕ - direction and 20 towers are in η - direction. Each Another important parts of STAR detector are: Vertex position detector (VPD) which consist of two identical detectors, one on the east and one on the west side of STAR. Next one is Heavy flavour tracker (HFT), installed in 2014, a high resolution silicon pixel detector. For our analysis we used primarily TPC a TOF sub-detectors.

D^0 meson is bounded state of charm quark and anti-up quark (anti-D^0 consist of anti-charm and up quark). Charm quark with beauty and top quark belongs to heavy quarks, which are produced in the hard processes. Hard processes occur almost instantaneously after collision, so heavy quarks are created even before formation of the QGP. Quarks then propagate through medium, are affected by medium and we try found how and how much they are affected. D^0 can decay into leptonic, semileptonic of hadronic decaying channel. In this analysis we focus on two hadronic decaying channels, where D^0 decay into $K^+\pi^-$ or $K^-\pi^+$. Branching ratio of both channels is $3.88 \pm 0.05\%$.

In the year 2012 for 5.5 weeks, Cu+Au collisions take place at RHIC. Isotopes $^{63}_{29}$Cu and $^{197}_{79}$Au was collided with energy $\sqrt{s_{NN}} = 200 GeV$. Primary motivation of Cu+AU collisions was a measurement of this system control geometry, because according the Glauber model, number of participants in Cu+Au central collisions should agree with semi-central Au+Au collisions. Cu+Au system is asymmetrical both in longitude and transverse direction. Sketch of this system we can see at 1. Another possibilities are study flow effect created by initial asymmetric density profile which lead to to asymmetric pressure gradient.

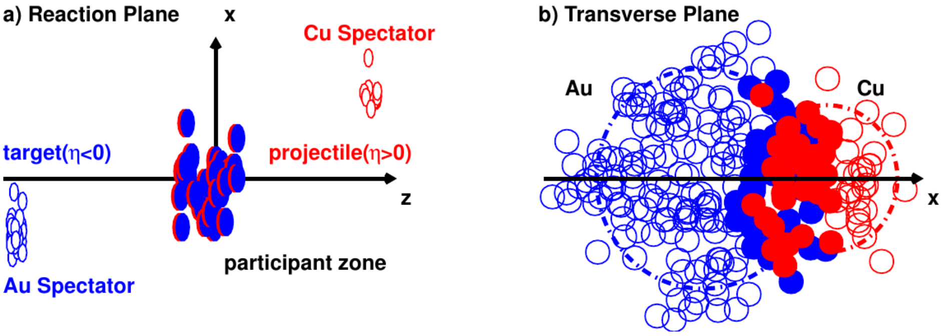

Figure 1: Schematic imagination of Cu+Au collision. a: View from a reaction plane. b: View from transverse plane.

References

[1] Observation of D0 Meson Nuclear Modification in Au+Au Collisions at $\sqrt{s_{NN}} = 200 GeV$, Phys. Rev. Lett 113, 142301

[2] Measurements of D0 and D* production in p+p collisions at $\sqrt{s_{NN}} = 200 GeV$, Phys. Rev. D 86, 072013

[3] K. Yagi et al., Quark-gluon plasma, Cambridge Universtity Press, (2005)

Production of transverse momentum spectra in ultrarelativistic nuclear collisions

Radka Sochorová *(sochorad@fjfi.cvut.cz)*

In the early phase of an ultrarelativistic nuclear collision quark-gluon plasma is produced. The system expands and its energy density drops. When the energy density is not high enough for the existence of plasma, it changes into the gas of hadrons. Hadrons interact strongly and can not escape from the fireball. When the energy density of hadron gas is low enough, there are no more scatterings between hadrons. The process of decoupling of hadrons from the fireball is called freeze-out. Kinematic freeze-out occurs when the system do not change kinematically (do not change momentum of particles). In my bachelor thesis I am interested in the shape of freeze-out hypersurface and in the effects which influence this shape. Lorentz invariant momentum spectrum of particles radiated by a thermal source with temperature T:

$$E\frac{d^3N}{dp^3} = \frac{d^2N}{m_T dm_T d\phi dy} = \int_\sigma d\sigma_\mu p^\mu f(x,p). \tag{1}$$

Firstly, we need to determine how many particles cross freeze-out the hypersurface of the fireball. The infinitesimal element is given by

$$d\sigma_\mu = \varepsilon_{\mu\nu\kappa\rho}\frac{\partial x^\nu}{\partial\alpha}\frac{\partial x^\kappa}{\partial\beta}\frac{\partial x^\rho}{\partial\gamma}d\alpha d\beta d\gamma, \tag{2}$$

where α, β, γ are three coordinates which we use to parametrize the hypersurface σ and $\varepsilon_{\mu\nu\kappa\rho}$ is antisymmetric tensor, $\varepsilon_{0123} = 1$. This equation can be used to computing the general volume of freeze-out hypersurface. The number of particles with momentum p which cross the element $d\sigma_\mu(x)$ at a given point x is

$$dN(p) = d\sigma_\mu(x)p^\mu d^4p 2\delta(p^2 - m^2)f(x,p) = d\sigma_\mu(x)p^\mu\frac{d^3p}{p^0}f(x,p), \tag{3}$$

where f(x,p) is the phase-space distribution (Bose-Einstein, Fermi-Dirac or Maxwell-Boltzman). When we will integrate over the whole freeze-out hypersurface, we gain the total number of particles with momentum p

$$N(p) = \int_\sigma d\sigma_\mu(x)f(x,p)p^\mu\frac{d^3p}{p^0}, \tag{4}$$

without the integration over momentum we obtain the spectrum. A real fireball is not stationary. In fact undergoes strong longitudinal expansion. The most common prescription for longitudinal expansion is Bjorken boost-invariant model. Longitudinal boost-invariant expansion looks the same in all reference frames with whatever longitudinal velocity.The fireball has to be longitudinally infinite (otherwise, we will be able to see the difference between the velocity in the center of collision and at the edge). It is unrealistic but in collisions with high energy it is possible to create fireball which looks boost-invariant in the central region. Longitudinal velocity in the case of boost-invariant expansion is given by

$$v_z = z/t. \tag{5}$$

A real fireball expands also in the direction transverse to the beam. We have the case of azimuthally symmetric fireball which is produced in the central collision. We have to add transverse velocity which has two components

$$v_x = v_t \cos\theta, \tag{6}$$

$$v_y = v_t \sin\theta. \tag{7}$$

Transverse velocity depends on the distance from the longitudinal axis of fireball r. We parametrize the velocity fireball using transverse rapidity $\eta_t(r)$. Transverse velocity is given by

$$v_t = \frac{\tanh\eta_t(r)}{\cosh\eta_s}, \tag{8}$$

where

$$\cosh\eta_s = \frac{1}{2}\ln(\frac{1+v_z}{1-v_z}). \tag{9}$$

I parametrized the freeze-out hypersurface using the parabolic dependence

$$\tau_f(r) = a_0 + a_1 r + a_2 r^2. \tag{10}$$

This gives cartesian coordinates

$$x^0 = t = \tau_f(r)\cosh\eta_{\|} \tag{11}$$

$$x^1 = r\cos\phi \tag{12}$$

$$x^2 = r\sin\phi \tag{13}$$

$$x^3 = \tau_f(r)\sinh\eta_{\|}. \tag{14}$$

Than I compute the infinitesimal elements of the area

$$d\Sigma^\mu = (\cosh\eta_{\|}, \frac{\partial\tau_f(r)}{\partial r}\cos\phi, \frac{\partial\tau_f(r)}{\partial r}\sin\phi, \sinh\eta_{\|}) r\tau_f(r) d\eta_{\|} d\phi dr. \tag{15}$$

The next step in my computing was

$$d\Sigma_\mu p^\mu = (m_T\cosh(y-\eta_{\|}) + \frac{\partial\tau_f(r)}{\partial r} p_T \cos(\phi-\phi')) r\tau_f(r) d\eta_{\|} d\phi dr. \tag{16}$$

For protons I used Fermi-Dirac distribution and for pions Bose-Einstein distribution

$$f_{eq}(p^\alpha u_\alpha) = \frac{1}{(2\pi)^3}[\exp(\frac{p^\alpha u_\alpha - \mu}{T}) - \varepsilon]^{-1}, \tag{17}$$

where ε = 1 for bosons and ε = -1 for fermions.
Four-velocity is defined as

$$u_\mu = (\cosh\eta_{\parallel}\cosh\eta_T, \sinh\eta_T\cos\phi, \sinh\eta_T\sin\phi, \sinh\eta_{\parallel}\cosh\eta_T), \tag{18}$$

where

$$\sinh\eta_T = \eta_f(\frac{r}{R}). \tag{19}$$

Then

$$p^\mu u_\mu = (p_T\sinh\eta_T\cos(\phi-\phi') + m_T\cosh\eta_T\cosh(\eta_{\parallel}-y)), \tag{20}$$

where

$$p_T = \sqrt{p_x^2 + p_y^2} \tag{21}$$

and

$$m_T = \sqrt{p_T^2 + m^2}. \tag{22}$$

I assumed values of these parametres

$$\eta_f = 0.8; T = 120MeV; \mu = 0; a_0 = 10; a_1 = 0; a_2 = \pm 1/20, 0; R = 10. \tag{23}$$

After integration over $\mathrm{d}\phi\mathrm{d}\eta_{\parallel}$ and introduction of modified Bessel function I_0, I_1, K_0 and K_1 the transverse momentum spectrum is

$$\begin{aligned}\frac{dN}{p_T dp_T dy d\phi} &= \sum_1^\infty \frac{m_T}{\pi}(-1)^{n+1}\int_0^R r\tau_f(r) I_0(\frac{np_T\eta_f\frac{r}{R}}{T})K_1(\frac{nm_T\cosh\eta_T}{T})dr \\ &+ \sum_1^\infty \frac{p_T}{\pi}(-1)^{n+1}\int_0^R \frac{\partial\tau_f}{\partial r}\tau_f I_1(\frac{np_T\eta_f\frac{r}{R}}{T})K_0(\frac{nm_T\cosh\eta_T}{T})dr.\end{aligned} \tag{24}$$

For the sake of simplicity we cut the summations after the third terms.
The resulting spectra for pions and protons for three different shapes of the freeze-out hypersurface are plotted in Figs. 1 and 2.

References

[1] E. SCHNEDERMANN, J. SOLLFRANK, U. HEINZ: Thermal phenomenology of hadrons from 200A GeV S+S collisions, Phys.Rev. C48 (1993) 2462-2475

[2] TOMÁŠIK, B., F. SANNINO, I. BEARDEN a T. DOSSING. Topics in modern nuclear physics: Flow and Sizes. Kobenhavns Universitet, Niels Bohr Institutet, 2004

[3] TOMÁŠIK, B., F. SANNINO, I. BEARDEN a T. DOSSING. Topics in modern nuclear physics: Observables addressed by hydrodynamics. Kobenhavns Universitet, Niels Bohr Institutet, 2004

[4] FLORKOWSKI, Wojciech. Phenomenology of Ultra-relativistic heavy-ion collisions. Jan Kochanowski University: World Scientific Publishing, 2010

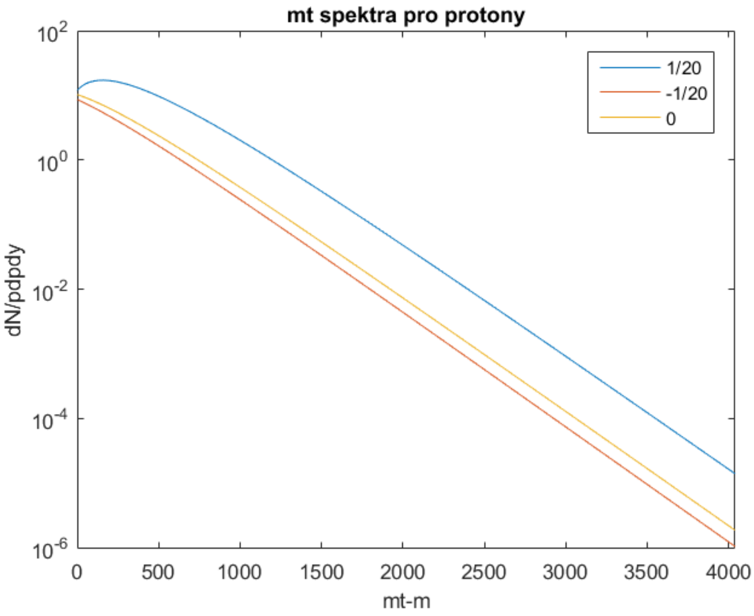

Figure 1: Transverse mass spectrum for protons for different coefficient a_2.

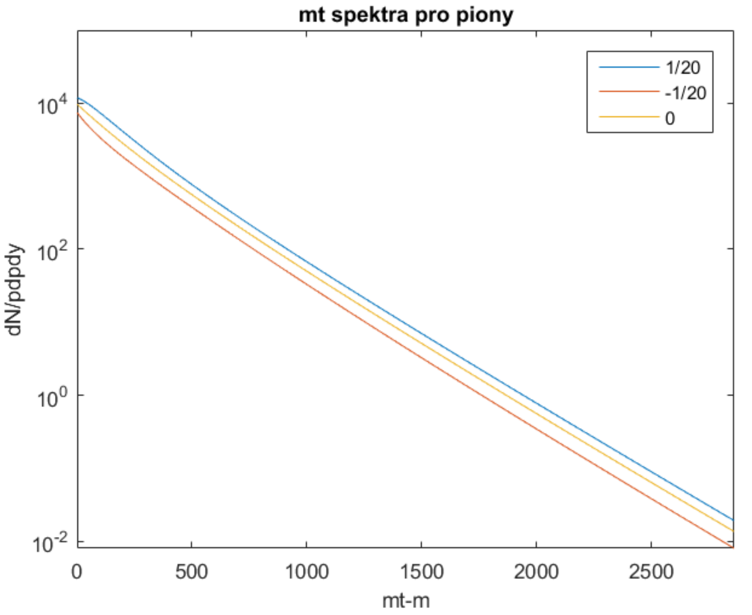

Figure 2: Transverse mass spectrum for pions for different coefficient a_2.

ATLAS Computing for Run 2

Michal Svatoš*(michal.svatos@fjfi.cvut.cz)*

ATLAS Computing [1] faced many challenges before the beginning of Run-2. The LHC accelerator was upgraded to higher energy and luminosity. It caused more than twice events to process in Run-2 with respect to Run-1. On the other hand, computing resources are expected to grow only by ∼20 % every year. How ATLAS adapted to this challenge is described in the following.

Several systems were developed to cope with Run-2 data. First, there is new distributed data management system, called Rucio [2]. It manages about 160 PB of data on more than 750 storage endpoint. In Rucio, every user, group or organised production activity is represented by an account. Every account has a data namespace identifier called scope which is used to partition the data namespace. Data files are the smallest unit of data. Files can be grouped into datasets and datasets can be grouped to containers. For Rucio, all these are called data identifiers (DIDs). Rucio Storage Element (RSE) is unit of storage space in Rucio (=endpoint). The transfers of data managed by Rucio are done by FTS3[3]. Then, there is Prodsys-2. It is a workload management system. It consists of four parts. First is Request Interface which allows management of production requests. Second is Database Engine for Tasks (DEfT) which translates production requests into tasks. Third is Job Execution and Definition Interface (JEDI) which dynamically creates jobs from the task definitions. And fourth is PanDA[4] which executes the jobs in the distributed environment.

In addition to new systems, there are several ways to improve resource utilisation.One example is improvement in reconstruction code which resulted in a reduction of the CPU time per event by almost a factor four. Another example is enabling of multi-processing in the reconstruction framework which keeps memory usage below the 2 GB per core (standard on available computing resources).

In order to get as much computing resources as possible, ATLAS is using so called opportunistic resources. Those are nonpledged (and in many cases volatile) computing resources. First of them is cloud computing. One example is usage of cloud technology on High Level Trigger (HLT) farm[5] (providing about 20k cores) which is available to the offline production activities in the periods when the online activities were stopped. Next case are High Performance Computers (HPCs), i.e. supercomputers (computers designed for massively parallel applications). Next case is volunteer computing. ATLAS@home[7] project allows usage of idle desktops and laptops. It is based on BOINC client and runs simulation payload. The Event Service[6] (ES) provides payloads at level of events designed for these volatile computing resources.

ATLAS Computing is a complex system and its functioning requires non-stop supervision. ATLAS formed several kinds of computing shift to help to keep the system running. Distributed Analysis Support Team (DAST) deals with computing related issues physicist have. ATLAS Distributed Computing operations Shifts (ADCoS) monitor and report issues of production activities (T0 export, data transfers, production jobs, etc.). Computing Run Coordinator (CRC) coordinates the daily ADC operations and is the main link within the ATLAS ADC communities.

References

[1] S. Campana, J. Phys. Conf. Ser. **664** (2015) 3, 032004. doi:10.1088/1742-6596/664/3/032004

[2] M. Barisits, C. Serfon, V. Garonne, M. Lassnig, T. Beermann and R. Vigne, J. Phys. Conf. Ser. **664** (2015) 6, 062002. doi:10.1088/1742-6596/664/6/062002

[3] H. Riahi *et al.*, J. Phys. Conf. Ser. **664** (2015) 6, 062051. doi:10.1088/1742-6596/664/6/062051

[4] K. De *et al.*, J. Phys. Conf. Ser. **664** (2015) 6, 062035. doi:10.1088/1742-6596/664/6/062035

[5] R. P. Taylor *et al.*, J. Phys. Conf. Ser. **664** (2015) 2, 022038. doi:10.1088/1742-6596/664/2/022038

[6] P. Calafiura *et al.*, J. Phys. Conf. Ser. **664** (2015) 6, 062065. doi:10.1088/1742-6596/664/6/062065

[7] C. Adam-Bourdarios *et al.* [ATLAS Collaboration], J. Phys. Conf. Ser. **664** (2015) 2, 022009. doi:10.1088/1742-6596/664/2/022009

Statistical Model of Hadron Production

Josef Uchytil *(uchytjos@fjfi.cvut.cz)*

My report was supposed to provide basic information on the statistical model, which is widely used when interpreting the chemical composition of hadrons produced in ultra-relativistic heavy ion collisions. The statistical model as such was introduced and two possible approaches - grandcanonical (GC) and canonical (C) - were elaborated. Furthermore, a brief review of my bachelor thesis was introduced.

1 Ultra-relativistic heavy ion collisions

The ultrarelativistic heavy-ion collisions are supposed to study the properties of strongly interacting matter which is exposed to extreme conditions of high energy density. According to the Quantum Chromodynamics (QCD), a phase transition from a state of hadronic constituents to a plasma of deconfined quarks and gluons (QGP) takes place within the strongly interacting matter. This can be achieved by colliding heavy ions at ultrarelativistic energies. Various experiments which were supposed to explore the conditions that are sufficient for deconfinement have been carried out at SPS/CERN and RHIC/BNL. Information on nature, composition and size of the medium of origin can be deduced from the hadron multiplicities and their correlations. Figure (1) shows the spacetime evolution of a longitudinally boost-invariantly expanding fireball. The QGP curve is also included. In the left part (a), we can see the result of a nucleus-nucleus collision without the QGP phase.

However, this indicates that the very existence of the QGP phase cannot be confirmed by simply analysing the final products, but the chemical equilibrium of the hadron constituents must be taken into account, too. A high level of chemical saturation generally indicates the deconfined phase created at the early stage of heavy ion collisions.

2 A brief introduction to the statistical model

In order to describe the equilibrium behavior of thermodynamical observables, we must use the statistical approach. If the approach of Gibbs is used, the thermodynamical observables can be expressed as an average over statistical ensembles. Thus, the equilibrium distribution may be obtained by an average over all accessible phase space. Assuming that the statistical operator can be used as Hamiltonian leading to the full hadronic mass spectrum, the only parameters describing the grand-canonical ensemble are temperature

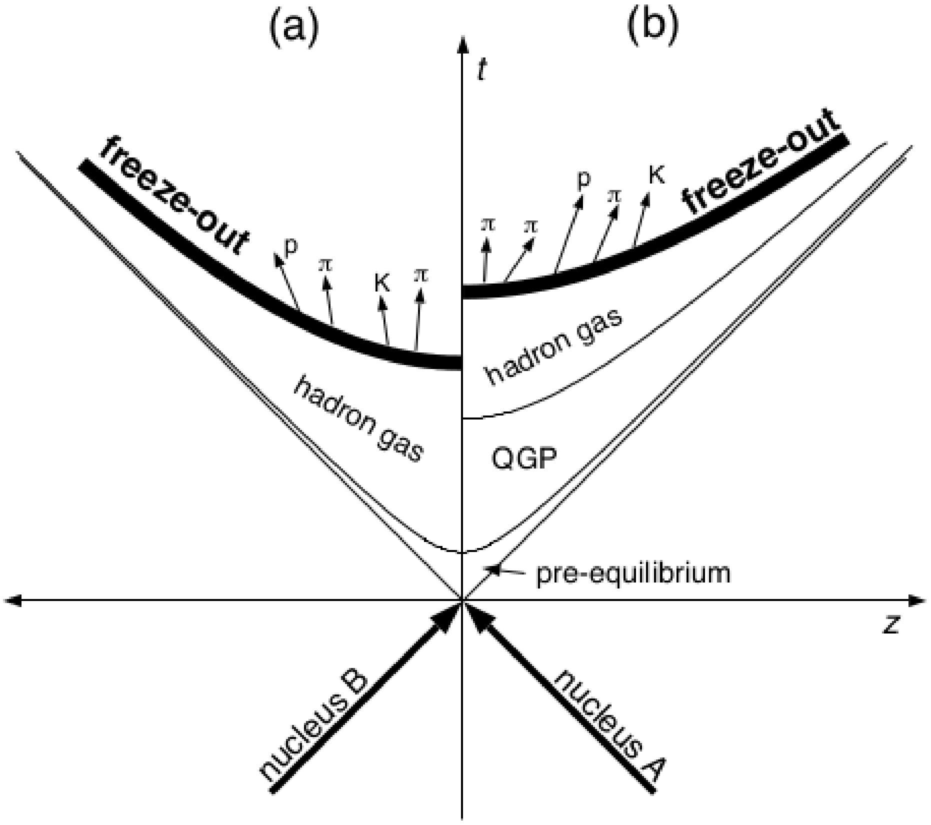

Figure 1: Spacetime evolution of a longitudinally boost-invariantly expanding fireball. Taken from [3].

T and baryon chemical potential μ_B. In case of chemical non-equilibrium, the strangeness suppression factor γ_S must be included as well.

2.1 Grandcanonical approach

The partition function necessary for computing the thermal composition of particle yields is given by Eq. (1). In order for the model to be considered trustworthy, the maximal temperature $T_{max} = 200$ MeV must be taken into account, as well as contributions from all mesons with masses below approximately 1,5 GeV and baryons with masses below approximately 2 GeV. The term for fugacity is given by Eq. (2). Eq. (3) shows the logarithm of the partition function for particle i of strangeness S_i, baryon number B_i, electric charge Q_i and spin-isospin degeneracy factor g_i. The term for ε_i is expressed by Eq. (4). The (+) and (-) signs represent fermions and bosons, respectively.
If lower energies are considered - in this case we assume that $T < 100$ MeV, so that the energy is considered low - the width of the resonances must be taken into account and the partition function has to be modified.

$$Z^{GC} = Tr[e^{-\beta(H-\sum_i \mu_{Qi} Q_i}] \tag{1}$$

$$\lambda_i = \exp\left(\frac{\mu_b B_i + \mu_S S_i + \mu_Q Q_i}{T}\right) \tag{2}$$

$$\ln Z_i = \frac{V g_i}{2\pi^2} \int_0^{+\infty} \pm p^2 dp \ln[1 \pm \lambda_i \exp\left(-\frac{\varepsilon_i}{T}\right)] \tag{3}$$

$$\varepsilon_i = \sqrt{p^2 + m_i^2} \tag{4}$$

where H is the Hamiltonian of the system, Q_i conserved charges, μ_i chemical potentials related to the respective baryon number, $\beta = 1/T$, T temperature, g_i spin-isospin degeneracy factor.

2.2 Canonical approach

Since the grand canonical approach is suitable for systems with a large number of produced hadrons only, the canonical ensemble is mandatory for small systems and for low energies. This leads to the so-called "canonical suppression", which is a phase space reduction for particle production. The density n_i^C of particle i with strangeness S can with a good approximation be related to the grand canonical value n_i^{GC}, as is shown in Equation (5).

$$\frac{n_i^{GC}}{F_S} = n_i^C \tag{5}$$

where

$$F_S = \frac{I_0(x)}{I_S(x)}$$

and $I_S(x)$ is the Bessel function of order S.

3 Comparison of model and experimental results

Comparison has been made between thermal model predictions and experimental particle ratios for Pb-Pb collisions at 40 GeV/nucleon (Figure (2)) and for Pb-Pb collisions at 158 GeV/nucleon (Figure (3)). The thermal model calculations were obtained with $T = 170$ MeV, $\mu_B = 255$ MeV, respectively. There are 11 particle ratios included for Pb-Pb collisions at 40 GeV/nucleon and 26 particle ratios for 158 GeV/nucleon. The obtained (T, μ_B) values are (148 ± 5, 400 ± 10) MeV and (170 ± 5,255 ± 10) MeV, respectively. The corresponding χ^2 values were obtained from Equation (6). In order for the fit of the model to data to be as good as possible, the term in Eq. (6) must be at its minimum.

$$\chi^2 = \frac{(R_i^{exp.} - R_i^{model})^2}{\sigma_i^2} \tag{6}$$

where $R_i^{exp.}$ and R_i^{model} are the obtained i-th particle ratio and the calculated value, respectively and σ_i represent the errors.

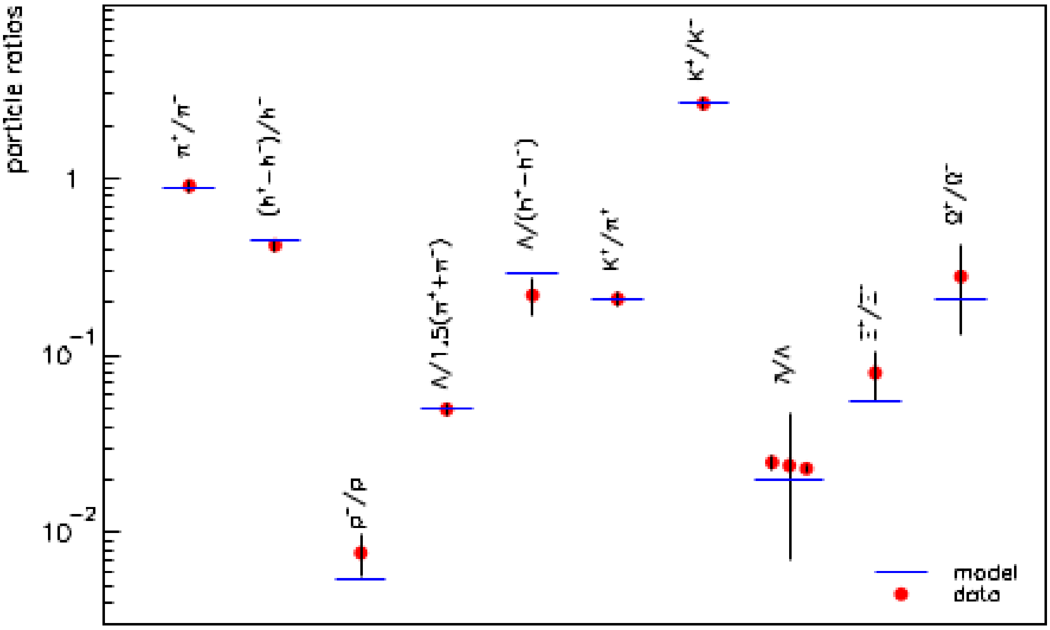

Figure 2: Comparison between thermal model predictions and experiental particle ratios for Pb-Pb collisions at 40 GeV/nucleon. Taken from [1].

4 Review of my bachelor thesis

In my bachelor thesis, I am going to further explore the influence of high-energy resonances on the temperature of the ensemble, the influence of the finite width of the resonances as well as the influence of the eigenvolume of hadrons. This will be done with the help of the SHARE3 simulation program.

References

[1] P. Braun-Munzinger, K. Redlich, J. Stachel – Particle production in heavy-ion collisions

[2] A. Andronic, P. Braun-Munzinger, J. Stachel – Hadron production in central nucleus-nucleus collisions at chemical freeze-out

[3] F. Sanino, I. Bearden, B. Tomášik, T. Dossing – Topics in modern nuclear physics

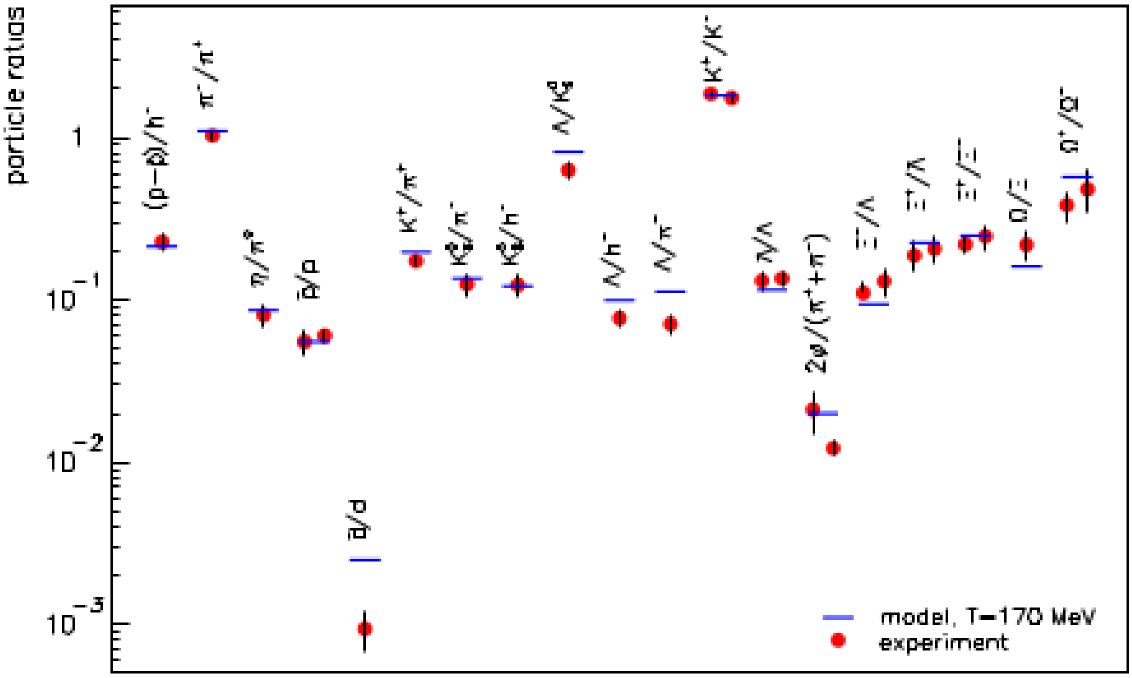

Figure 3: Comparison between thermal model predictions and experiental particle ratios for Pb-Pb collisions at 158 GeV/nucleon. Taken from [1].

Study of the properties of charm and bottom quarks using non-photonic electrons

Bc. Jan Vaněk*(vanekjan@fjfi.cvut.cz)*

It is believed that very shortly after the Big Bang (approx. 10^{-5} s [1]) a very hot and dense medium, called the quark-gluon plasma (QGP), was present in the Universe. In contrast to what we observe in contemporary Universe, the quarks and gluons inside QGP are not trapped in hadrons. Such state of matter was (officially) experimentally discovered relatively recently, in the year 2005, at Relativistic Heavy Ion Collider (RHIC) in Brookhaven National Laboratory (BNL) in ultra-relativistic heavy-ion (A+A) collisions. Since then the QGP is intensively studied using A+A collisions at RHIC and also at the Large Hadron Collider (LHC) in CERN laboratory near Geneva.

The QGP is created in he A+A collision nearly immediately after the impact of the two nuclei and lives just for very short time, which the reason why it is not possible to investigate it directly. Fortunately the collision itself provides excellent probes to the QGP, which are particles created during so-called hard scattering in early stage of the collision, before the QGP fireball is ignited. These particles then have to pass through the QGP, where they loose energy, which provides information about the medium.

There are many particle species originating in the hard scattering, two of which are open heavy flavour mesons, i.e. D mesons, containing one c quark and B mesons, containing one b quark. Interesting is then to compare their production in A+A and proton-proton collisions, which gives information about c and b quark production suppression. It would be also convenient to measure the mesons separately, which turned out not to be that simple.

One possibility is to measure the open heavy flavour mesons via semi-leptonic decay channel, in which one of the products is non-photonic electron (NPE) or positron and the others are (anti-)neutrino and a hadron. Since D mesons have shorter lifetime than B mesons, they can be distinguished by determining the distance between the primary (place, where they are created) and secondary vertex (place, where they decay). This distance can be quantified by variable called distance of closes approach (DCA) to the primary vertex, which is the shortest distance between the primary vertex and a reconstructed track of a chosen decay product, in this case electron, in plane transverse to the beam axis. DCA can be alternatively denoted d_0, which is usually called track impact parameter.

Telling apart heavy flavour mesons by measuring DCA is possible provided a detector with high spatial resolution is available. The shortest lifetime of all open heavy flavour mesons has D^0 ($c\overline{u}$) with $c\tau = 123\,\mu$m, therefore the DCA resolution has to be better than $\sim 100\,\mu$m in NPE analysis. These requirements matches ALICE detector at the LHC with its ITS (Inner Tracking System) subdetector, which has DCA resolution better than $\sim 80\,\mu$m for particles with $p_T > 1$ GeV/c [2] and STAR detector at RHIC with its HFT (Heavy Flavour Tracker) subdetector with DCA resolution better than $\sim 30\,\mu$m for $p_T > 1.5$ GeV/c [3].

Then restriction can be applied on DCA in real data in order to detect given particle. For example, when analyzing B mesons, the value of electron DCA is required to be greater than specific value, which is usually estimated from a simulation. This reduces contamination of the data sample by photonic electrons, NPE from D mesons and also hadrons coming predominantly from the primary vertex. Without the DCA cut, the hadron contamination is a big issue in identification of particles (PID) with p_T higher than ~ 6 GeV/c as PID is determined from energy loss in TPC (Time Projection Chamber). The energy loss of several particle species is very similar in this p_T region, which prevents clear PID.

Measurements of open heavy flavour mesons using DCA cuts were already performed at ALICE experiment in p+p and Pb+Pb collisions. All results obtained by DCA cuts are consistent with the results without it, as shown for example in [2] (p+p, $\sqrt{s} = 7\,$TeV). The same paper also shows that the hadron contamination is much lower after application of the DCA cut. At $p_T = 8$ GeV/c the contamination falls from $\approx 20\%$ to less than 3%, which can be considered as a significant improvement. There are no official NPE results from STAR experiment yet, as the HFT was installed into STAR detector in 2014 and it is not fully ready to be used.

So generally it can be said that the new method of data analysis using DCA cut, works well, as proven by ALICE experiment. The method can be therefore used to obtain spectrum of NPE originating from semi-leptonic decay of open heavy flavour mesons. Measurement of NPE, i.e. D and B mesons, is yet to be done at STAR experiment, as soon as operation the HFT is fully understood.

References

[1] K. Yagi et al., Quark-gluon Plasma, Cambridge University Press 2005

[2] ALICE collaboration, CERN-PH-EP-2012-229, 2013

[3] O. Kunsu, Measurements of Charm and Bottom Productions in Semi-Leptonic Channels at STAR, poster, Quark Matter 2015

Underlying event at 13 TeV

Matous Vozak*(vozakmat@fjfi.cvut.cz)*

1 Underlying event

To understand the meaning of the term underlying event in pp collisions a brief introduction to collision interpretation is needed. At the Large Hadron Collider (LHC) bunches of protons are accelerated in two opposite beams which collide together at places along the beam pipe surrounded by huge detectors. Interesting thing when colliding protons is their rather busy collision environment. As discovered in previous century protons have composite structure. They are not elementary particles like electrons thus consist of other particles - quarks and gluons, generally termed as partons as they carry a part of proton momentum. With this in mind, a collision between protons can be viewed as the collision of their constituents (partons).

If interacting parton carries a lot of proton momentum fraction, very energetic particles (hard process) can be created with high transverse momentum due conservation of momentum as protons from both beams have the same energy. From these energetic particles objects of studies as jets, Z, W bosons are created. Except this energetic interaction between pair of partons there are also interactions between other pairs as protons have more than one parton, leading to additional activity through so called multi-parton interaction.

Particles coming out of collision can have either color or electric charge and as such are able to radiate particles (the probability of radiation decreases with rising angle between radiated and radiating particle) which can further radiate other particles (if they posses either charge) resulting to effect termed as parton showers. Therefore, instead of having only one particle coming from collision, there is a collimated cone of objects. However, these objects are not detectable because of the strong interaction which affects them and quickly bonds them together into color neutral objects. This process is called hadronization and takes place before particles reach detectors. Furthermore particles with a short mean life time can also decay on the path hence only their ”daughter” particles are detected.

These additional contributions as multi-parton interaction, parton showers and beam and beam remnants represent contamination to measurement and are generally termed as underlying event (Figure 1). There are measurements such as low p_T jets measurements where this contribution is significant. Therefore, it is important for precise measurements to study and determine the underlying event activity in pp collisions.

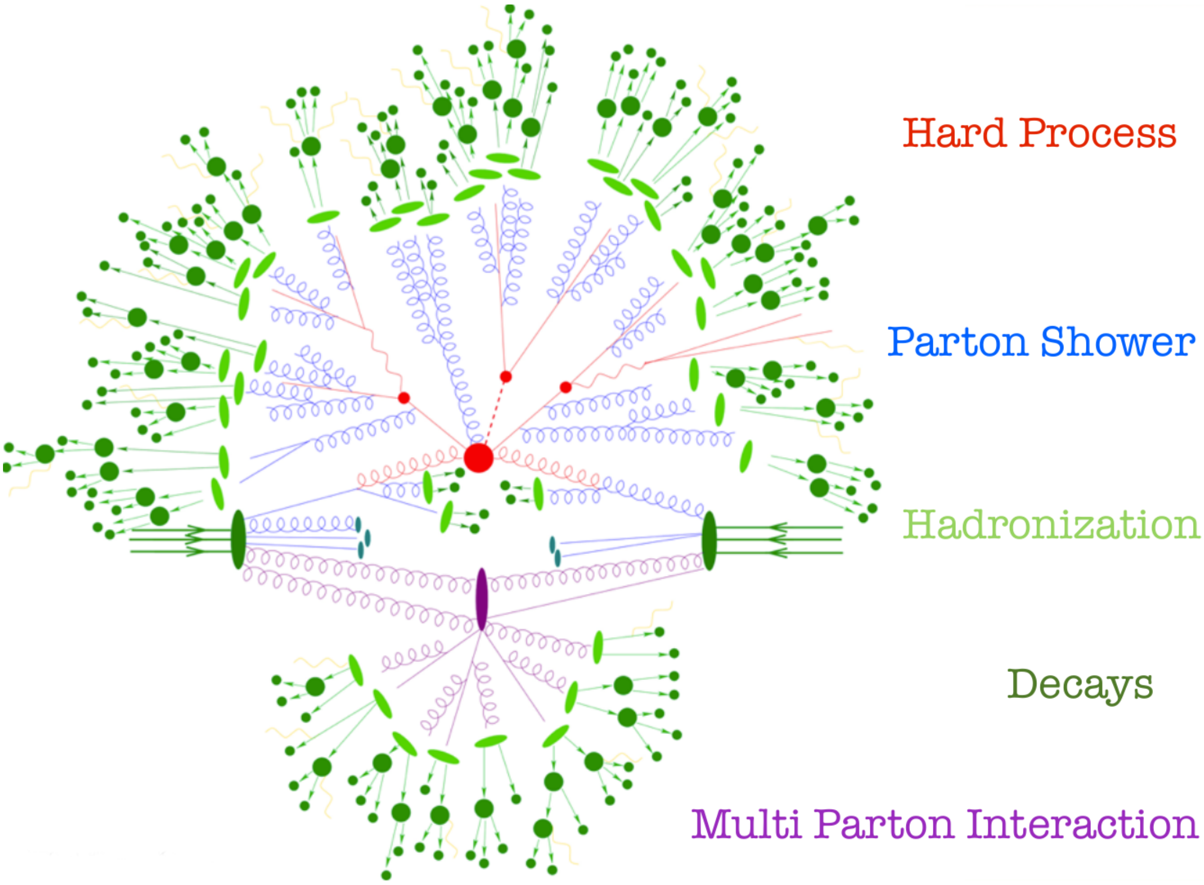

Figure 1: Representation of pp collision in MC simulation [1].

2 ATLAS underlying event analysis at 13 TeV

One approach how to measure the contribution of underlying event is to introduce regions in the plane perpendicular to the beam pipe Figure 2. First, particle with the highest transverse momentum is found in an event(leading track, the path of particle which passed through detector is referred as track). Then for each event three regions - toward, transverse and away are defined by projecting its leading track momentum to the perpendicular plane and measuring the difference between an azimuthal angle $\Delta\phi$ of the leading track and other tracks.

- Toward region $|\Delta\phi| < \pi/3$
- Transverse region $\pi/3 < |\Delta\phi| < 2\pi/3$
- Away region $2\pi/3 < |\Delta\phi|$

The purpose of this plane division lies in conservation of energy and momentum because most of the energy from the hard collision is focused in the toward and away regions. Therefore, the transverse region is very sensitive to this additional underlying event activity and thus good direction to be looking at.

The particles of interest in this particular analysis are primary charged particles where primary means with a mean proper lifetime $\tau_{prim} \gtrsim 0.3 \cdot 10^{-10}$ s. This can be either

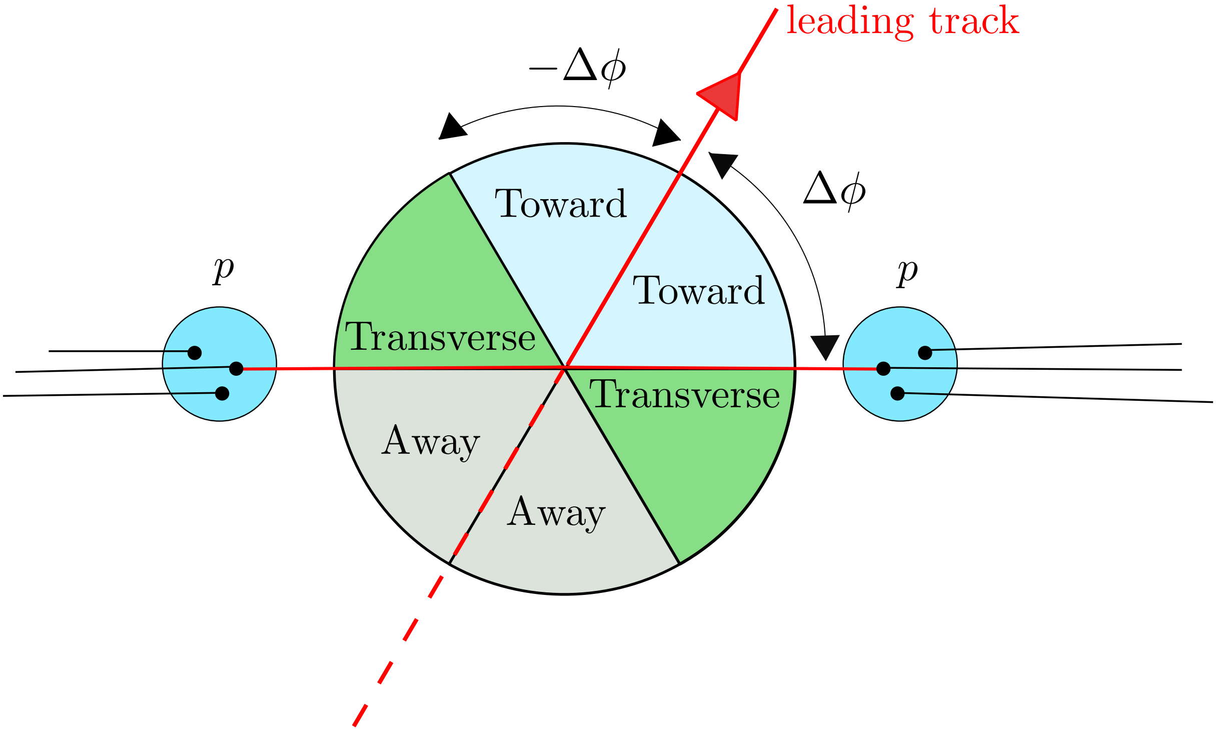

Figure 2: Separation of plane perpendicular to the beam pipe into 3 main regions according to the difference of azimuthal angle $\Delta\phi$ between the leading track and other tracks

particles coming directly from the collision or particles which decayed from particles with $\tau < \tau_{prim}$. Condition on particles are following: p_T of each particle has to be greater than 500 MeV and for leading track greater than 1 GeV which is a condition that separate the underlying event study from minimum bias. Pseudorapidity of particles has to be $|\eta|$ lesser than 2.5 because of ATLAS detector acceptance. Additional conditions are on impact parameters of particles and their hits in layers of ATLAS inner detector.

Observables which were studied in order to represent the underlying event activity are presented in Table 1.

	$\langle d^2N_{ch}/d\eta d\phi\rangle$	$\langle d^2\Sigma p_T/d\eta d\phi\rangle$	$\langle p_T\rangle$
Detector level	Mean number of selected tracks per unit $\eta\phi$	Mean scalar p_T sum of selected tracks per unit $\eta\phi$	average p_T of selected tracks

Table 1: Measured observables on detector level.

3 Results

In Figure 3 $\langle d^2N_{ch}/d\eta d\phi\rangle$ with respect to the transverse momentum of leading track p_T^{lead} in transverse region is plotted. As in previous measurements of underlying event [2], [3], there is a visible plateau (so called underlying event pedestal) starting around at 5 GeV. Therefore, the charged particle density is approximately constant with rising p_T^{lead} and no more particles are created from underlying event activity. Another valuable information, visible in bottom ratio pad, is that MC are tuned reasonably well, in particular Monash and HERWIG which are UE tunes.

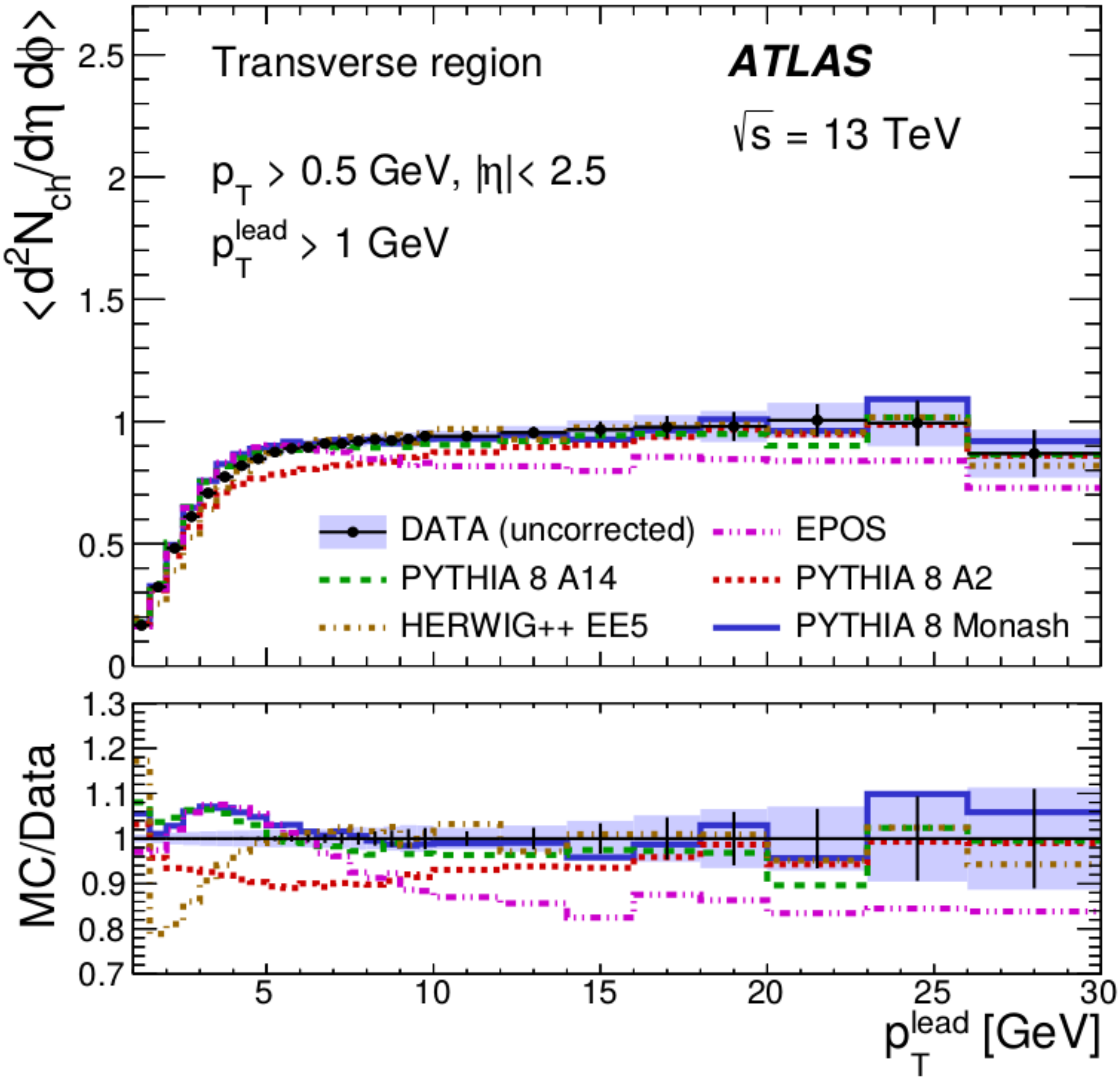

Figure 3: Comparison of detector level data and MC predictions for the $\langle d^2N_{ch}/d\eta d\phi\rangle$ wrt to p_T^{lead}. The bottom panel shows the ratio of MC predictions to data. The shaded bands represent the combined statistical and systematic uncertainties, while the error bars show the statistical uncertainties [4].

In Figure 4 there is $\langle d^2\Sigma p_T/d\eta d\phi\rangle$ with respect to a difference of azimuthal angle between leading track and other tracks $|\Delta\phi|$ for $p_T^{lead} > 1$ GeV and for $p_T^{lead} > 5$ GeV. Toward region has the dominant contribution which is even more visible at $p_T^{lead} > 5$ GeV as this is even harder process. In transverse region Σp_T drops down and slowly rise again towards the away region. The rest of plots in all regions can be found at [4].

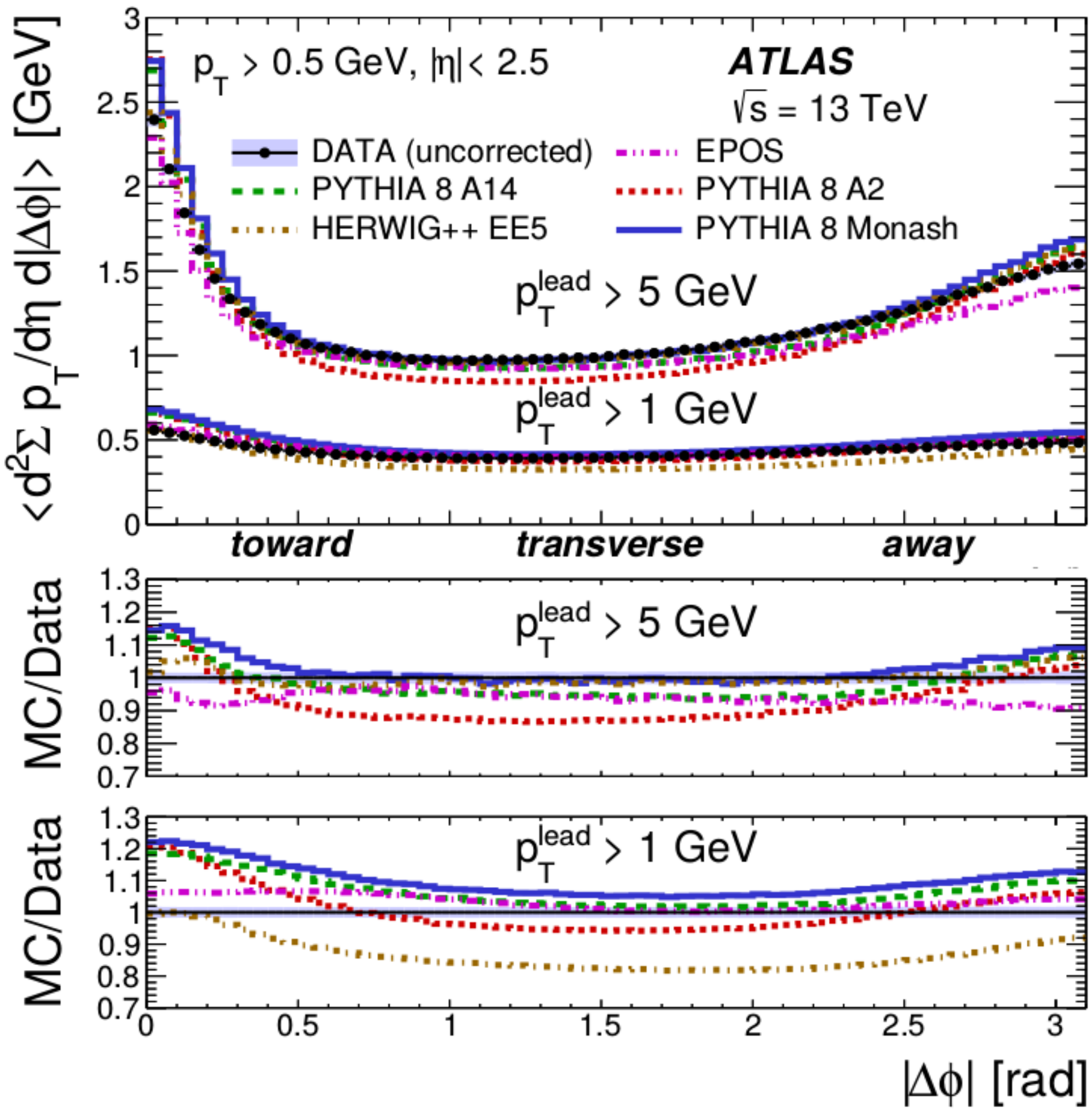

Figure 4: Comparison of detector level data and MC predictions for $\langle d^2N_{ch}/d\eta d\phi\rangle$ wrt $|\Delta\phi|$. The leading track is defined to be at $|\Delta\phi| = 0$, and excluded from the distributions. The distributions obtained by restricting p_T^{lead} to different values are shown separately. The bottom panel shows the ratio of MC predictions to data. The shaded bands represent the combined statistical and systematic uncertainties, while the error bars show the statistical uncertainties [4].

References

[1] Hoche, Stefan, Introduction to parton-shower event generators, arXiv:1411.4085 (2014)

[2] The ATLAS collaboration, Measurement of underlying event characteristics using charged particles in pp collisions at $\sqrt{s}$ = 900 GeV and 7 TeV with the ATLAS detector, Phys. Rev. D83 (2011)

[3] The CDF collaboration Studying the underlying event in Drell-Yan and high transverse momentum jet production at the Tevatron, arxiv.org/pdf/hep-ex/0404004 (2010)

[4] Vozak Matous, Measurement of distributions sensitive to underlying event at the LHC at 13 TeV, https://cds.cern.ch/record/2114789 (2015)

Jets and jet algorithms at the LHC

Ota Zaplatílek *(zaplaota@fjfi.cvut.cz)*

One of the interesting and very often studied processes at high-energy proton-proton collisions is the so called hard-scale process where the exchanged momentum is significantly higher than a few GeV. In these cases most of the observed energy is released in a collinear flow of particles called jets.

There are two main ways to find these jets, the so called jet algorithms, namely cone and clustering jet algorithms. Basic ideas of mentioned algorithms are the following. Cone algorithms surround significant flows of particles by cones with radius R. Whereas clustering algorithms combine two objects i, j retrospectively. They use this procedure repeatedly, which is based on comparing the mutual distances d_{ij}, d_{iB} of a chosen particle j and considered protojet i to find the leading particle, which stays at the beginning of QCD branching. The most common use of clustering algorithms in hadron-hadron collisions is described by formula (1) using kinematic variables: transverse momentum p_t, rapidity y, azimuthal angle ϕ and a set of input parameters: jet radius R and a parameter p, which is explained below.

$$d_{min} = min(d_{ij}, d_{iB}) \quad \text{where} \quad d_{iB} = p_{t_i}^{2p} \quad \text{and} \quad d_{ij} = min(p_{t_i}^{2p}, p_{t_j}^{2p}) \cdot \frac{\Delta R_{ij}}{R} \tag{1}$$

$$\Delta R_{ij} = \sqrt{(y_i - y_j)^2 + (\phi_i - \phi_j)^2}$$

The parameter p determines the weight of transverse momenta p_t. It also distinguishes the method for assigning particles to a jet. Accordingly it is possible to differentiate the k_t ($p = 1$), anti-k_t ($p = -1$) and Cambridge/Aachen ($p = 0$) algorithms. In the case of anti-k_t is $p = -1$, what leads to several important properties. Firstly since $p = -1$ hard particles are clustered first. Parameter $p = -1$ also relates with symmetrical output in space of $(\phi \times y)$ and insensitivity to soft particles. The clustering jet algorithms also comply with the important conditions for collinear and infrared safety in general. Consequently the anti-k_t algorithm represents the most widely used and the safest algorithm of all currently used algorithms[1].

The presentation was focused on two main topics. Firstly, it dealt with comparisons of prediction of MC generator Pythia 8.180 with data measured by the collaboration ATLAS at $\sqrt{s} = 7$ TeV for observables: the sum of transverse energy and the flow of transverse energy at ATLAS detector and differencial cross section for inclusive jet production as a function of rapidity and transverse momenta.

And secondly the difference among clustering jet algorithms were discussed. In more detail we presented the results of a study of kinematic observables of jets reconstructed by clustering algorithms using the hard QCD process simulated by MC generator Pythia

8.180 at scale of $p_t > 10$ GeV and $\sqrt{s} = 7$ TeV on particle level. The observed dependencies of spectra were interpreted, namely jet multiplicity, rapidity, pseudorapidity, transverse momentum, invariant mass and energy of jet reconstructed by the anti-k_t algorithm with different radii $R \in \{0.2, 0.4, 0.6, 0.8, 1.0, 1.5\}$, as well as reconstructed by different sequence clustering jet algorithms with reference radius $R = 0.6$. [2]

The most important results are shown in Fig. 1 and Fig. 2. They show unnormalised spectra of average transverse momentum of jets in events with exactly two jets $\bar{p}_t^{diJet}$. Fig. 1 describes distribution of $\bar{p}_t^{diJet}$ of jets reconstructed by anti-k_t with different R, whereas Fig. 2 shows jets obtained by different clustering algorithms. These dependencies describe a decreasing number of found jets with increasing p_t. Furthermore we observed that differences of ratios $R_x/R_{0.6}$ in p_t spectra in Fig. 1 of jets reconstructed by the anti-k_t algorithm with different radii decrease with rising p_t with respect to the reference radius $R_{0.6} = 0.6$. It applies for both radii higher and lower than $R = 0.6$.

The shape of ratio $R_x/R_{0.6}$ could be explained for high and low R individually using two assumptions. First, jets are more collimated and contain more final state radiation with increasing p_t, what was confirmed in studies of integral jet shape [3]. Second, relative increment of p_t leakage from underlying event is decreasing with rising p_t [4].

Narrow jets with $R < 0.6$ are not wide enough to collect all final state radiation at low scale ≈ 30 GeV. Therefore jets collect more final state radiation with increasing p_t so they behave similarly as jets with $R = 0.6$. Whereas wide jets with $R > 0.6$ are voluminous enough. They collect much of the underlying event, nevertheless they contain all final state radiation. With increasing p_t, fraction of underlying event in jets decreases, hence wide jets behave similarly as jets with $R = 0.6$ and fraction $R_x/R_{0.6}$ approaches unity.

An analogous character could be seen in ratio of spectra for the same variable $\bar{p}_t^{diJet}$ in Fig. 2, but in this case jets were reconstructed by the anti-k_t, k_t and Cambridge/Aachen algorithms with $R = 0.6$.

The ratios of Cambridge/Aachen and k_t with respect to the anti-k_t also tend to unity. Clustering algorithms differ by the choice of the p parameter, in other words by the difference in the methods for assigning particles to jet. The anti-k_t algorithm clustures hard particles first, the k_t algorithm starts with soft ones, whereas the Cambridge/Aachen works only with mutual distances. In fact jets at high p_t are formed in the area of hard particles, so it does not depend whether clustering starts with soft or hard particles. As it was written previously jet are more collimated with raising p_t, hence the ratio tends to unity.

Consequently the results of comparison of prediction of MC generator Pythia 8.180 with default setting with respect to the ATLAS data at 7 TeV show the differences smaller than 25%. Secondly it was proved that the differences of the anti-k_t algorithm with different radii decrease with increasing scale p_t. The same tendency was shown for different clustering algorithms, too. Note, the significant differences are obvious for extreme large radii.

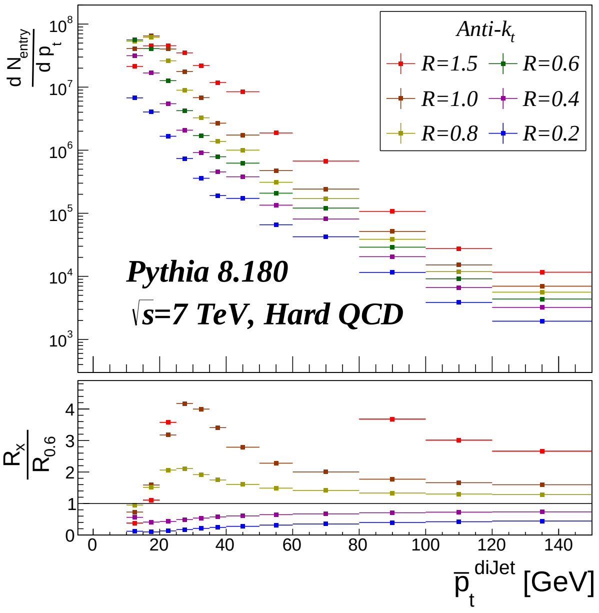

Figure 1: Comparison of shapes of unnormalised spectra of jets reconstructed by the anti-k_t algorithm with different radii R in Hard QCD process simulated by MC generator Pythia 8.180 at particle level for variable: average transverse momentum of jets in event with exactly two jets. The data are shown with statistical uncertainties. The ratio of p_t^{diJet} distribution $R_x/R_{0.6}$ with respect to $R_{0.6} = 0.6$ are shown in the lower panel.

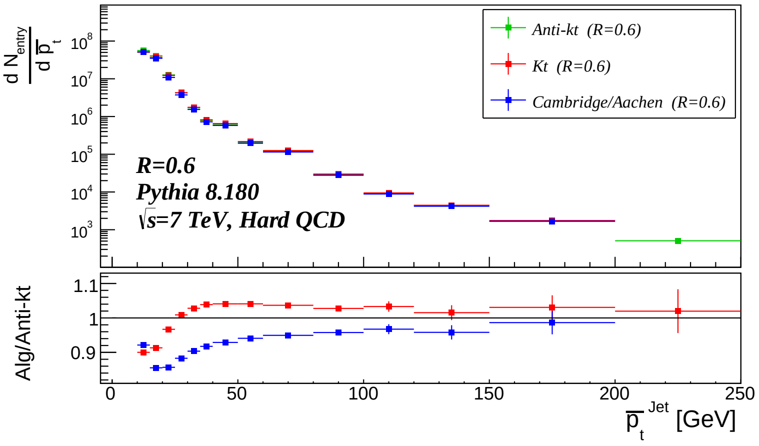

Figure 2: Comparison of shapes of unnormalised spectra of jets reconstructed by clustering algorithms, namely the k_t, anti-k_t and Cambridge/Aachen with radius $R = 0.6$ in Hard QCD process simulated by MC generator Pythia 8.180 at particle level for variable: average transverse momentum of jets in event with exactly two jets. The data are shown with statistical uncertainties. The ratio $Alg/Anti\text{-}k_t$ of p_t^{diJet} reconstructed by Cambridge/Aachen and k_t with respect to the anti-k_t are shown in the lower panel.

References

[1] M. Cacciari, G. P. Salam, *The anti-k t jet clustering algorithm*, 2008. arXiv:0802.1189 [hep-ph]

[2] O. Zaplatílek, Bachelor thesis: *Jets at the LHC*, 2016.

[3] The ATLAS Collaboration, *Study of Jet Shapes in Inclusive Jet Production in pp Collisions at* $\sqrt{s} = 7$ *TeV using the ATLAS Detector*, 2010. arXiv:1101.0070v1[hep-ex]

[4] G. P. Salam, *Phd-level lectures*, 2010-2011. `http://gsalam.web.cern.ch/gsalam/teaching/PhD-courses.html`

Rydberg Atoms and their Use in Experiment AEgIS

Alena Zemanová*(zemanal5@fjfi.cvut.cz)*

1 Experiment

AEgIS is an experiment, which is situated in CERN. It belongs to the group of experiments, that are trying to solve problems of antimatter. The abbrevation AEgIS stands for Antihydrogen Experiment: Gravity, Interferometry, and Spectroscopy. As we can see the primary goal of this experiment is direct measurement of the Earth´s local gravitational acceleration g on a neutral antihydrogen. The secondary goal is to carry out spectroscopic measurements on these antihydrogen atoms in flight.

Experiment AEgIS is not yet functional. However, it should work in eight simple steps. At first, positrons are produced by a ^{22}Na source and an accumulator. These are then captured and accumulated by the antiproton deceleration in a Penning trap and then cooled down to sub-K temperatures (to be precise, temperatures about 100mK are expected). Next step is the production of positronium (Ps) and its excitation to a high Rydberg state. After that, antihydrogen is finally pulsed-formed by resonant charge exchange between Rydberg Ps and cold antiprotons. Then we have to form antihydrogen beam by Stark acceleration and finally measure the g in a two-grating moiré deflectometer coupled with a position-sensitive detector. These steps can be seen in figure 1.

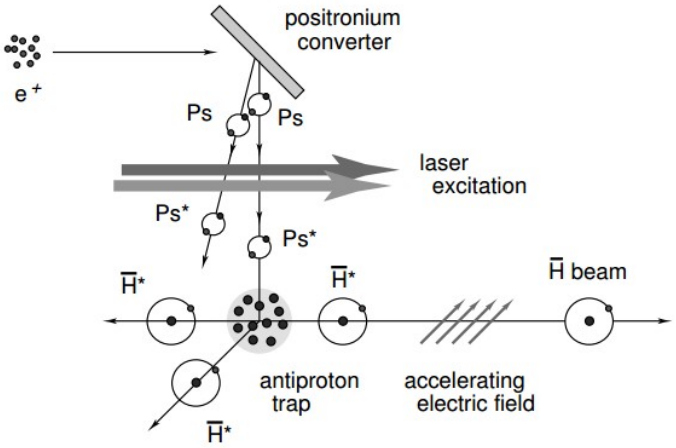

Figure 1: Setting of AEgIS experiment.

2 Rydberg Atoms

From this short description we can see, that in our experiment the primary role play the so-called Rydberg atoms. These are atoms, in which at least one electron is excited to a high quantum state. Ground states of atoms have principal quantum number n from 1 to 7, whereas Rydberg states has n as big as e.g. 300 (in AEgIS atoms with n around 25-30 will be used).

Production of Rydberg atoms is not very complicated process, they are mostly produced by three methods. The first one consist of charge exchange between a beam of ions and a population of neutral atoms of another species, resulting in the formation of a beam of highly excited atoms. Second one uses the kinetic energy of an electron to increase the internal energy of atoms exciting it to a broad range of different states. Finally, the third one, called optical excitation, consist of absorbing the incident photon by the target atom, absolutely specifying the final state energy. This excitation is used in our experiment, so I will explain it more thoroughly.

Excitation of positronium in experiment AEgIS takes place in two steps. At first, the positronium is excited to state 3. This step is much more complicated than the second step, which is excitation to higher states (15-17). Positronium is excited by a group of lasers, which wavelengths were tuned in the range 204-206 nm for first step, and 1680-1715 nm for second step. Getting these values of wavelengths is shown in the figure 2.

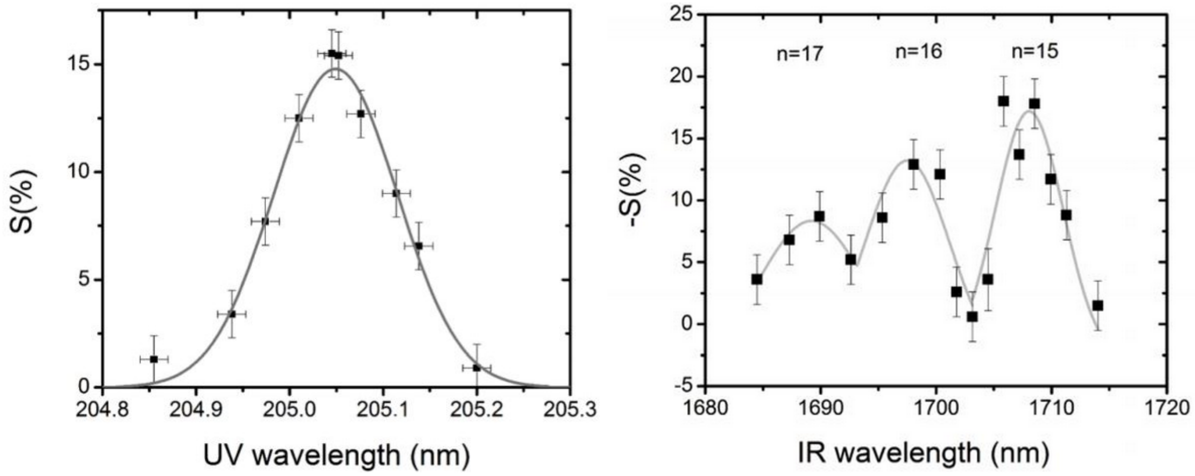

Figure 2: Tuning of the UV and IR laser wavelength during optical excitation.

3 Rydberg Atoms in External Fields

Due to the setting of the experiment, we have to investigate, how Rydberg atoms behave in external fields. Because of large distance between the electron and the ion-core an extremely large electric dipole moment (d) is possible. Energy associated with the presence of an electric dipole in an electric field (F) leads to Stark shift $E_s = -d \cdot F$. Due to this shift states may have energy that increases or decreases with field strength (depending on the sign of the projection of the dipole moment). Theoretical field strength at which a crossing would occur, assuming no coupling between the states, is called Inglis-Teller limit and could be computed from equation (1). Consequently, the energy levels from adjacent n-manifolds cross at the Inglis-Teller limit.

$$F_{IT} = \frac{e}{12\pi\varepsilon_0 a_0^2 n^5} \tag{1}$$

The potential energy found in the electronic Hamiltonian for hydrogen is the 1/r Coulomb potential, which means there is no quantum defect (could be seen in the figure 3). However, for lithium the presence of an ion-core, that can be polarized and penetrated by the Rydberg electron, adds additional terms to the electronic Hamiltonian (resulting in a finite quantum defect, which is called avoided crossing). Avoided crossing can be described as the case when the eigenvalues of a Hermitian matrix representing an observable for a system and depending on N continuous real parameters cannot cross (=two or more eigenvalues cannot become equal in value) and could be seen in the figure 3.

If so-called magic numbers of Rydberg atoms formed a planar cluster, it is called Rydberg matter. This matter is metastable with long radiative lifetimes and interacts only weekly with light. The long lifetime is consequence of the lack of overlap between excited and ground states, the forbidding of transitions between them and finally exchange-correlation effects hindering emission through necessitating tunnelling that causes a long delay in excitation decay.

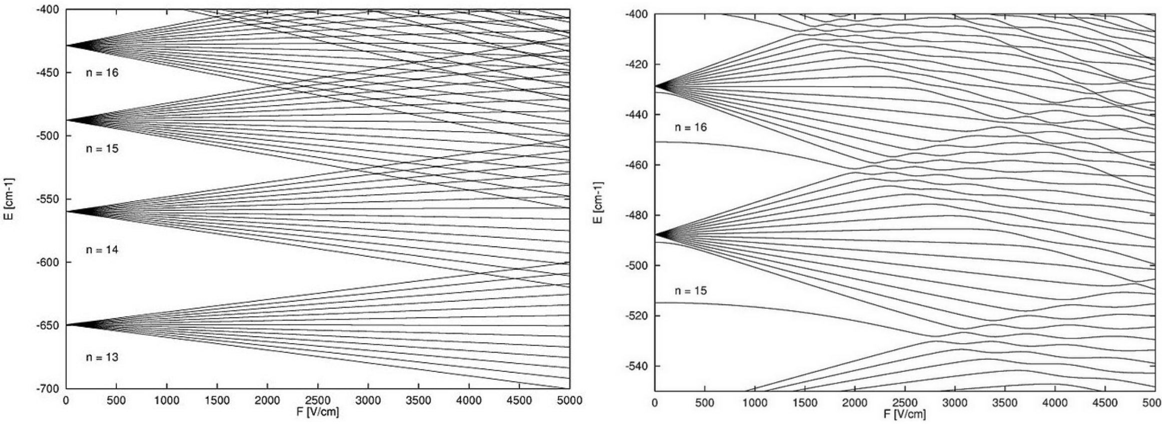

Figure 3: Computed energy level spectra of hydrogen and lithium in an electric field near n=15.

References

[1] A. Tauschinsky, Rydberg Atoms in External Electric Fields - Master Thesis ,(2008)

[2] The AEgIS/AD-6 collaboration, Progress report on the AEgIS experiment, (2015)

[3] Rydberg atom, Wikipedia, The Free Encyclopedia, Retrieved February 21, 2016, from *https : //en.wikipedia.org/w/index.php?title = Rydbergatom&oldid* = 699111423

[4] Rydberg matter, Wikipedia, The Free Encyclopedia, Retrieved February 21, 2016, from *https : //en.wikipedia.org/w/index.php?title = Rydbergmatter&oldid* = 683802247